DECAY OF HEAVY AND SUPERHEAVY NUCLEI FORMED IN A VARIETY OF NUCLEAR REACTIONS

A THESIS

Submitted to the

FACULTY OF SCIENCE

THAPAR INSTITUTE OF ENGINEERING

AND TECHNOLOGY (TIET), PATIALA

FOR THE DEGREE

OF

DOCTOR OF PHILOSOPHY

by

Amandeep Kaur

SCHOOL OF PHYSICS AND MATERIALS SCIENCE

TIET, PATIALA-147004

INDIA

JANUARY, 2019

I, very humbly, dedicate this work to

My Mother

A strong and gentle soul who taught me to trust in GOD

My Father

For earning an honest living for us

&

My Supervisor

For encouraging me to believe in myself

CERTIFICATE

This is to certify that the work embodied in this thesis entitled as "**DECAY OF HEAVY AND SUPERHEAVY NUCLEI FORMED IN A VARIETY OF NUCLEAR REACTIONS**" has been carried out by **Ms. Amandeep Kaur** under my supervision. This work fulfills the requirements for the award of degree of Doctor of Philosophy in the School of Physics and Materials Science, Thapar Institute of Engineering and Technology, Patiala. The content of this thesis is candidate's own work and has not been submitted partially or wholly for the award of any degree in any university or institute.

Supervisor

Dr. Manoj K. Sharma

Professor

School of Physics and Materials Science

Thapar Institute of Engineering and Technology (TIET)

Patiala- 147004

Punjab (India)

Acknowledgments

"No one who achieves success does so without the help of others. The wise and confident acknowledge this help with gratitude" ~ Alfred North Whitehead

My joy knows no boundaries as I take this opportunity to express my deepest and sincere gratitude to my supervisor **Dr. Manoj K. Sharma**, School of Physics and Materials Science (SPMS), Thapar Institute of Engineering and Technology (TIET), who has provided me unwavering support and mentorship through out this endeavor. He has always poured me with the exquisite knowledge he holds with him in the field of Nuclear Physics and has always motivated me with his constructive remarks. I would like to thank the members of my Doctoral committee Dr. S. Jana, Dr. Raj Kumar and Dr. S. S. Bhatia for examining the progress reports and encouraging me to make my work better. I express my sincere thanks to Prof. O. P. Pandey, Head, School of Physics and Materials Science (SPMS), Thapar Institute of Engineering and Technology (TIET) for being an example to be followed in pursuing research works. I am also grateful to Dr. Rafat Siddique, Senior Professor and Dean Research and Sponsored Projects (RSP). Sincere thanks to Mrs. Sonam for always being so polite and affectionate.

My sincere gratitude to **Dr. Gudveen Sawhney** for being the best person of my lab and with whom I share precious personal and professional moments which will be cherished throughout life. I would like to offer my gratitude to **Dr. Gurvinder Kaur** and **Dr. Kirandeep Sandhu**, under whose guidance I started this work and I tried to follow their footsteps to steer towards the completion of this work.

I am extremely thankful to Ishita Sharma for always being there with a big smile on her face and I am thankful for the advices she gave me along my journey of this achievement. Neha Grover deserves a special thanks as I am privileged to be her colleague and I am honored to complete this journey with her. I would also like to extend my thanks to Rajni Mittal, Kanishka Sharma, Gurjeet Kaur, Amandeep Kaur and Shivani Jain for the collegial environment they created in the lab and for the helping hands they offered whenever needed.

I am filled with immense joy as I thank my sister-like friend *Kuljeet Kaur*, who has always proved to be a shoulder to lean on whenever stressful situations invaded during the course of this work and her companionship will be acknowledged till the last breath. The support, encouragement and comfort that came from the gems of my life Manjot Kaur, Navjot Dhindsa, Purnima Sharma, Harleen Kaur, Sumeet Sagar, Mankaran Singh, Ishtpal Singh, Jagbir Singh Randhawa, Puneet and Harjeet Singh are gratefully acknowledged.

The smiling face of my niece Hardika and the unconditional love she offered and offers to me has always been a stress buster for me throughout this work. The amusing and satisfying company of Pankaj Batish and Raina Ahuja have always charged up my energy levels and their presence in my life is a blessing. I would also take no time in expressing my deepest appreciation to, *Gurpreet Saggu* for being patient with me and believing in my competency. The faith he put in me conveyed a spirit of self-believe which helped in shattering my delusion of being incapable of accomplishing this task. There have been a lot of people who walked alongside this journey, helped me and guided me, knowingly and unknowingly. I offer heartfelt thanks to all of them. Some are along with me and some of them changed their paths, they still deserve a cordial gratitude.

I may be short of words to pay the debt of recognition towards the lady who have always been a source of strength for me, my mother, Mrs. Inderjit Kaur. I, in whole of my lifetime, will not be able to compensate her love which nourished me and accompanied me through every step of my life. Thanks to my brother Mr. Gauravdeep Singh for just being my brother. A distinctive thanks to my father S. Dilbagh Singh, for always leading from behind and it was because of him only that I was courageous enough to dream big and to pursue those dreams. My other family members, my sisters, Minnie, Dr. Ishatdeep Kaur, Rupinder Kaur and Navjot Kaur and my brother, Dr. Ram are also entitled to be a source of encouragement for me and deserve a vote of thanks. In the last, I would love to pay my profound obligation to all those people who have been a part of this momentous achievement.

I gratefully acknowledge the Department of Science and Technology (DST), Govt. of India, to offer financial support in the form of INSPIRE Fellowship that made my Ph.D work possible.

Patiala

Date 11-10-19

Amandeep Kaur

(Amandeep Kaur)

List of Publications

I. International Journals:

1. Fragmentation analysis of α-induced reactions using clusterization approach.

   Amandeep Kaur and Manoj K. Sharma

   Nucl. Phys. A **969** 30-44 (2018).

   doi.org/10.1016/j.nuclphysa.2017.09.012 [Impact factor=1.992].

2. Competing analysis of α and 2p2n-emission from compound nuclei formed in neutron induced reactions.

   Amandeep Kaur and Manoj K. Sharma

   Nucl. Phys. A **957** 274-288 (2017).

   doi.org/10.1016/j.nuclphysa.2016.09.009 [Impact factor=1.992].

3. Formation and decay analysis of $^{98,104}Cd^*$ isotopes with in ^{40}Ca-induced reactions.

   Manjeet Gautam, **Amandeep Kaur** and Manoj K. Sharma

   Phys. Rev. C **92**, 054605 (2015).

   doi.org/10.1103/PhysRevC.92.054605 [Impact factor=3.304]

4. Fission decay analysis of n-induced reaction using collective clusterization approach.

   Amandeep Kaur, Gurvinder Kaur and Manoj K. Sharma

   Nucl. Phys. A **941** 152-166 (2015).

   doi.org/10.1016/j.nuclphysa.2015.06.014 [Impact factor=1.992].

5. Decay of the compound nucleus $^{297}118^*$ formed in the reaction $^{249}Cf + ^{48}Ca$ using the dynamical cluster-decay model.

   Gudveen Sawhney, **Amandeep Kaur**, Manoj K. Sharma and R. K. Gupta

Phys. Rev. C **92**, 064303 (2015).

doi.org/10.1103/PhysRevC.92.064303 [Impact factor=3.304]

6. Decay and related stability aspects of ^{266}Rf* nucleus formed in ^{18}O+^{248}Cm reaction.
   Kirandeep Sandhu, Manoj K. Sharma, **Amandeep Kaur** and Raj K. Gupta
   Phys. Rev. C **90**, 034610 (2014).
   doi.org/10.1103/PhysRevC.90.034610 [Impact factor=3.304]

7. 2n-emission from ^{205}Pb* nucleus using clusterization approach at E_{beam}~14-20 MeV.
   Amandeep Kaur, Kiran Sandhu and Manoj K. Sharma
   AIP Conf. Proc. **1728**, 020424 (2016).
   doi: 10.1063/1.4946475

8. Relative role of different radii in the dynamics of ^{8}B+^{58}Ni reaction.
   Amandeep Kaur, Kirandeep Sandhu, and Manoj K. Sharma
   AIP Conf. Proc. **1953**, 140080 (2018).
   doi: 10.1063/1.5033255

II. In International/National Conferences, Symposiums and Workshops:

1. Fragment mass distribution of radioactive ^{238}U* nucleus, Gurvinder Kaur, **Amandeep Kaur** and Manoj K. Sharma, 3rd National Confrence on Advanced Materials and Radiation Physics (AMRP), RP(P)-15, p-85 (2013).

2. Dynamics of transuranic ^{240}Np* nucleus formed in n-induced reaction, **Amandeep Kaur**, Gurvinder Kaur and Manoj K. Sharma, DAE symposium on Nuclear Physics, Vol. **59**, 364-365, BHU, Varanasi, India (2014).

3. Role of nuclear potential and associated deformations in the decay of Z=118 nucleus, G. Sawhney, **Amandeep Kaur**, Manoj K. Sharma, R. K. Gupta, 75-years of Nucl. Fission, BARC, Mumbai, DAE (2014).

4. Synthesis of ^{294}118 nucleus in ^{249,250}Cf(^{48}Ca, xn) reactions using the dynamical cluster-decay model, G. Sawhney, R. K. Gupta, **Amandeep Kaur**, and M. K. Sharma, Zakopane Conference on Nuclear Physics Extremes of the Nuclear Landscape, Zakopane, August 31-September 7, Book of Abstract p.197 (2014).

5. Decay study of ^{240}Np* nucleus using Dynamical Cluster-decay Model, G. Kaur, **Amandeep Kaur**, Manoj K. Sharma, National Conference on Emerging Horizons in Science, SGGSWU, Fatehgarh Sahib (2014).

6. Investigation of ^{206}Pb(n, α)^{203}Hg and ^{208}Pb(n, p)^{208}Tl reactions using collective clusterization approach, **Amandeep Kaur**, G. Sawhney and Manoj K. Sharma, National Confrence on Emerging challenges in Nucl. And Many body Physics (ECNMP), Jammu University, Jammu (2014).

7. Analysis of α and cluster-emission in superheavy nuclei, Gudveen Sawhney, **Amandeep Kaur**, Manoj K. Sharma, Raj K. Gupta, DAE symposium on Nuclear Physics, Vol. **60**, 178-179, SSSIHL, Prasanthi Nilayam, (A.P.), India (2015).

8. Decay of radio-active nucleus ^{238}U* formed in n-induced reaction using clusterization technique, **Amandeep Kaur**, Gurvinder Kaur and Manoj K. Sharma, National Conference on Application of Radioisotopes and Radiation Technology in Industry Healthcare and Agriculture (ARRTIHA), Department of Chemical Engineering, Thapar University, Patiala, India (2016).

9. Study of light charged particle emission from Pb-isotopes formed in n-induced reactions, **Amandeep Kaur**, Kiran Sandhu and Manoj K. Sharma, DAE symposium on Nuclear Physics, Vol. **61**, 576-577, Kolkata, India (2016).

10. Decay of exotic nucleus $^{191}\text{Ir}^*$ formed in α-induced reaction, **Amandeep Kaur** and Manoj K. Sharma, DAE symposium on Nuclear Physics, Vol. **62**, 638-639, TIET, Patiala, India (2017).

Contents

List of Tables

List of Figures

Abstract

This thesis covers a comprehensive analysis of the mechanism involved in the decay of compound nuclei formed in a variety of nuclear reactions lying in low energy regime. The use of various projectiles like n, p, α or heavy-ions leads to the formation of compound nuclei covering different mass regions of the periodic table ranging from light mass to super-heavy mass region. The methodology of Dynamical Cluster-decay Model (DCM) is employed to account for the decay of nuclear systems and the relevant information is extracted from the fragmentation structures and preformation profiles. This investigation of the dynamics governing the decay of compound nuclei not only help in enhancing the overall understanding of the dynamics involved, but also provide idea about certain properties which play eminent role in deciding the fragmentation patterns.

Here, the relative role of angular momentum and excitation energy of the decaying system is investigated along with the significance of nuclear deformations and orientations of the decaying fragments. Additionally, the role of the fragmentation potential has also been exercised by using two versions of proximity potential-Prox77 and Prox00 and two limits of moment of inertia-sticking (I_S) and non-sticking moment of inertia (I_{NS}) which helps in defining the centrifugal potential term. Moreover, the decay dynamics is also investigated for the inclusion of asymmetry dependence in Bulk constant (α) of liquid drop term and the radius term used in DCM calculations, for the inclusion of mass dependence in level density parameter ($a(A)$) and the suitable information is imparted from the modified fragmentation patterns. The descriptive presentation of the work done is provided in the seven chapters of the thesis and the segregation of these chapters is given as below:

Chapter-1 covers the general informative description regarding the nuclear reactions and the significance of the use of various projectiles is also explained. The nuclear decay mechanism is reported in this chapter along with the significance of

deformations-orientations and other parameters included in DCM like- level density parameter, its mass-dependence and asymmetry dependent terms. Also, this chapter provides the highlights of the compound nuclei taken in to consideration, the types of the reaction leading to these compound nuclei and the role of a particular projectile nucleus in defining the energetics of their respective decay paths.

Chapter-2 provides the details of the methodology used in achieving the objectives proposed in this work- the Dynamical Cluster-decay Model (DCM). This methodology is based on Quantum Mechanical Fragmentation Theory (QMFT) and explains the decay of a compound nucleus in terms of the preformation of the decaying fragments within the compound nucleus and penetration of these fragments through the Coulomb barrier. The cross-sections of a particular exit channel are estimated in terms of the preformation probability and barrier penetration probability, and the collective clusterization approach is followed which treats the possible exit channels simultaneously. The various nuclear interaction potentials used in solving the Schrödinger wave equation in mass coordinates are also described in this chapter. The details of the Preformed Cluster-decay Model (PCM), employed for ground state processes and PCM (T≠0) for excited state decays are also provided in this chapter.

Chapter-3, explains in detail, the dynamics of the decay of ^{240}Np* formed in n+^{239}Np reaction over an incident beam energy of E_n=0.62-18.75 MeV. The experimentally available data for fission decay channel is adequately addressed using the DCM. The calculations are done for spherical as well as quadrupole deformed choice of fragmentation and corresponding structural variations are analyzed. The experimentally available data showed triple humped variation for the fission cross-sections signifying maximas at $E_{c.m.}$=1.87, 8.75 and 16.92 MeV. The enhanced cross-sections are explained in terms of orientational degree of freedom of the decaying fragments by taking in to account the hot (equatorial) and cold (polar) configurations. In addition to this, the role of moment of inertia on the fragmentation structure is investigated via opting sticking (I_S) as well as non-sticking (I_{NS}) moment of inertia. Lastly, comparative analysis of the decay profile of ^{240}Np* with that of ^{238}U* formed under similar reaction conditions is carried out.

Chapter-4 provides the details explaining the decay of compound nucleus ^{61}Ni* formed in reaction n+^{60}Ni over an incident beam energy of E_n=1-100 MeV. The DCM methodology is used to address the cross-sections of formation of ^{57}Fe nucleus after α or $2p2n$-emission. It has been observed that, the same CN ^{61}Ni* decays via α-emission at low excitation energies and as the excitation energy is increased, the α-emission is replaced by $2p2n$-emission yielding same daughter nucleus. This transmutation has been explained in terms of the temperature-dependence of binding energies used in DCM. For this case, the calculations are done using non-sticking moment of inertia (I_{NS}). The effect of mass (and charge) of the CN on α and $2p2n$-emission is also investigated by considering similar reactions using different targets. Also, the analysis of the decay of the light mass nuclei formed in proton-induced reactions is also carried out where the compound nuclei ^{77}As*, ^{83}Br* and ^{86}Sr* formed in p+^{76}Ge, p+^{82}Se and p+^{85}Rb reactions are investigated for particle evaporation over incident beam energies of 1-5 MeV. The n-evaporation cross-sections are addressed using DCM and the effect of deformations of decaying fragments is also explored. In addition to this, the sensitivity of DCM calculated cross-sections towards level-density parameter (LDP) is also investigated by varying its value from $a = 6toa = 10$ and by including mass-dependence in LDP.

In **Chapter-5** the decay of ^{117}Sb*, ^{145}Pm* and ^{191}Ir* formed in α-induced reactions over an incident beam energy $E_\alpha\sim$ 10 to 15 MeV and $^{98,104}Cd^*$ formed in ^{40}Ca-induced reactions over an energy spread E_{Ca}=105-155 MeV are studied. It is to be noted that for types of reactions, the CN choose to decay via particle evaporation and the experimental data is adequately addressed within DCM approach. For α-reactions, the effect of mass of target nuclei (and hence the compound nuclei) on the decay pattern is investigated. Further, this analysis is extended on the basis of different asymmetry values (I=$\frac{N-Z}{A}$) of each decaying system and within this context, Bulk constant α used in liquid drop term of binding energy expression and the radius term R_i used in DCM based calculations is made I-dependent. The relative effect of these modified parameters α_{asymm} and R(I), emerges from the structural variations in fragmentation and preformation curves. While for the heavy-ion induced reactions ^{40}Ca+^{58,64}Ni, the isotopic analysis of the decay profiles of $^{98,104}Cd^*$ is carried out along with the analysis of the role of temperature and angular momentum on the fragmentation structure.

Chapter-6 presents the decay analysis of superheavy compound nucleus $^{297}118^*$ formed using heavy ion ^{48}Ca beam and transactinide target ^{249}Cf at excitation energies E^*_{CN}=29.2±2.5 and 34.4±2.3 MeV. This analysis is carried out for xn-evaporation from $^{297}118^*$ formed in the above-mentioned hot-fusion reaction using DCM and the calculations are done using two different of proximity potentials-Prox-77 and Prox00. The observations are recorded for the variations in barrier height V_B, barrier lowering parameter ΔV_B, potential energy surfaces and other DCM parameters when Prox00 is used in place of Prox77. Additionally a comprehensive analysis of the fragmentation profiles of superheavy nuclei with Z=113-118 formed in ^{48}Ca-induced reactions is also carried out to extract a better picture of the dynamics involved within. And finally, the half-lives of α-decay chains of ^{294}118 and the subsequent parent nuclei ^{290}116 and ^{286}114 occurring in the decay chain are addressed with the methodology of PCM and then by including T-dependence in it. In addition to this, the competition between the relative emergence of heavy clusters along with α-decay is also explored for various structural and related aspects.

Chapter-7 demonstrates the highlights of the work presented in this thesis, summarizing the results obtained and conclusions drawn. Along with this, the potential extensions of this work for near future endeavors is also drafted.

Chapter 1

Introduction

1.1 Time-line of the word 'nuclear'

Fascinated by the various events happening in this magical universe, the human brain has always been curious to dig deep into every bit of the observable surroundings and has tried to answer the assorted *whys* and *hows* that emerge during these explorations. The curiosity ship not only steered towards the grand, endless expanse of the universe, but also anchored deep into the miniature scaled atoms, nuclei and even to the elementary quarks. With the same motive of having a vital understanding of the weaving of this whole cosmos, the experimental and theoretical methods go hand in hand, with the experiments managing to gather details and data about the processes and theories try to explain the gathered information and predict further pathways in the related area. The continual ventures and deserving endeavors by scientists motivated towards the revelation of the X-rays in 1895 by Wilhelm Roentgen. This was the outset of digging in to the *"so-called"* indivisible atom and this discovery laid the foundation of the present day modern physics. In the three successive years (1896-1898), the discovery of radioactivity from natural Uranium by Henry Becquerel [1] and discovery of Po-209 and Ra-226 by Curie couple not only fetched them the Nobel Prize in 1903 but also proved to be the principle footsteps in the area of nuclear physics. In 1899, Rutherford [2] found that the Radiation from

Uranium is composed of two kinds of particles, one the readily absorbed-α-*particles* and the other having more penetrating power-β-*particles*, and when subjected to magnetic fields they get deflected in opposite directions signifying their opposite charges. In 1900, Becquerel proved the β-particles to be electrons and a new type of radiation having the highest penetration depth than any other radiation related with radioactivity, the γ-rays were discovered by P. Villard. Prior to the proposal of *nucleus* by Rutherford through the scattering experiment in 1911, a series of substantial discoveries were made in the emerging field of nuclear physics including-the radioactive decay laws and radioactive decay series explaining the spontaneous transformation of one element to another (parent→daughter) by Rutherford and Soddy in 1902-03 and identification of α-particle as ^{4}He-nucleus by Rutherford and T Royds in 1909. After that the nuclear physics broadened its branches accompanied by the discovery of deutron (Harold Urey, 1932), neutron (J. Chadwick, 1932) and the use of first particle accelerator by Sir J. Cockcroft and E. Walton [3] in the same year. Following this, the idea for a nuclear chain reaction was patented by L. Szidard(1934), artificial radioactivity was proposed by Joliot-Curie couple in 1934 and the very famous analogy of a nucleus with a drop of liquid leading to the derivation of Weizsacker formula [4] was achieved in 1935. In 1938, the division of a massive nucleus into lighter nuclei was observed i.e. the discovery of neutron-induced fission by O. Hahn, F. Strassman and L. Meitner. And very soon after this in 1942, Enrico Fermi [5] built the first nuclear reactor for the US Manhattan project followed by bombing at Hiroshima and Nagasaki in 1945. Mayers and co-workers established a model that explained the extra stability of some nuclides due to coupling of spin and orbital angular momentum terms-*the shell model* [6]. In 1959, the first breeder reactor started operating to produce electricity. In 1959, a model for deep-inelastic collision (DIC) [7] was proposed which involves grazing collision of nuclei forming a complex nucleus, that breaks up against Coulomb repulsion before the formation of stable compound nucleus. In 1967, Strutinsky introduced Shell corrections to the liquid drop energies which explained the asymmetric fission of nuclei. In 1970, a report on proton radioactivity was presented in which proton decay was observed from ground state ^{151}Lu nuclide by S. Hoffmann. 1984 is the year of cluster-decay of heavy nuclides that produced ^{14}C and many heavier clusters up to ^{34}Si. In 1986, the outbreak at Chernobyl power plant caused huge damage and made people believe that the word *"nuclear"* accompanies destructive activities. But such incidents did not prove to be a barrier in the growth of nuclear field and this regime continues to grow with immense scope of new possibilities, properties and applications.

1.2 Nuclear reactions

Nuclear physics provides a doorway to numerous research domains including nuclear engineering, nuclear medicines, radioactive dating and so on but one of the foremost and significant area of research is nuclear reactions and other nuclear structure and related phenomenon [8–13]. Simply, a nuclear reaction is defined as the interaction of two nuclei carrying energies sufficient enough to overcome the Coulombic repulsion between them and resulting in products either different or similar to the colliding partners. But the actual dynamics that govern these nuclear reactions is not so simple as it appears to be. The mechanism of every nuclear reaction is unique and depends upon target-projectile combination, the energy with which they collide, the angular momentum transferred, the impact factor between the colliding nuclides and so on. Hence, the knowledge of the energies and masses of the interacting nuclei, not only helps to understand the kinematics involved in the process but also leads us towards the segregation of nuclear reactions which further advances our know-hows about the reaction dynamics. The energy associated with these reactions has a wide expanse from a few MeV/nucleon to GeV/nucleon and hence drives us to categorize them as (a) low energy reactions, (b) intermediate energy reactions and lastly as, (c) high-energy reactions. The reactions limited to *low energy* are studied within an energy range of E$\leq$15 MeV/nucleon and mainly, the processes of fusion-fission, particle evaporation, intermediate mass fragments (IMFs) etc. are the topic of interest within this energy range. If the energy of the reaction is between 15-500 MeV/nucleon, this energy regime is called *intermediate energy* region and in this range processes like energy flow, multi-fragmentation, balance energy etc. are studied. When the energy is higher than 500 MeV/nucleon, the nucleon-nucleon interactions start coming into picture and this energy domain is referred to as *high energy region or particle physics* and one deals with elementary particles, quarks, mesons etc.

The present work is confined to low-energy domain only and the mechanisms involved in processes like particle evaporation, fusion-fission, decay of compound nucleus and its fragmentation structure etc. are studied. The projectile beam carries sufficient energy, overcomes the existing repulsive Coulomb barrier, gets amalgamated with the target nucleus resulting in to a longer living state called the *compound nucleus*, which afterwards de-excites via light particle emission or fission. During the young ages of nuclear physics, the energetic projectile beams were comprised of α-particles, β-particles and γ-rays which resulted from the radioactive decay from heavy mass nuclei. But with the advancement in the field, the particle accelerators were developed and were used to get beams of variable mass and energy. The advancement of particle accelerators helps in providing a broader energy window for the incident beams with sufficiently high intensities unlike the beam of α-particles obtained from a radioactive source. As the neutrons are not subjected to Coulomb barriers, so they are also used as projectiles. Here, the present work comprises of the decay analysis of compound nuclei having masses lying in different regions and formed using various projectile beams. The projectile beams include neutrons, protons, α-particles and other heavy-ion beams. The motive behind the use of various projectiles is to modulate the asymmetry of incoming channel which in turn controls the fraction of beam energy E_{beam} converted in to center of mass energy $E_{c.m.}$ and transferred to the fused system as its excitation energy E^*_{CN}. Generally, the energetic beam approaching the target nucleus, has to work against the exist-

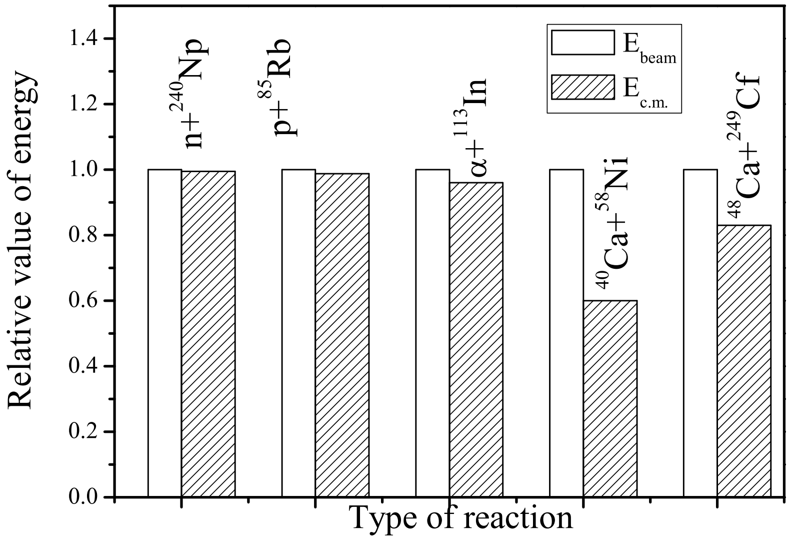

Figure 1.1: Relative value of E_{beam} and $E_{c.m.}$ with respect to the asymmetry of the incoming channel.

ing Coulomb barrier. For neutrons, the Coulomb barrier vanishes, but for protons, a noticeable barrier hinders the process of fusion and this magnitude of Coulomb barrier further increases as α-particle or other heavy ions are incident. Hence, a substantial amount of beam energy E_{beam} may be utilized in overcoming this fusion barrier and consequently different amount of energy will be transferred as excitation energy to the compound nucleus. Although the methodology used here, the Dynamical Cluster-decay Model (DCM), explained later, deals with analyzing the decay patterns and fragmentation structures of CN formed in various nuclear reactions, yet the significance of using a variety of projectiles emerges from the fact that this methodology finds it basis from the exchange of nucleons and transference of energy of incident channel ($E_{c.m.}$) to the excitation ($E_{CN}{}^*$) of the decaying fragments. These energies are related via following equations:

$$E_{c.m.} = \frac{A_T}{A_T + A_P} E_{beam} \tag{1.1}$$

and

$$E^*_{CN} = E_{c.m.} + Q_{in} \tag{1.2}$$

From eq.(1.1), it is clear that the conversion of beam energy E_{beam} in to K.E. of the incoming channel $E_{c.m.}$ may be attuned by varying the mass of projectile A_P. The greater the mass asymmetry (η_A=$\frac{A_T-A_P}{A_T+A_P}$) of the incoming channel, that means, the greater the difference between the mass of target (A_T) and projectile (A_P), larger fraction of the beam energy would be available for excitation of the compound system. This is evident from Fig. 1.1 where the relative values of E_{beam} and E$c.m.$ are outlined in terms of asymmetry of the incoming channel and it may be inferred that for highly asymmetric incident channels (using n and p as projectiles), 99% of the beam energy is converted while its value goes down to 60% for the reactions having low asymmetry of the incident channel (heavy-ion induced reactions). The Q-value of the incident channel, Q_{in} is defined as;

$$Q_{in} = B_P + B_T - B_{CN} \tag{1.3}$$

also plays its part in estimating the $E_{CN}{}^*$. On the basis of this kinematics, the various types of reactions which are the basis of this work are discussed briefly below:

n and p-induced reactions: Neutrons, being neutral in character are highly penetrating and can be ideally used as projectiles as whole of the energy of the projectile beam is transferred to the target because no Coulomb barrier exists in between. For proton beams, a part of the beam energy is utilized in overcoming the Coulomb barrier before its fusion in the target nucleus. The novelty of using neutron and proton beams lies in the fact that the fusion of a neutron and proton in the target nucleus raises its atomic mass by 1 unit (and charge by 1 unit in case of proton induced reactions) and it would be of quite interest to explore the fragmentation structure of the compound nuclei formed in n and p-induced reactions and to extract information regarding the effect of such high mass asymmetry in the incoming channel on decay dynamics. Also, the center of mass energy ($E_{c.m.}$) for such highly asymmetric incoming channel is almost equivalent to beam energy (depicted in Fig.1.1) as defined by eq. (1.1);

$$E_{c.m.} = \frac{A_T}{A_T + A_P} E_{beam} \simeq E_{beam} \tag{1.4}$$

In this work, the n-induced reactions are studied for two types of compound nuclei-one heavy mass system ^{240}Np* which decays via fission and another light mass ^{61}Ni* which decays via light particle evaporation. Also, the decay of the compound systems ^{77}As*, ^{83}Br* and ^{86}Sr* formed in the corresponding p-induced reactions is investigated for the comprehension of mechanisms involved in p-induced reactions and the details are provided in subsequent chapters.

α and heavy-ion induced reactions: α-particles and ions with A>4 and Z>2 (i.e. heavy ions) have always played an eminent role in nuclear probing techniques. When energetic beams of α-particles and heavy-ions are incident on the target nucleus, they transfer their energy and momentum to form an amalgamated nuclear stage which disintegrates against Coulombic repulsions, and hence the effects of energy, mass or the transferred angular momentum can be extracted from the fragment yields. For α-particles, the beam energies (E_{beam}) are transferred to the target nucleus in such a way that it assigns different $E_{c.m.}$ values because of difference in the mass of target (A_T) and the amalgamated or the equilibrated stage so formed (A); $E_{c.m.} < E_{beam}$ (as defined by eq.(1.1)) and it becomes $E_{c.m.} \ll E_{beam}$, as projectiles of heavier masses as used further(depicted in Fig.1.1). This transference of energy of the incoming reaction channel to the excitations of the outgoing channel is explained in Chapter-2.

In apprehension to this, the decay of ^{117}Sb*, ^{145}Pm* and ^{191}Ir* formed in α-induced reactions and ^{98,104}Cd* formed in reactions induced by heavy-ions, is scrutinized and the relevant details are provided in the following chapters.

Super-heavy nuclei: Ever since the human brain has started to solve the mazes of nature, it is unveiled that there are only 92 natural elements and as the periodic table hits Z=92, it felt as if this is the end of the stable continent of elements. But the worthy researches that were carried out in the domain of nuclear physics, helped in expanding the boundaries of above mentioned stable continent of elements and it started with the discovery of Neptunium (Z=93) and Plutonium (Z=94) in 1935. Later on within a span of a decade, the tail end of the periodic table reached Z=101. Various theoretical formulisms and experimental methods were put forward to go beyond Z=101 as at this high value of Z, the Coulombic repulsions between the protons starts superseeding; leading to disintegration of the nucleus before it touches the stable life-time.

After 1960, the eminent theoreticians Myers and Swiatecki [14], Nilsson *et al.* [15, 16], Mosel and Greiner [17], Fizet and Nix [18], Randrup *et al.* [19] were on a quest to look for the island of stability for super-heavy nuclei i.e. the next doubly magic Z and N values after Pb (Z=82 and N=128). Various experimental ventures have always been carried out at Lawrence Berkeley Laboratory (USA), Joint Institure of Nuclear Research (JINR, Dubna), and Gesellschaft für Schwerionenforschung (GSI) near Darmstadt (Germany) in accordance with these theoretical paths and predictions. The Lawrence Berkeley Laboratory (USA) tried to overcome the repulsion between the protons for elements with Z>100, by impinging the target with a nuclear flux instead. But the super-heavy nuclei synthesized by this method failed to meet the stable life-time limits.

Eventually, to synthesize super-heavy nuclei, the following three techniques were manifested-(i)**Cold fusion:** Within this method, the beam of neutron rich isotopes of elements from *Ca* to *Zn* were fused with **Pb** and **Bi** targets, and this method successfully extended the periodic table from Z=102 to Z=112. The nomenclature of this method corresponds to the orientations of the interacting nuclei so as to possess "lowest interaction barrier" and "largest interaction radius" and hence this fusion refers to a non-compact (elongated) fusion forming compound nuclei with excitation energies <20 MeV. Also, the compound nucleus is subjected to evaporation of 1 or 2 neutrons. This theoretical description was developed by Greiner and collaborators [20]- [31] and is based on Quantum Mechanical Fragmentation Theory (explained in Chapter-2) based on two center shell model and Strutinsky macroscopic-microscopic approach. In the following years, the experimental facilities available at Dubna [32] were successful to synthesize super-heavy nuclei up to Z=106 and by using the advanced accelerator and detector techniques at Darmstadt [33]- [38], the count of the highest proton number in periodic table reached up to Z=112.

(b)**Hot fusion:** The second method to synthesize super-heavy nuclei is via *'hot fusion'* reactions. Just like cold fusion reactions, the 'hot-fusion' also refers to the orientations of the fusing nuclei and corresponds to 'highest interaction barrier' and 'smallest interaction radius'. The compound nucleus excitation energies are higher than that of cold fusion reactions and reach up to 35 MeV. The compound nuclei de-excite via evaporation of 3 or 4 neutrons. This category also includes a sub-division of 'very hot' fusion reactions and these reactions correspond to compound nucleus excitation energy up to 50 MeV and the neutrons emitted from the compound system is greater than 4 in number. Theoretically, hot (and very hot) fusion reactions are also explained on the basis of QMFT and experimentally, these reactions proceed through the fusion of energetic beam of ^{48}Ca with **actinide** targets with Z=90-98. The super-heavy elements with Z>113 are successfully synthesized via hot fusion reactions at Dubna [39]- [43] and the cross-sections for 3n, 4n (and 5n in some cases) are recorded.

(c)Lastly, the third kind of reactions used for the synthesis of super-heavy nuclei is making use of ^{22}Ne and ^{26}Mg beams on actinide targets (^{248}Cm and ^{248}Bk). These reactions proceeds like hot fusion reactions, there by making neutron rich super-heavy compound systems; de-exciting via 4 or 5n evaporation and having substantial lifetimes.

For the interpretation of dynamics supervising the decay of superheavy nuclei, the present work covers the details of decay of $^{297}118^*$ formed in heavy ion induced reactions using transactinide target nucleus and the relevant details are provided in the following chapters.

1.3 Reaction mechanism and modes of decay

The interaction of the incoming nucleus with the target nucleus depends on many factors such as energy of the incoming beam, the impact parameter, the plane of collision and the deformations of the nuclei taking part in a nuclear reaction. Every factor plays a vital role and govern the reaction dynamics, providing us with an insightful picture of the fusion-fission process. If the bombarded nucleus carry energy so as to overcome the repulsive Coulomb barrier of the target nucleus and, is incident with minimum impact factor and interacts at the precisely optimized orientations, then the resulting nucleus formed after the fusion of the two nuclei is supposed to be in the most stable configuration. Understanding the crucial part played by the aforementioned factors, Niels Bohr, in 1936 [44], formulated a theory characterizing the systematics followed during a nuclear reaction. Bohr, in his theory, postulated that the kinematics supervising nuclear reactions is basically a dual-step process. *First step* involves the equilibrated amalgamation of the incident nucleus with in the target nucleus provided the energy carried by the incoming nuclei is adequate enough to overcome the mutual Coulombic repulsion. This composite system, having mass equal to the sum of the mass of projectile (A_P) and target (A_T), is called *compound nucleus* (CN) and has a relatively longer life-time($\sim 10^{-14}$ s) as compared to nuclear time scale($\sim 10^{-23}$ s). This longer life-time is attributed to the time during which the energy of the incoming nucleus is distributed equally amongst all the nucleons stabilizing all the degrees of freedom. The *second step* proceeds through the de-excitation of this energetic intermediate stage through particle evaporation or through binary fragmentation and while the intermediate compound nucleus steers towards its disintegration, it forgets the mode of formation. Later on, the theory of Bohr was verified experimentally by Ghoshal and collaborators [45] and this hypothesis helped in exploring the reaction dynamics.

Within the compound nucleus, there is continuously a struggle between the attractive nuclear forces and repulsive electrostatic forces and eventually, the energetic compound system disintegrates against the repulsive forces. The decay path chosen by the CN depends upon the energy and mass of the system (A_{CN}). The emission of lights particles, clusters or fission fragments from a CN is treated via quantum mechanical tunnelling of these fragments across the Coulomb barrier [46]. The various modes opted by the CN are explained below:

(a) Neutron evaporation: At moderate excitations, the emission of charged particles or massive clusters from the CN is hindered because of the existing Coulomb barrier, hence, the CN prefers to decay via emission of few neutrons. The compound system de-excites through the neutron evaporation and a corresponding stabilized isotope is formed as a daughter nucleus. If the excitations are between E_{CN}^*=10-20 MeV, 1 or 2 neutrons evaporate from the CN leaving the isotopic daughter nucleus behind while, if excitations are higher, then the stabilization or de-excitation of the CN may require 3 or more neutrons.

(b)Evaporation Residue (ER) mode: For the compound system masses ranging from A_{CN}=50-100, there is a lesser possibility of the compound system to follow fission path. Hence, the compound system de-excites via emitting light charged particles like protons, deutrons or α-particles. The compound nucleus stabilizes by emission of fragments with $A \leq 4$ and $Z \leq 2$ there by forming a highly asymmetric exit channel and the process is referred to as particle evaporation; leaving behind the daughter nucleus which is referred as *evaporation residue.*

(c)Fusion-fission mode: As the mass of the compound system exceeds 200, the system ruptures under Coulombic agitation and prefers symmetric decay mode which includes fission fragments having almost same masses ($=\frac{A_{CN}}{2}$). Also, if the decaying channel becomes asymmetric i.e. in case the mass of one fragment is greater than the other, then the emitted channel is termed as asymmetric fission (AF) with the mass range $\frac{A_{CN}}{2} \pm 20$. In addition to this, for the compound systems with intermediate mass A_{CN}~100, fragments with masses A=5-20 and Z=2-10 form the competing decay mode and the emitted fragments are called intermediate mass fragments (IMF). Sometimes there could be emergence of fragments heavier than IMF and smaller than AF, such fragments are called heavy mass fragments (HMFs). The present work comprises of the analysis of the decay modes opted by the compound systems formed in the aforementioned reactions using a variety of projectiles. This analysis is done within the clusterization mechanism of the Dynamical Cluster-decay Model (DCM) [47]- [60] which treats all of these exit channels on equivalent basis.

In certain cases, when a projectile nucleus tries to fuse in to the target nucleus, the complete equilibration of energy within all the nucleons is hindered and the nuclear reaction may not proceed via compound nuclear mechanism. In such cases, another reaction dynamics- quasi-fission [61], deep inelastic collision [62, 63], incomplete fusion [64] etc. start competing. These are the non-equilibrated processes and hold similar significance as that of equilibrated processes for understanding nuclear reaction dynamics and other related aspects. These processes have life-times relatively longer than nuclear time scales but shorter than that of compound nuclear processes.

1.4 Significance of various parameters used in DCM

(a) Nuclear deformations and orientations:

In addition to the above explained parameters of energy as well as mass of the interacting nuclei, another important criteria which can govern the reaction

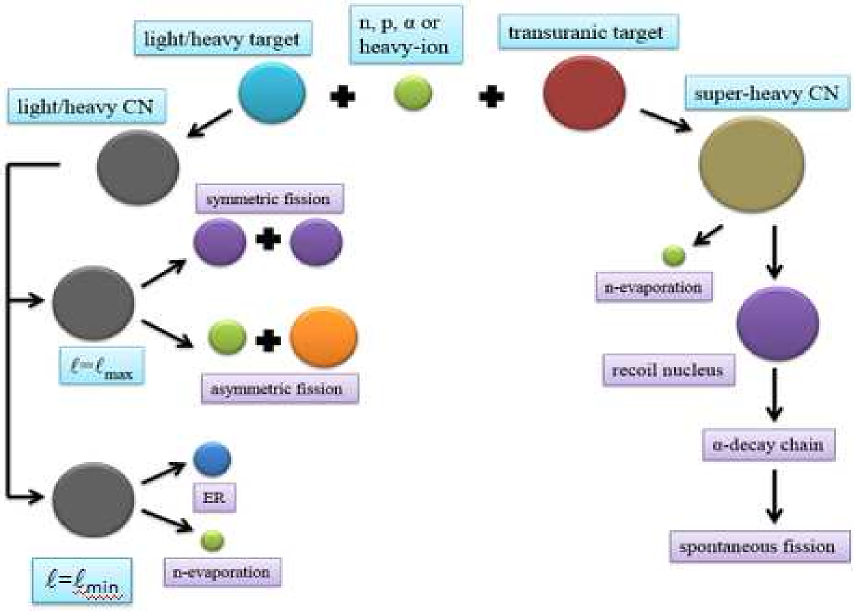

Figure 1.2: Illustration of the fusion and decay processes involving various projectiles and target combination along with it the effect of angular momentum and deformations is also shown.

dynamics is the shapes of the nuclei taking part in a nuclear reaction. The shapes of the target and projectile may be as simple as two interacting charged spheres or they may have extreme shapes (elongated or flattened) depending upon the neutron to proton ratio. The shapes merely give an idea about the distribution of charge and mass and eventually, the knowledge of deformations proves to be crucial for a deeper insight of nuclear reactions and related dynamical phenomenon. The commendation of probing the deviation of a nucleus from spherical shape goes to Schuler and Schmidt (1935) [65]. This deviation of charge (and mass) distribution is defined in terms of quadrupole moment (β_2) and this is the lowest state of deformation. If the nucleus possess this deformation, the shape is elongated (prolate) and flattened (oblate) and respectively, β_2>0 and β_2<0 [66]. Experimentally, it has been found that a majority of nuclei prefer to have prolate shape while a very few are seen to be octupole deformed [67–69]. Various nuclei may possess higher order deformations with λ=3, 4 or they may also be super-deformed but the presented work includes up to quadrupole deformations (β_2) only. The role of β_2-deformations is analyzed for the decaying compound nuclei ^{240}Np* formed in n-induced reaction, ^{77}As* formed in p-induced reactions, ^{191}Ir* formed in α-induced reaction and finally for the decaying system $^{297}118^*$ formed in heavy-ion induced reactions lying in superheavy mass region. The observations are reported in subsequent parts of this thesis.

As the deformations of the colliding nuclei are taken in to account, we get a number of combinations for their interaction along the collision axis. Every configuration at which the two deformed nuclei collide will have their unique interaction radius and interaction barrier. This means the orientations of the two colliding nuclei play as much significant role as is played by the deformations. Every angle at which the two nuclei approach and interact will leave us with unique set of potentials (Coulomb and proximity) and hence play vital role in analyzing various distinctive features of reaction dynamics. Hence, there exists a peculiar orientation for both the interacting nuclei at which the interaction radius and interaction barrier are optimized so as to result in to relatively stable and long-lived compound nucleus. This analysis has been worked upon by Gupta and collaborators [70, 71] within the quantum mechanical fragmentation approach (QMFT) where the orientations are optimized for fusing β_2 deformed nuclei. In this thesis, the two optimum orientations- hot (equatorial) and cold (polar) are incorporated to investigate their significance in DCM based calculations. In the present work, the inclusion of orientational degree of freedom of the decaying fragments has been investigated for decaying ^{240}Np* formed in n+^{239}Np reaction and the corresponding structural variations are analyzed to extract the relevant information imparted. The decay is studied for equatorial and polar configurations. and the details are presented subsequently.

(b) Angular momentum and temperature effects: Another important parameter for DCM based calculations is angular momentum (ℓ) and temperature (T_{CN}) of the decaying compound system. It has been well known that the DCM calculated cross-sections follows the partial wave mechanism and the resultant cross-sections are estimated by summing the preformation probability P_0 and barrier tunnelling probability P over the ℓ-values. Also, the ℓ-values find its significance in evaluating the centrifugal potential (V_ℓ), as explained in Chapter-2 and as a consequence, the fragmentation structure will also be a function of angular momentum. Hence, the angular momentum plays an eminent role in context to the DCM framework which emerges from the variations in the decay profiles when studied at different ℓ-values. The role of the angular momentum values on the decay path opted by the decaying compound systems has been analyzed for $^{240}Np^*$, $^{61}Ni^*$ formed in n-induced reactions, for $^{77}As^*$, $^{83}Br^*$ and $^{86}Sr^*$ formed in p-induced reactions, for $^{117}Sb^*$, $^{145}Pm^*$ and $^{191}Ir^*$ formed in α-induced reactions and also for the decay of $^{98,104}Cd^*$ and $^{297}118^*$ formed in heavy ion induced reactions. The significance of ℓ, as reflected from the DCM calculations is presented in this work in subsequent chapters.

Secondly, it may be well explained in the Chapter-2 that the excited compound nucleus having energy $E_{CN}{}^*$, is imparted a certain temperature T_{CN} which is an important parameter for DCM calculations as the other parameters like radius term R_i, binding energy B_i of the interacting nuclei show better comparison with experimentally available data when the T-dependence is included. Henceforth, the significance of the dependence of these parameters on T is also investigated and the corresponding results are discussed in this work. This dependence of T has been specifically investigated for the binding energies used in DCM and the corresponding effect on the choice of exit channel is investigated for the decay of $^{61}Ni^*$.

(c) Level density parameter a: Statistically, the level density parameter is an important parameter and helps in deciding the distribution of energy amongst the available states. The methodology of DCM proceeds through the transference of energy of the incoming channel $E_{c.m.}$ to the internal excitations of the decaying fragments $E_{CN}{}^*$. Consequently, the significance of level density parameter in DCM arises from here, that if the number of nuclear levels available are modulated, it will result in to modifications in T_{CN}, as explained above and consequently, the parameters depending on T_{CN} will further be attuned and it is quite interesting to analyze these variations. Usually, within DCM, the values of level density are fixed as a=9 for heavy nuclei and a=11 for superheavy nuclei but the present work involves the analysis of the sensitivity of DCM based calculations towards the level density parameter a by varying its value and further to extend this analysis, the mass dependence is also included the level density parameter $a(A)$. These variations are included for the decay of ^{77}As* and the corresponding observations are discussed in the following chapters. The mass dependence in LDP is included in ref. to [72].

(d) Inclusion of neutron-proton asymmetry I:

The rich literature available in the field of nuclear physics is a reflection of the fact that the stability of heavier nuclei demands the excess of neutrons over protons, there by making the neutron to proton asymmetry, I defined as $I = \frac{N-Z}{A}$, as an important parameter whose role in the reaction dynamics can never be ignored. In apprehension of extracting important information in this regard, the Bulk constant α used in Liquid Drop binding energies and the radius terms R_i used in DCM calculations are made I-dependent and the consequent effects on the fragmentation structure, preformation profiles, barrier tunnelling probability and hence on the overall reaction cross-sections are analyzed and well presented in this thesis. The asymmetry-dependence in Bulk constant α is included in ref. to [73] while the neutron-proton asymmetry dependent radius term R_i is taken from [74]. These effects are studied for the decay of ^{191}Ir* formed in α-induced reactions and the relevant details are discussed.

1.5 Motivation behind the work

This thesis presents the analysis of nuclear reaction mechanism explaining the decay of a variety of CN formed in nuclear reactions using different projectiles. The main emphasis of the work is to apply collective clusterisation technique of DCM to address the following points: (i) dynamics of neutron, proton and α-induced reactions and associated dynamical aspects (ii) use of heavy-ion projectiles to synthesize heavy/superheavy nuclear systems and analysis of their subsequent decay (iii) particle evaporation and production of various isotopes of heavy/superheavy nuclei and (iv) finally to compare the reported observations with available experimental results.

The details of the work done is presented in Chapters 3-6 in this thesis.

1.6 Layout of the thesis

The thesis is following the underlying layout:

Chapter 2 describes the methodology on which the calculations of the present work are based- *the dynamical cluster-decay model (DCM)* [47]- [60]. This chapter presents a brief account of the quantum mechanical fragmentation theory (QMFT) which forms the basis of the DCM model. This methodology proceeds via conversion of the beam energy E_{beam} to center of mass energy $E_{c.m.}$ (which is controlled by the asymmetry of the incoming channel) and hence to the excitation energy $E_{CN}{}^{*}$ of the exit channel. It is explained very well in this chapter that DCM is a two-step process- first step involves the estimation of the probability with which the decaying fragments are pre-born within the compound nucleus prior to the decay i.e. the *preformation probability* P_0 and second step involves the application of WKB approximation to calculate the probability of these preformed fragments to tunnel through the existing Coulomb barrier i.e. *the barrier tunnelling probability P or penetrability.* The fragmentation potential used in solving the stationary state Schrödinger wave equation to calculate P_0 consists of macroscopic part (LDM energy), microscopic part (shell corrections), Coulomb potential, centrifugal potential and the proximity potential. The relevant details of these potential terms are provided in this chapter along with the temperature, angular momentum and deformation dependent terms. The details of the two versions of proximity potential used in the present calculations i.e. Prox77 and Prox00 and the two limits of centrifugal potential term i.e. sticking I_S and non-sticking I_{NS} is also discussed. The tunnelling of the fragments through the potential barrier is explained in view of WKB approximation and the barrier characteristics like $V(R_a)$, V_B and barrier lowering parameter ΔV_B etc. are also defined analytically as well as graphically. Lastly, the PCM (T=0) for ground state decays, α-decay chains, cluster emission etc. is explained and the concept of recoil energy which transforms PCM for excited state decays i.e. T$\neq$0 is briefly accounted.

Chapter-3 provides a descriptive analysis of the neutron-induced reactions having a highly asymmetric incoming channel. The dynamics involved in the decay of compound nucleus ^{240}Np* formed in n+^{239}Np reaction [75] over an incident energy range of E_n=0.62-18.75 MeV are investigated in context to fission decay because of the heavier mass of the compound system so formed. This endeavor highlights the significance of deformations and orientations in context to DCM based calculations. The excitation functions for the decay of ^{240}Np* show a triple-humped variation as a function of energy showing maximas at $E_{c.m.}$=1.87, 8.75 and 16.92 MeV and this enhancement in cross-sections may be explained on the basis of inclusion of orientational degree of freedom of the decaying fragments. Also, the impact of moment of inertia on the decay profile of the compound system ^{240}Np* is also worked upon by opting I_S and I_{NS} approach and the relative role of moment of inertia in context to n-induced reactions is investigated. Lastly, the decay profile of ^{240}Np* is compared with that of ^{238}U* formed in similar reaction conditions is carried out.

Chapter-4 presents the analysis of n and p-induced reactions where the light mass compound nuclei are formed and they decay via particle evaporation. Here, the decay analysis of the compound nucleus ^{61}Ni* formed in n+^{60}Ni reaction is carried out over a wide energy spread of E_n=1-100 MeV in context to particle evaporation, using collective clusterization approach of DCM. The experimentally available [76] excitation functions for this decay reveals α-emission at low energies while at higher energies, multi-nucleon emission is observed leading to the same daughter nucleus.

This transmutation is well explained in terms of the temperature dependence of the binding energies used in DCM based calculations. The calculations are done by opting the non-sticking limits of moment of inertia I_{NS} and the calculated results agree fairly with the experimental data. Also, the effect of mass of compound nucleus on α and 2p2n emission is exercised by choosing different compound systems with masses varying from A=17-93 and the comparisons are done to get a better picture of the dynamics involved. In addition to this, the analysis of proton-induced reactions is carried out where the decay of ^{77}As*, ^{83}Br* and ^{86}Sr* via n-evaporation, formed in p+^{76}Ge, p+^{82}Se and p+^{85}Rb reactions at incident beam energy range of 1-5 MeV [77–79] is investigated. The comparative analysis of the decay profiles of the chosen compound systems is done at common incident energy (E_{beam}=3.6 MeV). The importance of deformations and angular momentum is also explored in this work. Along with this, the sensitivity of DCM calculated cross-sections towards the choice of level density parameter is also investigated and for this purpose, the magnitude of LDP is varied from $a = 6toa = 10$ along with inclusion of mass dependence in LDP.

Further, the **Chapter-5** comprises of the detailed analysis of α-induced and heavy-ion induced reactions, as the use of projectiles heavier that n and p i.e. the use of α and heavy-ions leads to a decrement in the asymmetry of the incoming channel. To pursue this, the dynamics of α-induced reactions are worked out over an incident beam energy E_α=10-15 MeV and the decay profiles of ^{117}Sb*, ^{145}Pm* and ^{191}Ir* formed using α-particle as a projectile are investigated for particle evaporation (n-emission). The cross-sections estimated by DCM, finds nice agreement with the experiential data [80–82] and the chosen systems are such that they cover a wide range of compound nuclear mass A_{CN}=117-191, providing us with an opportunity to explore various aspects related to reaction dynamics. The Bulk constant α of the LDM expression and the radius term R_i are made asymmetry dependent and the subsequent effect on the reaction dynamics is also explored in terms of modified fragmentation structure, preformation profiles and other barrier characteristics like barrier position R_B and barrier height V_B. The other part of this chapter deals with the analysis of reactions using heavy-ions as projectiles and here, the decay analysis of the compound nuclei $^{98,104}Cd^*$ formed in ^{40}Ca-induced reactions is analyzed. The calculations are done by including the quadrupole deformations of the decaying fragments and the evaporation residue cross-sections are fitted nicely in accordance to experimentally available data [83] over wide energy range $E_{c.m.}$=64-88 MeV. The isotopic analysis is done for the compound systems $^{98,104}Cd^*$ and their decay patterns are compared at common beam energy with the inclusion of angular momentum and temperature effects.

The Chapter-6 deals with the decay analysis of superheavy mass nuclei $^{297}118^*$ formed in ^{48}Ca-induced reaction using transactinide target nuclei ^{249}Cf. Here, the reaction dynamics involved in the decay of super-heavy nuclei $^{297}118^*$ is investigated for 2n, 3n and 4n emission within the framework of DCM at excitation energies E_{CN}^*=29.2 and 34.4 MeV [84, 85]. In addition to this, the residual nucleus $^{294}118$ formed after 4n evaporation from the nucleus $^{298}118*$ is also analyzed to check the possibility of mixing of ^{250}Cf isotope along with ^{249}Cf. The decay patterns are investigated to extract the role of deformations, angular momentum and proximity potentials in DCM based calculations. In addition to this, the role of proximity potential in context to the study of α-decay chains using ground state PCM (with T=0) and PCM for excited states (T$\neq$0) is analyzed by opting two different versions of the proximity potential namely-Prox77 and Prox00. The excited state PCM is defined by introducing the concept of recoil energy left with the residual nucleus $^{294}118$ after 3n-evaporation from $^{297}118^*$. The α-decay chains and the most probable cluster are also studied for $^{294}118^*$ and the subsequent parent nuclei appearing in the α-decay chain-$^{290}116^*$ and $^{286}114^*$. Lastly, the half-lives are calculated for the heavier clusters-^{86}Kr, ^{84}Se and ^{80}Ge, corresponding to the doubly magic ^{208}Pb daughter nucleus.

Chapter-7 briefs the over all work presented in this thesis along with the future aspects of the work.

Bibliography

[1] H. Becquerel, C. Rendus **122**, 420 (1896).

[2] E. Rutherford, Phil. Mag. **37**, 581 (1919).

[3] J. D. Cockcroft and E. T. S. Walton, Proceedings of the Royal Society A, **136**, 619-630 (1932).

[4] C. F. V. Weizsäcker, Z. Physik **96**, 7-8, 431-458 (1935).

[5] E. Fermi, Proceedings of the American Philosophical Society **90**, 20-24 (1946).

[6] M. G. Mayer, Phys. Rev. **75**, 1969 (1949); O. Haxel, D. Jensen, and H. E. Suess, Phys. Rev. **75**, 1766 (1949).

[7] R. Kaufmann and R. Wolfgang, Phys. Rev. **121:192** (1961).

[8] A. Shukla, P. K. Raina, R. Chandra, P. K. Rath, J. G. Hirsch, Euro. Phys. Jour. A 23(2): 235-242 (2005).

[9] D. Singh, Arun Bharti, A. Kumar, S. Singh, G. H. Bhat and J. A. Sheikh, Int. Jour. Mod. Phys. E Vol. 26, no. 6 1750041 (2017).

[10] S. Mahapatro, C. Lahiri, B. Kumar, R. N. Mishra and S. K. Patra, Int. our. Mod. Phys. E 25, 1650062 (2016).

[11] R. Kumar, V. R. Sharma, A. Yadav, P. P. Singh, A. Agarwal, S. Appannababu, S. Mukherjee, B. P. Singh, R. Ali and R. K. Bhowmik, Phys. Rev. C 96, 054614 (2017).

[12] A. Choukri, J. L. Reyss, L. Turpin, and M. Berrada, Radiochemica Acta 65, 137-139 (1994).

[13] K. Kim, Y. Kim, A. K. Nasirov, G. Mandaglio, G. Giardina, Phys. Rev. C 91, 064608 (2015).

[14] W. Myers and W. J. Swiatecki, Nucl. Phys. **81**, 1 (1966).

[15] S. G. Nilsson, J. R. Nix, A. Sobiczewski, Z. Szymanski, S. Wizech, C. Gustafson and P. Möller, Nucl. Phys. A **115**, 545 (1968).

[16] S.G. Nilsson, C.F. Tsang, A. Sobiczewski, Z. Szymanski, S. Wycech, C. Gustafson, I. L. Lamm, P. M¨oller and B. Nilsson, Nucl. Phys. A **131**, 1 (1969).

[17] U. Mosel and W. Greiner, Z. Phys. **222**, 261 (1969).

[18] E.O. Fizet and J.R. Nix, Nucl. Phys. A **193**, 647 (1972).

[19] J. Randrup, S.E. Larsson, P. M¨oller, A. Sobiczewski and A. Lukasiak, Phys. Scr. **10A**, 60 (1974).

[20] J. Maruhn and W. Greiner, Phys. Rev. Lett. **32**, 548 (1974).

[21] R.K. Gupta, W. Scheid and W. Greiner, Phys. Rev. Lett. **35**, 353 (1975).

[22] A. Săndulescu, R.K. Gupta, W. Scheid and W. Greiner, Phys. Lett. **60B**, 225 (1976).

[23] R.K. Gupta, A. Săndulescu and W. Greiner, Phys. Lett. **67B**, 257 (1977); Rev. Roum. Phys. **23**, 51 (1978).

[24] S. Yamaji, W. Scheid, H.J. Fink and W. Greiner, Z. Phys. A **278**, 69 (1976).

[25] S. Yamaji, W. Scheid, H.J. Fink and W. Greiner, J. Phys. G: Nucl. Phys. **2**, L189 (1976).

[26] S. Yamaji, K.H. Ziegenhain, H.J. Fink, W. Greiner and W. Scheid, J. Phys. G: Nucl. Phys. **3**, 1283 (1977).

[27] R. K. Gupta, A. Săndulescu and W. Greiner, Z. Naturforsch. **32a**, 704 (1977).

[28] R. K. Gupta, C. Pirvulescu, A. Săndulescu and W. Greiner, Z. Physik A **283**, 217 (1977); Sovt. J. Nucl. Phys. **28**, 160 (1978).

[29] R.K. Gupta, Z. Physik. A **281**, 159 (1977).

[30] A. Săndulescu, H. J. Lustig, J. Hahn, and W. Greiner, J. Phys. G: Nucl. Phys. **4**, L279 (1978).

[31] H. J. Lustig, J. A. Maruhn, and W. Greiner, J. Phys. G: Nucl. Phys. **6**, L25 (1980).

[32] Yu. Ts. Oganessian *et al.*, Nucl. Phys. A **239**, 157 (1975).

[33] S. Hofmann *et al.*, Z. Phys. A **350**, 277 (1995).

[34] S. Hofmann *et al.*, Z. Phys. A **350**, 281 (1995).

[35] S. Hofmann, Rep. Prog. Phys. A **61**, 639 (1998).

[36] S. Hofmann *et al.*, Eur. Phys. J. A **10**, 5 (2001).

[37] S. Hofmann *et al.*, Eur. Phys. J. A **14**, 147 (2002).

[38] S. Hofmann *et al.*, Z. Phys. A **354**, 229 (1996).

[39] Yu.Ts. Oganessian *et al.*, Eur. Phys. J. A **5**, 63 (1999); **19**, 3 (2004).

[40] Yu.Ts. Oganessian *et al.*, Phys. Rev. C **69** 021601(R) (2004).

[41] Yu.Ts. Oganessian *et al.*, Phys. Rev. C **69** 054607 (2004).

[42] Yu.Ts. Oganessian *et al.*, Nature (London) **400**, 242 (1999).

[43] Yu.Ts. Oganessian *et al.*, Phys. Rev. C **63** 011301(R) (2000).

[44] N. Bohr, Nature (London) **137**, 344 (1936).

[45] S N Ghoshal, Phys. Rev. **80**, 939 (1950).

[46] P. E. Hodgsona, E. Betak, Phys. Rep. **374**, 1 (2003).

[47] R. K. Gupta, R. Kumar, N. K. Dhiman, M. Balasubraniam, W. Scheid, and C. Beck, Phys. Rev. C **68**, 014610 (2003).

[48] M. Balasubraniam, R. Kumar, R. K. Gupta, C. Beck, and W. Scheid, J. Phys. G **29**, 2703 (2003).

[49] B. B. Singh, M. K. Sharma, and R. K. Gupta, Phys. Rev. C **77**, 054613 (2008).

[50] R. K. Gupta, M. Balasubraniam, R. Kumar, D. Singh, and C. Beck, Nucl. Phys. A **738**, 479c (2004). R. K. Gupta, M. Balasubramaniam, R. Kumar, D. Singh, C. Beck, and W. Greiner, Phys. Rev. C **71**, 014601 (2005).

[51] B. B. Singh, M. K. Sharma, R. K. Gupta, and W. Greiner, Int. J. Mod. Phys. E **15**, 699 (2006).

[52] S. Kanwar, M. K. Sharma, B. B. Singh, R. K. Gupta, and W. Greiner, Int. J. Mod. Phys. E **18**, 1453 (2009). S. K. Arun, R. Kumar, and R. K. Gupta, J. Phys. G: Nucl. Part. Phys. **36**, 085105 (2009).

[53] M. K. Sharma, S. Kanwar, G. Sawhney, R. K. Gupta, and W. Greiner, J. Phys. G: Nucl. Part. Phys. **38**, 055104 (2011); D. Jain, R. Kumar, M. K. Sharma, and R. K. Gupta, Phys. Rev. C **85**, 024615 (2012).

[54] M. K. Sharma, G. Sawhney, R. K. Gupta, and W. Greiner, J. Phys. G: Nucl. Part. Phys. **38**, 105101 (2011). M. K. Sharma, G. Sawhney, S. Kanwar, and R. K. Gupta, Mod. Phys. Lett. A **25**, 2022 (2010).

[55] G. Sawhney and M. K. Sharma, Eur. Phys. J. A **48**, 57 (2012). M. K. Sharma, S. Kanwar, G. Sawhney, and R. K. Gupta, Phys. Rev. C **85**, 064602 (2012).

[56] M. Kaur, R. Kumar, and M. K. Sharma, Phys. Rev. C **85**, 014609 (2012).

[57] M. Kaur and M. K. Sharma, Phys. Rev. C **85**, 054605 (2012). M. Kaur, M. K. Sharma and Raj K. Gupta, Phys. Rev. C **86**, 064610 (2012).

[58] M. Kaur and Manoj K. Sharma, *International Conference On Recent Trends in Nuclear Physics-2012*, published in AIP conf. proc. **1524**, pp.151-154 (2013).

[59] K. Sandhu, M. K. Sharma, and R. K. Gupta, Phys. Rev. C **85**, 024604 (2012).

[60] G. Kaur and M. K. Sharma, Nucl. Phys. A **884**, 36 (2012). G. Kaur and M. K. Sharma, Phys. Rev. C **87**, 044601 (2013).

[61] B. B. Back *et al.*, Phys. Rev C **32**, 195 (1985); Phys. Rev. C **33**, 385 (1986); C. Ngô, Prog. Part. Nucl. Phys. **16**, 139 (986); W. J. Swiatecki, Phys. Ser. **24**, 113 (1981); S. Bjornholm and W. J. Swiatecki, Nucl. Phys. A. **391**, 471 (1982); W. Q. Shen, *et al.*, Phys. Rev. C **36**, 115 (1987); J. Toke, *et al.*, Nucl. Phys. A **440**, 327 (1985); J. P. Blocki *et al.*, Nucl. Phys. A **459**, 145 (1986); P. Armbruster, Annu. Rev. Nucl. Part. Sci. **50**, 411 (2000).

[62] W. U. Schroder and J. R. Huizenga, in Damped Nuclear Reactions, Treatise on Heavy-ion Science, edited by D. A. Bromley (Plenum Press, New York, 1984), Vol. **2**, p. 115.

[63] J. G. Keller, B. B. Back, B. G. Glagola, D. Henderson, S. B. Kaufman, S. J. Sanders, R. H. Siemssen, F. Videbaek, B. D. Wilkins, and A. Worsham, Phys. Rev. C **36**, 1364 (1987).

[64] H. C. Britt and A. R. Quinton, Phys. Rev. **124**, 877 (1961).

[65] T. Sch*ü*ller and T. Schmidt, Z. Phys. **92**, 148 (1934); **94**, 457 (1935).

[66] P. Stransky, A. Frank and R. Bijker, J. Phys. Conf. Ser. **322**, 012018 (2011).

[67] P. Möller and J. R. Nix, Nucl. Phys. A **361**, 117 (1981).

[68] I. Hamamoto and B. R. Mottelson, Phys. Rev. C **79**, 034317 (2009); M. Horoi and V. Zelevinsky, Phys. Rev. C **81**, 034306 (2010).

[69] N. J. Stone, At. Data Nucl. Data Tables **90**, 75 (2005).

[70] R. K. Gupta, M. Balasubramaniam, R. Kumar, N. Singh, M. Manhas, and W. Greiner, J. Phys. G: Nucl. Part. Phys. **31**, 631 (2005).

[71] W. Greiner, International NATO Advanced Study Institute (NASI) Course on Quantum Electrodynamics of Strong Fields, Lahnstein 1981; M. Seiwert, N. Abul-Naga, V. Oberacker, J. A. Maruhn and W. Greiner, Gesellschaft fur Schwerionenforschung (GSI) Annual Report 1981.

[72] J. P. Lestone, Phys. Rev. C **52**, 2 (1995).

[73] W. Myers, and W. J. Swiatecki, Nucl. Phys. **81** 1 (1996).

[74] B. Nerlo-Pomorska, and K. Pomorski, Z. Phys. A **348** 169-172 (1994).

[75] A. Czeszumska *et al.*, Phys. rev. C **87** 034613 (2013).

[76] N. Fotiades *et al.* Phys. Rev. C **91** (2015) 064614.

[77] G. G. Kiss, Gy. Gyürke, Z. Elekes, Zs. Fülöp, and E. Somorjai, Phys. Rev. C **76**, 055807 (2007).

[78] Gy. Gyürke, Zs. Fülöp, and E. Somorjai, Phys. Rev. C **68**, 055803 (2003).

[79] G. G. Kiss, T. Rauscher, Gy Gyürke, A. Simon, Zs. Fülöp, and E. Somorjai, PRL **101**, 191101 (2008).

[80] C. Yalçin et al., Phys. Rev. C **79**, 065801 (2009).

[81] A. Sauwerin *et al.*, Phys. Rev. C **84**, 045808 (2011).

[82] P. Scholz *et al.*, Phys. Rev. C **90**, 065807 (2014).

[83] D. Bourgin *et al.*, Phys. Rev. C **90** (2014) 044610.

[84] Yu. Ts. Oganessian, *et al.*, JINR Communication D7-2002-287 (2002); see http://www.jinr.ru/publish/Preprints/2002/287(D7-2002-287)e.pdf

[85] Yu. Ts. Oganessian, *et al.*, Phys. Rev. C **74**, 044602 (2006).

Chapter 2

Methodology

2.1 Introduction

The work enclosed in this thesis describes the decay analysis of the compound systems formed in a variety of nuclear reactions using a number of projectiles there by resulting in the formation of compound nuclei lying in different mass region-ranging from medium mass to super-heavy region. This work governs the energetics of the nuclear reactions involving beams of neutrons, light charged particles like protons, α-particles and heavy-ions. The incident energy lie in low-energy region (E<15 MeV/nucleon) but sufficient enough to overcome the Coulomb barrier existing between the projectile and target and hence resulting in the relatively long-lived compound systems. The excited state decay paths of the compound nuclei formed in the aforementioned nuclear processes are governed via Dynamical Cluster-decay Model (DCM) [1]- [14] while the ground state processes like- α-decay or cluster emission from super-heavy nuclei is carried out using Preformed Cluster-decay Model (PCM) [15]- [19], both of these are explained in the following sections of this chapter.

This methodology deals with the study of the decay profiles of compound nuclei formed in nuclear reactions within the low energy regime. In general, as suggested by N. Bohr [20] in his theory of compound nuclear reactions, the energetic projectile

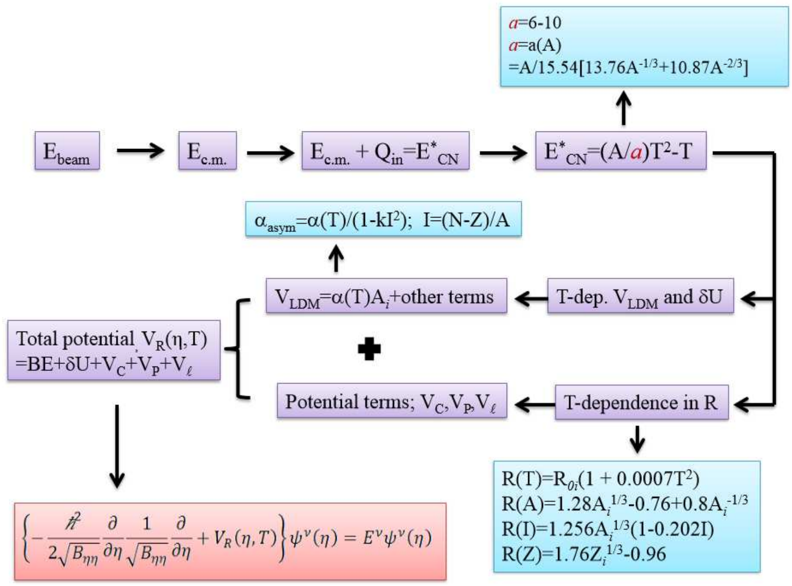

Figure 2.1: The layout of the Dynamical Cluster-decay Model (DCM).

beam when incident upon a target nucleus, gets fused in to it resulting in an intermediate compound nuclear stage, which subsequently de-excites choosing any of the exit channel amongst light particles (LPs), intermediate mass fragments (IMFs) or heavy mass fragments/fission fragments (HMF/ff) as detailed in Chapter-1. It is relevant to note that the energy of the incident beam (E_{beam}) gets equally distribute amongst all degrees of freedom of the nucleons of the amalgamated system (compound nucleus) leaving it in excited state; which disrupts due to Coulombic agitation through the most suitable exit channel. In apprehension to this, the methodology of DCM finds its origin; which involves the flow or exchange of nucleons amongst the interacting nuclei (projectile or target) and the energy of the incoming channel is transferred as $E_{CN}{}^*$. The energy carried by incident beam E_{beam}, in terms of the center of mass frame of the two-body system can be given as;

$$E_{c.m.} = \frac{A_T}{A_T + A_P} E_{beam} \tag{2.1}$$

It can be inferred from this equation that; the conversion of beam energy in to $E_{c.m.}$ depends upon the projectile-target combination. This can be explained as; for projectiles like neutron and proton, with A_P=1;

$$E_{c.m.} \simeq E_{beam} \tag{2.2}$$

while for the use of α-particles as incident beam;

$$E_{c.m.} < E_{beam} \tag{2.3}$$

and for heavier projectiles,

$$E_{c.m.} \ll E_{beam} \tag{2.4}$$

Hence, it may be inferred that a beam of neutrons, protons, α-particles or other heavier ions carrying same beam energy, E_{beam}, when incident up on same target, will leave us with different $E_{c.m.}$ values and hence accordingly, the dynamics of the reactions will be affected. This means, the asymmetry of the incoming channel plays an eminent role in the investigation of the kinematics involved in the nuclear dynamics. The $E_{c.m.}$ is related to $E_{CN}{}^*$ as;

$$E^*_{CN} = E_{c.m.} + Q_{in} \tag{2.5}$$

where Q_{in} defines the Q-value of the incident channel and $Q_{in} = B_P + B_T - B_{CN}$, where the symbols represent the B.E. of incoming, target and compound nucleus respectively. The excitation energy of the compound nucleus E^*_{CN} gives the temperature up to which the equilibrated hot-rotating compound nucleus is excited;

$$E^*_{CN} = \frac{A_{CN}}{a}T^2 - T \tag{2.6}$$

The temperature T of the compound nucleus plays significant role as the inclusion of temperature dependence (T-dependence) in various parameters involved in DCM calculations help in having deeper insights of the role-play of the dynamics of variety of nuclear reactions and associated decay mechanisms. Comprehensively, it may be seen that although the decay mechanism of the compound system forgets the history of its formations, yet the inclusion of temperature or in other words, when the excited state decays of the compound nucleus are taken in to considerations, the influence of the incoming channel needs to be acknowledged. Hence, it may be stated that the investigation of decay dynamics of compound nuclei formed using a variety of projectiles (with different masses) finds its significance from the fact that the asymmetry of the incoming channel somehow, decides the excitations produced in the compound nucleus and consequently, the corresponding fragmentation pattern gets influenced.

In equation (2.6), the term appearing in the denominator a, the nuclear level density parameter (LDP), is a vital ingredient as it arises from the statistical distribution of energy amongst all the nucleons of the compound system. The variation in its magnitude refers to the variation in the number of nuclear levels available for nucleon distribution. This thesis comprises of a set of calculations within which the magnitude of level density parameter a is varied from 6 to 10, keeping the excitation energy E^*_{CN} same and consequently, the compound nucleus is excited to different temperatures for each value of a. This is evident from Table-2.1 where T_{CN} increases with an increase in the magnitude of LDP. As various parameters involved in this methodology are taken to be T-dependent, hence, the corresponding modifications in the fragmentation pattern will be useful in understanding the dynamical and structural effects. Additionally, the LDP can also be made mass dependent instead of taking constant values a=6-10, which means that one can optimize the values of LDP according to the mass of the compound nucleus. For this purpose,

Table 2.1: Values of compound nucleus temperature T_{CN} for different LDP, a= 6 to 10 for compound nucleus $^{77}As^*$ ar $E_{CN}{}^* \simeq 12$ MeV

S. No.	LDP (a)	T (MeV)
1	6	1.007
2	7	1.091
3	8	1.170
4	9	1.245
5	10	1.315

mass-dependence is also included in the LDP which reads as [21];

$$a = \frac{A}{15.54}[1 + 3.76 \times A^{-1/3} + 10.87 \times A^{-2/3}] \tag{2.7}$$

Using this one can get a set of LDP values for compound nuclei lying in various mass regions and this, in turn, may administer a better picture for the statistical distribution as compared to the use of fixed value of LDP a=9.

The optimization of T_{CN} from compound nuclear excitation energies, using the statistical equation(eq.(2.6)), further assists to include T-dependence in other parameters of DCM as defined in following sub-sections.

Macroscopic part-Liquid drop energies and the T-dependent parameters: Defining the set of binding energies to be used in calculations in any nuclear related problems is the most fundamental step. In literature, a number of sets of binding energies [22–24] with different set of constants are available , but every version finds their origin from the liquid drop analogy of a nucleus. These versions are similar from the view point of taking volume term, surface term and Coulomb term as the fundamentally contributing terms and differ in the inclusion of correction terms like asymmetry term, Wigner term and pairing term. In the present work, the binding energies used are the Liquid drop binding energies based on the semi-empirical mass formula used by Seeger [22] and is given as;

$$V_{LDM}(A_i, Z_i, T) = \alpha(T)A_i + \beta(T)A_i^{2/3} + (\gamma(T) - \frac{\eta(T)}{A_i^{1/3}}) \times (\frac{t^2 + 2 \mid t \mid}{A_i}) + \frac{Z_i^2}{r_0(T)A_i^{1/3}}$$

$$\times(1 - \frac{0.7636}{Z_i^{2/3}} - \frac{2.29}{[r_0(T)A_i^{1/3}]^2}) + \delta(T)\frac{f(Z_i, A_i)}{A_i^{3/4}} \quad (2.8)$$

with $t = a_a(Z_i - N_i)$, $a_a = 1$, and f(Z_i, A_i)=-1 for even-even,0 for even-odd and 1 for odd-odd nuclei. The values of constants at $T = 0$ was estimated by Seeger [22] and are given in the reported reference. The pairing energy term is taken from Ref. [25]. These constants of V_{LDM} at $T = 0$ are re-fitted in [1–3] with respect to the experimental binding energies where shell corrections are determined from Myers and Swiatecki [26]. The first attempt was made by [1, 2] for Audi Wapstra Tables [27] of binding energies, and then in [3] for the Tables [28].

The T-dependence of V_{LDM}(T) used in defining the fragmentation potential is taken from Davidson *et. al.* [29] which provide different set of constants β, γ , η and δ for every value of T. Also, in this work, α(T) used in the first term of the LDM eq.(2.8) (which represents the volume term) is made asymmetry dependent (α_{asym}) in accordance with [26] and modified as;

$$\alpha_{asym} = \alpha(T)/[1 - kI^2] \quad (2.9)$$

with I=(N-Z)/A, and the value of k is also taken from [26]. The new set of α_{asym} which comes out to be neutron-proton asymmetry dependent (I-dependent), are obtained by rescaling the conventional set of Bulk constant (α) used in DCM, by a factor of (1-kI^2). Evidently, the effect of inclusion of I-dependence vanishes for N=Z. The refitting is done at T=0 MeV and subsequently, the temperature dependence is included as per [29]. It is relevant to mention here that similar efforts have been done previously [3] where α were refitted only but no neutron-proton asymmetry dependence was included.

The binding energy of xn-cluster, is defined as (from [30, 31])

$$B(A_2 = xn) = xB_n, \tag{2.10}$$

and the binding energies of $xnyp$-cluster with x neutrons and y protons are calculated as

$$B(A_2 = xnyp) = xB_n + yB_p - a_c A_L^{5/3} \tag{2.11}$$

where B_n is the binding energy of one neutron and B_p is the binding energy of one proton and these values are taken to be Temperature-dependent. The additional term $a_c A_L^{5/3}$ is due to the repulsive Coulomb forces [26] between the protons and value of a_c=0.7053 MeV. Consequently, with in this work, the binding energy of multinucleon system $2p2n$ at T=0 MeV is estimated as 23.618 MeV while for α-cluster its value at T-0 MeV is 2.4966 MeV and later on the T-dependence is included in ref. to [29]. It is relevant to mention here that both the systems have A_L=4 yet differ on the basis of binding energies.

The shell corrections are included in accordance to the “empirical” formula of Myers and Swiatecki [26].

Moving further, the most vital factor involved in analysis of interaction between two nuclei is the radius of the two nuclei. The significance of radius term emerges from the fact that every potential term will depend up on the relative separation between the interacting nuclei and hence, the potential terms will be affected accordingly in magnitude. Hence, the preference of radius term plays an eminent role in estimating the magnitudes of various potential terms involved and consequently, the other dynamical aspects of nuclear reactions under consideration will be affected. The fragmentation potential, which is defined as the resultant of binding energies of the interacting nuclei with shell corrections duly included, the long range Coulomb potential (V_C), the centrifugal potential due to rotation of the hot excited decaying fragments (V_ℓ) and the proximity potential (V_P) coming in to picture as the two interacting nuclei lie in immediate vicinity of each other, is the essence of DCM based calculations and require appropriately defined radius expression. The literature of nuclear physics defined the radius term of a spherical nucleus in terms of its mass number as;

$$R = R_0 A^{1/3} \tag{2.12}$$

with R_0=1.2 fm. Along the line, this expression has been modified and various other empirical factors has been included in it. Also, its dependence on factors other than mass number A had also been proposed in passed years and it had presented a newer pathways for enhancing the understanding of nuclear reaction mechanisms. In DCM, the radius term used in determining the magnitude of various potential terms for hot-deformed decaying fragments is defined as;

$$R_i(\alpha_i, T) = R_{0i}(T)[1 + \sum_{\lambda} \beta_{\lambda i} Y_{\lambda}^{(0)}(\alpha_i)] \tag{2.13}$$

and

$$R_{0i}(A, T) = [1.28A_i^{1/3} - 0.76 + 0.8A_i^{-1/3}](1 + 0.0007T^2) \tag{2.14}$$

Here, i= 1,2 is chosen respectively for both the decaying and interacting fragments or nuclei and the second term in eq.(2.13) incorporates the deformation effects. Clearly, eq.(2.14) represents the radius expression utilized in DCM based calculations and evidently, it is taken to be mass dependent. The temperature dependence is also included and is depicted in eq.(2.14). The literature available for demonstrating nuclear reactions characterizes other parameters also on which the radius term is thought to be dependent upon asymmetry ($I = \frac{N-Z}{A}$) of the interacting nuclei. The inclusion of this dependencies can be read as under;

$$R_{0i}(I) = 1.256 A_i^{1/3}(1 - 0.202I) \tag{2.15}$$

in ref. to [32]. The use of above-mentioned radius expressions, reformulate the magnitude of the fragmentation potential and the structural distribution gets influenced accordingly. The dependence of radius term on Z and I attunes the potential terms describing these interactions and hence, the corresponding potential barriers and other characteristics also get modified. The observations following the use of various radius expressions and the results are discussed in subsequent chapters. The various potential terms exemplifying the interactions of these two-body problems i.e. the interaction of the two decaying fragments, are defined in succeeding sub-sections.

The Proximity Potential for deformed, oriented, co-planar nuclei:

There are some additional attractive forces which come in to picture when the two nuclei lie in close proximity to each other are called Proximity forces which are explained by Blocki *et al.* [33] via reformulating a theory originated by Deryagin [34]. The original expression of Blocki based on the pocket formula was for spherical nuclei, and is given by

$$\begin{aligned} V_P(s_0) &= f(sh., geo.)\Phi(s_0) \\ &= 4\pi\bar{R}\gamma b\Phi(s_0). \end{aligned} \tag{2.16}$$

The constants used here are defined in [33]. In this work, two versions of proximity potential are used namely- Prox77 and Prox00 in which the above mentioned parameters have different definitions which are explained as follows. Within the Prox77 potential, the universal function $\Phi(s_0)$ takes the form;

$$\Phi(s_0) = \begin{cases} -\frac{1}{2}(s_0 - 2.54)^2 - 0.0852(s_0 - 2.54)^3 \\ -3.437exp(-\frac{s_0}{0.75}) \end{cases} \tag{2.17}$$

respectively, for $s_0 \leq 1.2511$ and $s_0 \geq 1.2511$. Here, s_0 is defined in units of b, i.e. s_0 is s_0/b, where b is the diffuseness.

While for the Prox00 potential, its value reads as:

$$\Phi(s_o) = \begin{cases} -0.1353 + \sum_{n=0}^{5}[c_n/(n+1)](2.5 - s_o)^{n+1} \\ \qquad for 0 < s_o \leq 2.5, \\ -exp((2.75 - s_o)/0.7176) \\ \qquad for s_o \geq 2.5, \end{cases} \tag{2.18}$$

The values of different constants c_n were c_0=-0.1886, c_1=-0.2628, c_2=-0.15216, c_3=-0.04562, c_4=0.069136, and c_5=-0.011454. The values of other constants and detailed description of these potential terms is in reference to [35], [36, 37] .

The Coulomb potential: The positive Coulomb potential acting between two nuclei is given as:

$$V_c = \frac{Z_1 Z_2 e^2}{R} \tag{2.19}$$

While for deformed and oriented interacting nuclei in DCM, the Coulomb potential reads as [38], [39, 40]:

$$V_c(Z_i, \beta_{\lambda i}, \theta_i, T) = \frac{Z_1 Z_2 e^2}{R(T)} + 3Z_1 Z_2 e^2 \sum_{\lambda, i=1,2} \frac{R_i^{\lambda}(\alpha_i, T)}{(2\lambda+1)R(T)^{\lambda+1}} Y_{\lambda}^{(0)}(\theta_i) \Big[\beta_{\lambda i} + \frac{4}{7}\beta_{\lambda i}^2 Y_{\lambda}^{(0)}(\theta_i)\Big], \tag{2.20}$$

where the symbols have their usual meanings.

Centrifugal potential of hot rotating compound nucleus: The kinetic energy of the entrance channel is transferred to the internal excitation there by forming a hot rotating compound system. This rotational motion of the hot compound nu-

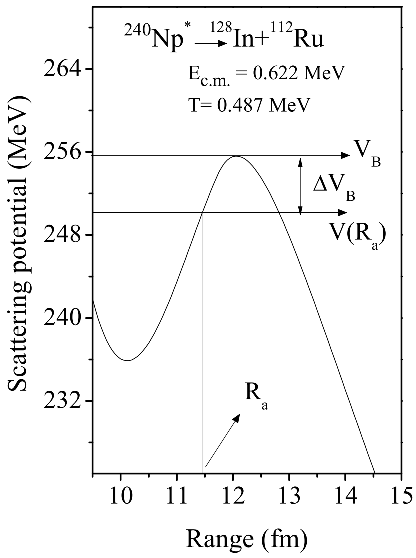

Figure 2.2: Scattering potentials $V(R)$ for ^{240}Np*→^{128}In+^{112}Ru using the DCM, at a fixed temperature T=0.487 MeV, corresponding to $E_{c.m.}$=0.62 MeV, calculated at $\ell = \ell_{max}$. The concept of barrier lowering $\Delta V_B = V(R_a) - V_B$ is also shown.

cleus provides centrifugal energy due to angular momentum gained by the system. This centrifugal potential ℓ is given by;

$$V_\ell(R, A_i, \beta_{\lambda i}, \theta_i, T) = \frac{\hbar^2 \ell(\ell+1)}{2I(T)} \tag{2.21}$$

where μ is the reduced mass and I is the moment of inertia. The two limits used here are- sticking I_S and non-sticking I_{NS}. The sticking moment of inertia I_S is given as;

$$I_S(T) = \mu R^2 + \frac{2}{5} A_1 m R_1^2(\alpha_1, T) + \frac{2}{5} A_2 m R_2^2(\alpha_2, T). \tag{2.22}$$

and the non-sticking moment of inertia I_{NS}=μR^2 [41].

2.2 Scattering potential and barrier characteristics

The various potential terms, as explained above, help in explaining how the two decaying fragments interact and how the interaction between a particular pair of fragments dominates the decay channel at the expense of other fragments. Also, these potential terms, collectively, define the *scattering potential*, which reads as;

$$\begin{aligned} V(R,\ell,T) &= V_C(R,Z_i,\beta_{\lambda i},\theta_i,\phi,T)+V_P(R,A_i,\beta_{\lambda i},\theta_i,\phi,T) \\ &+ V_\ell(R,A_i,\beta_{\lambda i},\theta_i,\phi,T) \end{aligned} \quad (2.23)$$

This potential demonstrates the decay path of the fragments, being emitted from a decaying compound system. A typical scattering potential for the decay $^{240}Np^{*} \rightarrow ^{128}In + ^{112}Ru$ at a fixed temperature T=0.487 MeV, corresponding to $E_{c.m.}$=0.62 MeV, calculated at $\ell = \ell_{max}$ is shown in Fig.2.2. Clearly, the shape of the plot is an interweaving of the behavior of Proximity and Coulomb potential, where, for short range, the proximity potential defines the shape of the curve and at longer range, the behavior of the plot follows Coulomb potential.

The point from which tunnelling of the potential barrier starts, is defined as;

$$R_a(T) = R_t + \Delta R(\eta, T) \quad (2.24)$$

where

$$R_t = R_1(\alpha_1, T) + R_2(\alpha_1, T) \quad (2.25)$$

$\Delta R(T)$ is the neck-length parameter which assimilates the neck formation effects and R_i are radius vectors, given by eqs.(2.14-2.15).

The potential $V(R_a)$ at R=R$_a$ gives the effective Q-value, Q_{eff}, for the decay of the hot CN at temperature T. Also, the second turning point R_b satisfies the following condition

$$V(R_a, \ell) = V(R_b, \ell) = Q_{eff}(T, \ell) = TKE(T). \tag{2.26}$$

Defining the lowering of the barrier: At energies around the Coulomb barrier, the compound nucleus fusion probability is hindered due to the various factors including low binding energy of the projectile, halo nuclei or due to competing direct or non-compound nucleus processes which lead to the over-estimation of data through coupled-channel calculations. In this case, the addressal of data requires adequate modification of the barrier profile and this methodology provides this barrier modification by defining a parameter called *Barrier lowering* (ΔV_B).

This phenomenon of barrier lowering while keeping the depth of the fusion pocket intact emerges through the optimization of neck-length parameter ΔR. The parameter R_a corresponding to the best-fit of the available experimental data defines the effective barrier $V(R_a)$ experienced by the decaying fragments. For each ℓ-value, barrier lowering is defined as;

$$\Delta V_B(\ell) = V(R_a, \ell) - V_B(\ell). \tag{2.27}$$

where $V_B(\ell)$ is the barrier height and $V(R_a,\ell)$ is the potential at $R=R_a$.

2.3 Quantum Mechanical Fragmentation Theory

The Dynamical Cluster-decay Model (DCM) approach is developed in view of Quantum Mechanical Fragmentation Theory (QMFT) [42]- [49], which works in terms of mass (and charge), η_A (and η_Z) asymmetry coordinate of the two decaying fragments and relative separation coordinate R between the two separating fragments.

The mass asymmetry is defined as;

$$\eta_A = \frac{A_1 - A_2}{A_1 + A_2} \tag{2.28}$$

and consequently, the charge asymmetry coordinate may be represented as;

$$\eta_Z = \frac{Z_1 - Z_2}{Z_1 + Z_2} \tag{2.29}$$

where 1 and 2 represent, the heavier and the lighter fragment respectively. The deformation co-ordinates $\beta_{\lambda i}$ (λ=2,3,4... and i=1,2) of the decaying fragments, their orientation degrees of freedom $\theta_i (i = 1, 2)$ are included appropriately while the angle between the principle planes, azimuthal angle ϕ is taken to be zero. However, in the present work, the deformations are considered only up to quadrupole (β_2, with λ=2) deformations and ϕ is taken to be zero as we are dealing with co-planar interactions.

The Schrödinger wave equation in terms of mass parameters η and relative separation R co-ordinates can be written as:

$$H(\eta, R)\psi(\eta, R) = E(\eta, R)\psi(\eta, R) \tag{2.30}$$

with the Hamiltonian,

$$H(\eta, R) = K(\eta) + K(R) + K(\eta, R) + V(\eta) + V(R) + V(\eta, R) \tag{2.31}$$

For decoupled Hamiltonian, Schrödinger wave equation (eq.(2.31)) can be separated for the two co-ordinates η and R as follows,

$$\left[-\frac{\hbar^2}{2\sqrt{B_{\eta\eta}}} \frac{\partial}{\partial \eta} \frac{1}{\sqrt{B_{\eta\eta}}} \frac{\partial}{\partial \eta} + V(\eta) \right] \psi^{\nu}(\eta) = E^{\nu}_{\eta} \psi^{\nu}(\eta) \tag{2.32}$$

and

$$\left[-\frac{\hbar^2}{2\sqrt{B_{RR}}}\frac{\partial}{\partial R}\frac{1}{\sqrt{B_{RR}}}\frac{\partial}{\partial R}+V(R)\right]\psi^{\nu}(R)=E_R^{\nu}\psi^{\nu}(R) \tag{2.33}$$

with

$$\psi(\eta,R)=\psi(\eta)\psi(R) \tag{2.34}$$

and

$$E=E_\eta+E_R \tag{2.35}$$

The states $\psi^{\nu}(\eta)$ are the vibrational states in the potential $V(\eta)$ and are labelled by the quantum numbers $\nu = 0, 1, 2, ...$

Fragmentation potential: The temperature dependent potential energy or the fragmentation potential V(η, R, T) which is used to solve the Schrödinger equation (eq.(2.31)) is defined as;

$$\begin{aligned} V_R(\eta,T) &= \sum_{i=1}^{2}[V_{LDM}(A_i,Z_i,T)]+\sum_{i=1}^{2}[\delta U_i]\exp(-T^2/T_0^2)+V_C(R,Z_i,\beta_{\lambda i},\theta_i,T) \\ &\quad +V_P(R,A_i,\beta_{\lambda i},\theta_i,T)+V_\ell(R,A_i,\beta_{\lambda i},\theta_i,T) \end{aligned} \tag{2.36}$$

The ingredients of the fragmentation potential $V_R(\eta, T)$ have already been discussed in the preceding sub-sections of this chapter.

Preformation probability P_0:

After the establishment of the Hamiltonian of eq.(2.32), the Schrödinger equation is solved in mass fragmentation co-ordinate (η $|\psi^{\nu}(\eta)|^2$) to define the probability with which the decaying fragments are pre-born within the compound nucleus prior to the decay, called the preformation probability P_0 such that;

$$P_0(A_2)\propto|\psi^{\nu}(A_2)|^2 \tag{2.37}$$

where ν=0 refer to nuclear ground state solutions while ν=1, 2, 3,... refer to excited state decays. For the nuclear ground state processes like spontaneous fission (SF) or cluster decay only ν=0 is occupied and in this case the mass (or charge) distribution yield for a fragment of certain mass will be proportional to the probability $|\psi^{(0)}(\eta)|^2$ (or $|\psi^{(0)}(\eta_Z)|^2$). This probability of finding a particular decay channel having a fixed mass asymmetry η_A (or charge η_Z asymmetry) at a particular position R, after normalization is defined as;

$$P_0 = |\psi_R^{(0)}(A_2)|^2 \frac{2}{A}\sqrt{B_{\eta\eta}(A_2)}). \tag{2.38}$$

However for excited system where the interaction between various degrees of freedom are allowed, there will be excitation of higher vibrational states hence, the higher values of ν would also contribute. This is achieved via inclusion of temperature dependence in potential V and masses B_{ij}. On the other hand, cold fission means taking both the potential V and masses B_{ij} having full shell effects included in them while hot fission refers to the V_{LDM} and smoothed masses B_{ij}. Such excitations are included here by assuming a Boltzmann like occupation of excited states

$$|\psi(\eta)|^2 = \sum_{\nu=0}^{\infty} |\psi^{\nu}(\eta)|^2 \exp\left(-\frac{E_\eta^\nu}{T}\right) \tag{2.39}$$

Barrier Penetration Probability P**:** After the fragments or clusters are preborn within the compound nucleus, the next step is to penetrate through the barrier to complete the binary fragmentation of the decaying compound nucleus. The probability of the decaying fragments to penetrate or tunnel through the barrier is calculated from WKB approximation. The scattering potential V(R) is defined as;

$$V(R) = V_c + V_p + V_\ell \tag{2.40}$$

For ground state processes, the transmission probability P is defined as:

$$P = P_i W_i P_b. \tag{2.41}$$

However, for a heavy cluster decay into the excited states of the daughter nucleus $\mathbf{W}_i\mathbf{=1}$, such that,

$$P = P_i P_b, \tag{2.42}$$

where P_i and P_b are calculated by using WKB approximation giving the final expression as:

$$P = exp[-\frac{2}{\hbar}\int_{R_a}^{R_b}\{2\mu[V(R) - Q_{eff}]\}^{1/2}dR], \tag{2.43}$$

where R_a and R_b represent the entry and exit points of barrier penetration, μ is the reduced mass and Q_{eff} is the effective Q-value.

2.4 Reaction cross-sections using Dynamical Cluster-decay Model:

The decoupled approximation when applied to R and η-motions, defines the DCM based decay cross-sections in terms of partial wave analysis as [1]- [14];

$$\sigma = \sum_{\ell=0}^{\ell_{max}} \sigma_\ell = \frac{\pi}{k^2}\sum_{\ell=0}^{\ell_{max}}(2\ell+1)P_0 P; \qquad k = \sqrt{\frac{2\mu E_{c.m.}}{\hbar^2}} \tag{2.44}$$

where, μ is the reduced mass of the two-body problem. P_0 is the preformation probability and refers to η-motion whereas P is the barrier penetrability and corresponds to R-motion. The ℓ_{max} is the maximum angular momentum which correspond to the ℓ-value at a stage where light particle cross-sections become negligibly small. These terms are explained in the former sub-sections of this chapter.

2.5 Ground state decays: Preformed Cluster-decay Model

The ground state decay processes like α-decay, cluster decay have always been a matter of interest and number of theoretical models [15, 50–54] were put forward to have proper understanding of the dynamics involved in such reactions. Broadly speaking, such models are classified into two categories-first, Unified Fission Model (UFM) which explains cluster decay as single step barrier penetration. Second, Preformed Cluster-decay Model (PCM) [15]- [19], which defines the cluster-decay as a two step process. In the present work, the ground state processes like- α-decay, cluster decay are worked out within the guidelines of Preformed Cluster-decay Model (PCM).

The methodology of PCM is different from the other models in the sense that it estimates the preformation probability of all the possible fragments/clusters while the other models or theories like that of Gamow theory for α-decay, only α-particle is considered to be emitted and hence its preformation probability is taken to be 1. In PCM, the decay constant is defined as;

$$\lambda = \nu_0 P P_0 \tag{2.45}$$

and the half-life of the decay is;

$$T_{1/2} = \frac{\ln 2}{\lambda} \tag{2.46}$$

In the above equation, P_0 is the probability of preformation of the clusters within the parent nucleus before emission and ν_0 is the frequency with which the preformed clusters hit the barrier. P refers to the probability of tunnelling or penetration through the barrier.

Also, for ℓ=0 i.e. for s-wave; the eq.(2.45) reduces to $\sigma_0 = \frac{\pi}{k^2} P_0 P$, which when compared with the corresponding expression of decay constant (λ) as given by PCM i.e. $\lambda = \nu_0 P_0 P$, suggests that σ_0 and λ differ through a constant only.

However, in this work, PCM (T≠0) has also been employed to analyze the α-decay chains of $^{294}118^*$ nucleus, where T is related to the recoil energy E_R of the (recoiled) residue SHN [55] whose excitation energy E_R^* for α-decay is

$$E_R^* = E_R + Q_\alpha, \tag{2.47}$$

where E_R^*, when given in terms of T(in MeV) just like E_{CN}^* , reads as

$$E_R^* = \frac{1}{a} A T^2 - T \tag{2.48}$$

Here, the value of level density parameter $a = 11$, as mass of the parent nucleus is quite high (in super-heavy region). Also, for the recoil energy E_R, we have taken value of 12.5 MeV which is chosen in reference to the average of the measured E_R range [56] (7-18 MeV) for α-decay chain of $^{294}118^*$ nucleus. The results obtained using collective clussterization based methodology are discussed in subsequent chapters.

Bibliography

[1] R. K. Gupta, R. Kumar, N. K. Dhiman, M. Balasubraniam, W. Scheid, and C. Beck, Phys. Rev. C **68**, 014610 (2003).

[2] M. Balasubraniam, R. Kumar, R. K. Gupta, C. Beck, and W. Scheid, J. Phys. G **29**, 2703 (2003).

[3] B. B. Singh, M. K. Sharma, and R. K. Gupta, Phys. Rev. C **77**, 054613 (2008).

[4] R. K. Gupta, M. Balasubraniam, R. Kumar, D. Singh, and C. Beck, Nucl. Phys. A **738**, 479c (2004). R. K. Gupta, M. Balasubramaniam, R. Kumar, D. Singh, C. Beck, and W. Greiner, Phys. Rev. C **71**, 014601 (2005).

[5] B. B. Singh, M. K. Sharma, R. K. Gupta, and W. Greiner, Int. J. Mod. Phys. E **15**, 699 (2006).

[6] S. Kanwar, M. K. Sharma, B. B. Singh, R. K. Gupta, and W. Greiner, Int. J. Mod. Phys. E **18**, 1453 (2009). S. K. Arun, R. Kumar, and R. K. Gupta, J. Phys. G: Nucl. Part. Phys. **36**, 085105 (2009).

[7] M. K. Sharma, S. Kanwar, G. Sawhney, R. K. Gupta, and W. Greiner, J. Phys. G: Nucl. Part. Phys. **38**, 055104 (2011); D. Jain, R. Kumar, M. K. Sharma, and R. K. Gupta, Phys. Rev. C **85**, 024615 (2012).

[8] M. K. Sharma, G. Sawhney, R. K. Gupta, and W. Greiner, J. Phys. G: Nucl. Part. Phys. **38**, 105101 (2011). M. K. Sharma, G. Sawhney, S. Kanwar, and R. K. Gupta, Mod. Phys. Lett. A **25**, 2022 (2010).

[9] G. Sawhney and M. K. Sharma, Eur. Phys. J. A **48**, 57 (2012). M. K. Sharma, S. Kanwar, G. Sawhney, and R. K. Gupta, Phys. Rev. C **85**, 064602 (2012).

[10] M. Kaur, R. Kumar, and M. K. Sharma, Phys. Rev. C **85**, 014609 (2012).

[11] M. Kaur and M. K. Sharma, Phys. Rev. C **85**, 054605 (2012). M. Kaur, M. K. Sharma and Raj K. Gupta, Phys. Rev. C **86**, 064610 (2012).

[12] M. Kaur and Manoj K. Sharma, *International Conference On Recent Trends in Nuclear Physics-2012*, published in AIP conf. proc. **1524**, pp.151-154 (2013).

[13] K. Sandhu, M. K. Sharma, and R. K. Gupta, Phys. Rev. C **85**, 024604 (2012).

[14] G. Kaur and M. K. Sharma, Nucl. Phys. A **884**, 36 (2012). G. Kaur and M. K. Sharma, Phys. Rev. C **87**, 044601 (2013).

[15] S. S. Malik and R. K. Gupta, Phys. Rev. C **39**, 1992 (1989).

[16] S. K. Arun, R. K. Gupta, B. B. Singh, S. Kanwar, and M. K. Sharma, Phys. Rev. C **79**, 064616 (2009).

[17] S. K. Arun, R. K. Gupta, S. Kanwar, B. B. Singh, and M. K. Sharma, Phys. Rev. C **80**, 034317 (2009).

[18] G. Sawhney, M. K. Sharma, and R. K. Gupta, Phys. Rev. C **83**, 064610 (2011).

[19] R. Kumar and M. K. Sharma, Phys. Rev. C **85**, 054612 (2012).

[20] N. Bohr, Nature (London) **137**, 344 (1936).

[21] J. P. Lestone, Phys. Rev. C **52**, 2 (1995).

[22] P. A. Seeger, Nucl. Phys. **25**, 1 (1961).

[23] C. Guet, Phys. Lett. B **205**, 4 (1988).

[24] H. J. Krappe, Phys. rev. C **59**, 5 (1999).

[25] S. DeBenedetti, Nuclear Interactions (New York: Wiley) (1964).

[26] W. Myers, and W. J. Swiatecki, Nucl. Phys. **81** 1 (1966).

[27] G. Audi and A. H. Wapstra, Nucl. Phys. A **595**, 4 (1995).

[28] G. Audi, A. H. Wapstra and C. Thiboult, Nucl. Phys. A **729**, 337 (2003).

[29] N. J. Davidson, S. S. Hsiao, J. Markram, H. G. Miller, and Y. Tzeng, Nucl. Phys. A **570**, 61c (1994).

[30] R. K. Gupta, S. Kumar, M. Balasubramaniam, G. Münzenberg, and W. Greiner, J. Phys. G : Nucl. Part. Phys. **28**, 699 (2002).

[31] R. K. Gupta, M. Balasubramaniam, S. Kumar, S. K Patra, G. Münzenberg, and W. Greiner, J. Phys. G : Nucl. Part. Phys. **32**, 565 (2006).

[32] B. Nerlo-Pomorska, and K. Pomorski, Z. Phys. A **348** 169-172 (1994).

[33] J. Blocki, J. Randrup, W. J. Swiatecki, and C. F. Tsang, Ann. Phys. (NY) **105**, 427 (1977).

[34] Deryagin, Kolloid Z. **69**, 155 (1934).

[35] D. jain, R. Kumar and M. K. Sharma, Nucl. Phys. A **915** 106-124 (2013).

[36] W. D. Myers, W. J. Światecki, Phys. Rev. C **62**, 044610 (2000).

[37] K. A. Brueckner, J. R. Buchler, M. Kelly, Phys. Rev. **173**, 944 (1968).

[38] R. K. Gupta, M. Balasubramaniam, R. Kumar, N. Singh, M. Manhas and W. Greiner, J. Phys. G: Nucl. Part. Phys. C **31**, 631 (2005).

[39] M. Münchow, D. Hahn and W. Scheid, Nucl. Phys. A **388**, 381 (1982).

[40] M. J. Rhoades-Brown, V. E. Oberacker, M. Seiwert and W. Greiner, Z. Phys. A **310**, 287 (1983).

[41] S. Kailas (private communication).

[42] J. Maruhn and W. Greiner, Phys. Rev. Lett. **32**, 548 (1974).

[43] R. K. Gupta, W. Scheid, and W. Greiner, Phys. Rev. Lett. **35**, 353 (1975).

[44] A. Săndulescu, R. K. Gupta, W. Scheid, and W. Greiner, Phys. Lett. B **60**, 225 (1976). R. K. Gupta, A. Săndulescu, and W. Greiner, Phys. Lett. B **67**, 257 (1977); Rev. Roum. Phys. **23**, 51 (1978).

[45] S. Yamaji, W. Scheid, H. J. Fink, and W. Greiner, Z. Phys. A **278**, 69 (1976).S. Yamaji, W. Scheid, H. J. Fink, and W. Greiner, J. Phys. G: Nucl. Phys. **2**, L189 (1976). S. Yamaji, K. H. Ziegenhain, H. J. Fink, W. Greiner, and W. Scheid, J. Phys. G: Nucl. Phys. **3**, 1283 (1977).

[46] R. K. Gupta, A. Săndulescu, and W. Greiner, Z. Naturforsch. **32a**, 704 (1977).R. K. Gupta, C. Pirvulescu, A. Săndulescu, and W. Greiner, Z. Phys. A **283**, 217 (1977); Sovt. J. Nucl. Phys. **28**, 160 (1978). R. K. Gupta, Z. Physik. A **281**, 159 (1977).

[47] A. Săndulescu, H. J. Lustig, J. Hahn, and W. Greiner, J. Phys. G: Nucl. Phys. **4**, L279 (1978).H. J. Lustig, J. A. Maruhn, and W. Greiner, J. Phys. G: Nucl. Phys. **6**, L25 (1980).

[48] H. J. Fink, W. Greiner, R. K. Gupta, S. Liran, J.H. Maruhn, W. Scheid, and O. Zohni, in Proceedings of Int. Conf. on Reaction between Complex Nuclei, Nashville, 1974, 21, (Amsterdam: North Holland), pages 2.

[49] R. K. Gupta, IANCAS Bull. (India), **6**, 2 (1990).

[50] Y. J. Shi and Swiatecki, Phys. Rev. C **54**, 300 (1985).

[51] G. A. Pik-Pichak, Yad. Fiz. **44**, 1421 (1986).

[52] R. Blendowske and H. Walliser, Phys. Rev. Lett. **61**, 1930 (1988).

[53] B. Buck and A. C. Merchant, J. Phys. G: Nucl. Phys. **15**, 615 (1989).

[54] A. Sandulescu, R. K. Gupta, F. Carstoiu, M. Horoi, and W. Greiner, Int. J. Mod. Phys. E **1**, 374 (1992).

[55] Niyti, G. Sawhney, M. K. Sharma, and R. K. Gupta, Phys. Rev. C **91**, 054606 (2015).

[56] Yu. Ts. Oganessian, *et al.*, Phys. Rev. Lett. **109**, 162501 (2012).

Chapter 3

Fission decay analysis of ^{240}Np* formed in n-induced reaction

3.1 Introduction

Nuclear reactions have always proved to be the key-tool in understanding the nuclear structure, properties of nuclear matter and provide vital information regarding the role of various parameters that are contemplated while probing the dynamics of such reactions [1–3]. With the advent of technology, numerous stable and radioactive beams are available for investigating through the reaction mechanisms-neutrons beams being elemental amongst them. It is a well known fact that when a neutron is incident upon a target nucleus, whole of the beam energy is imparted to the compound nucleus thus formed as the Coulomb barrier vanishes for neutrons. Due to this, the neutrons have always been designated as one of the best probing tool as far as nuclear reactions at low energies (E<15 MeV/ nucleon) are considered. Since the neutrons have A=1, hence the compound nucleus formed will have mass almost equal to the target nucleus. If heavy mass target nucleus ^{239}Np is used then A_{CN}=240 and when light mass nucleus ^{60}Ni [4] is used then A_{CN}=61. Consequently, the compound nuclei will chose to decay via fission or particle evaporation depending upon their masses. In view of this, the present work comprises of investigation of both kind of decays-fission and particle evaporation. The fission decay analysis in n-induced reactions is presented in this chapter while the particle evaporation for the same is explained in detail in next chapter.

Hence, this chapter proceeds via analysis of the decay pattern of ^{240}Np* nucleus formed in n+^{239}Np over incident beam energy of E$_n$=0.62-18.75 MeV [5]. The fission cross-sections are addressed for ^{240}Np* within the framework of DCM [6–12], which is reformulation of PCM [13–15], by varying the neck-length parameter ΔR, in reference to the experimental data [5]. The detailed description of the analysis carried out is explained in the Sec.-3.2 and the conclusions are drawn in Sec.-3.3

3.2 Calculations and Results

This section involves the decay analysis of ^{240}Np* nucleus formed in n+^{239}Np reaction over an energy range of E$_n$=0.62-18.75 MeV (or equivalently E$_{c.m.}$=0.62-18.67 MeV). The fission decay cross-sections of this nucleus are addressed via DCM and the results are compared with experimental data [5]. To investigate the role of quadrupole (β_2) deformations, the decay of ^{240}Np* nucleus is studied for spherical as well as quadrupole (β_{2i}) deformed choice of fragmentation and the deformation parameters of the nuclei ($\beta_{\lambda i}$) are taken from the tables of [16]. Interestingly, the experimentally measured fission cross-sections are found to possess a triple humped variation and corresponding maxima is seen at energies $E_{c.m.}$=1.87, 8.75 and 16.92 MeV (see later in Fig. 3.6). These enhanced cross-sections may be due to the orientation degree of freedom of decaying fragments and the same is investigated by taking into account the hot (equatorial) and cold (polar) configurations [17]. Apart from this, another feature investigated in the present study is the influence of moment of inertia and to investigate this, the comparative study of the decay profile is done by using sticking limit (I_S) as well as non-sticking limit of moment of inertia (I_{NS}) (defined in Chapter-2) [18]. Lastly, the comparative analysis of decay profile

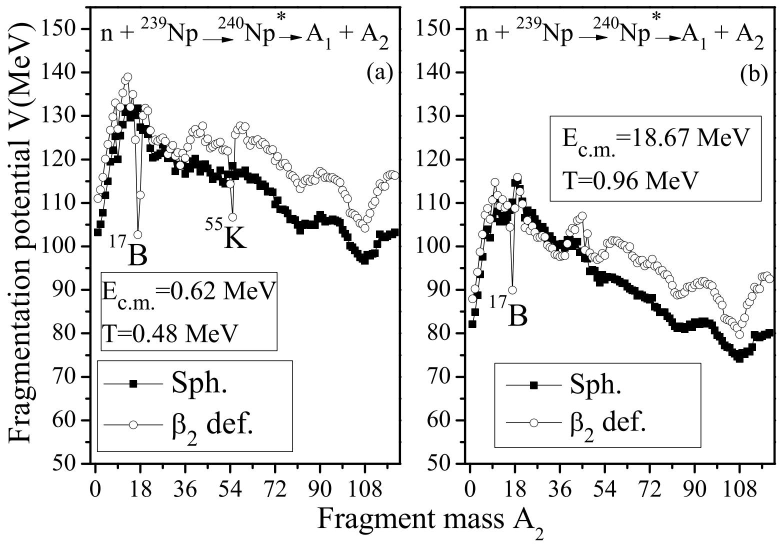

Figure 3.1: Comparative study of fragmentation potential minimized in mass coordinate η(A) for the decay of ^{240}Np* nucleus plotted at center of mass energy (a)E$_{c.m.}$=0.62 MeV and (b)E$_{c.m.}$=18.67 MeV at ℓ=ℓ_{max}. The filled square represents spherical choice of fragmentation while the hollow circles represent the deformed approach.

of ^{240}Np* is done with that of ^{238}U* formed in similar reaction conditions [19] on the basis of their same N/Z value.

Hence, the following sub-sections deal with: (i) the study of the effect of spherical and quadrupole deformed fragmentation (ii) the analysis of the influence of hot (equatorial) and cold (polar) orientation degree of freedom to account for the enhanced fission cross-sections at few energies and (iii) to carry out the comparative study of sticking limit (I_S) and non-sticking limit of moment of inertia (I_{NS}) (iv) comparative analysis of the decay profiles of ^{240}Np* and ^{238}U*.

3.2.1 Role of deformations in the decay of ^{240}Np*

Fig.3.1 shows the behavior of fragmentation potential as a function of fragments mass A_2, plotted for the decay of ^{240}Np* at extreme energies (a)E$_{c.m.}$=0.62 MeV and (b)E$_{c.m.}$=18.67 MeV respectively and at maximum angular momentum (ℓ_{max}). The ℓ_{max} is that value of angular momentum at which light particle cross-sections approach to zero. It may be noted that the characteristic behavior of fragmentation potential is different for minimum and maximum angular momentum and owing to the fission decay mode in the chosen reaction, the results is presented at ℓ_{max} only. In order to study the role of deformations on the decay of transuranic ^{240}Np* nucleus, the fragmentation potential is plotted for spherical approach as well as with inclusion of quadruple (β_2) deformation. At both energies, the magnitude of fragmentation potential is relatively lesser for spherical approach and increases with inclusion of deformations particularly for fragments heavier than $A_2 \geq 36$. This suggests that effect of deformations is significant for the heavy mass fragments (HMFs) and fission fragments but is relatively silent for light mass region. Further, comparing the fragmentation potential for spherical approach at both extreme energies across the barrier, it is observed that the magnitude of fragmentation potential changes while the structure of potential energy surfaces (PES) remain similar while going from minimum to maximum energy. In other words, the PES don't exhibit a significant change at extreme energies across the barrier for spherical approach. On the other hand, the structure of fragmentation potential looks somewhat different for deformed approach, at both extreme energies. Moreover, the fragmentation potentials show some dips in the case of deformed considerations which are missing in the spherical choices of fragmentation. Although, the sharp minima in the β_2-deformed fragmentation show the preference for the ^{17}B and ^{55}K clusters but they get ruled out because of their small penetrability as shown in Fig.3.3.

Further the role of deformations is also studied from the variation of preformation probability (P_0) plotted as a function of heavy mass fragment (A_i;i=70-176) as depicted in Fig.3.2 where (a) is plotted for E$_{c.m.}$=0.62 MeV (T=0.48 MeV) and (b) for E$_{c.m.}$=18.67 MeV (T=0.96 MeV) respectively. The curve is plotted at maximum angular momentum ℓ_{max}, for both spherical as well as deformed choice of decaying fragments. The deformations are found to influence the preformation probability (P_0) of the transuranic ^{240}Np* nucleus and it is observed that at the extreme en-

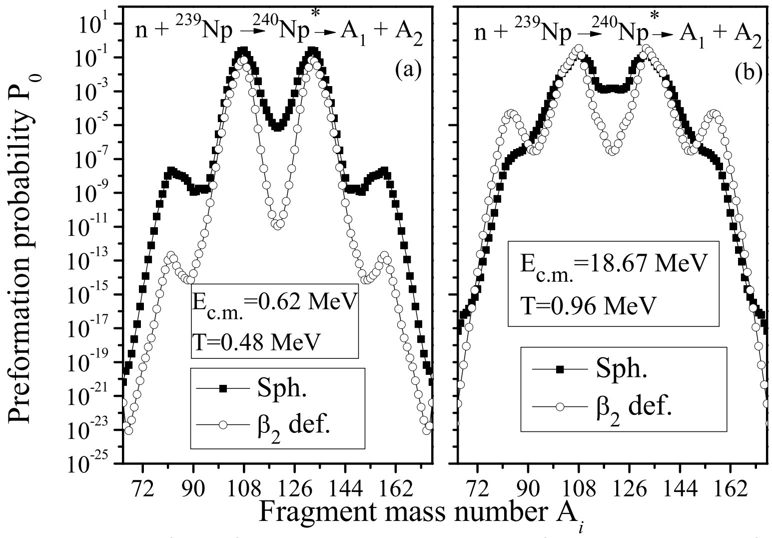

Figure 3.2: Variation of preformation probability for the decay of ^{240}Np* nucleus as a function of fragment mass A_i for spherical as well as β_2-deformed choice of fragmentation plotted at respective ℓ_{max} values at extreme centre of mass energies (a)$E_{c.m.}$=0.62 MeV and (b)$E_{c.m.}$=18.67 MeV.

ergies, the fragment mass distribution is asymmetric for spherical and deformed choice of fragmentation with very small contributions from symmetric region. The contribution of symmetric fission fragments is relatively less at minimum energy as compared to maximum energy. Apparently, the overall structure of preformation probability (P_0) is almost similar for spherical approach at both energies across the barrier. However, with inclusion of quadrupole deformations, the mass distribution of fragments changes significantly on going from below barrier to above barrier energy. These observations are consistent with those obtained earlier in Fig.3.1. Moreover, it is observed that the role of deformations is significant at both the energies, being more prominent at lower energy as expected. From the variation of P_0, it is evident that the dominant fission fragments contributing towards the decay of ^{240}Np* nucleus lie in the mass range A_2 =100-112 (and their complementary heavy fragments). Interestingly, the contributing fragments remain consistent for both the choices of fragmentation at extreme energies.

The DCM based calculations reproduce the experimental data for both the approaches using only parameter of model, the neck-length parameter Δ R. The

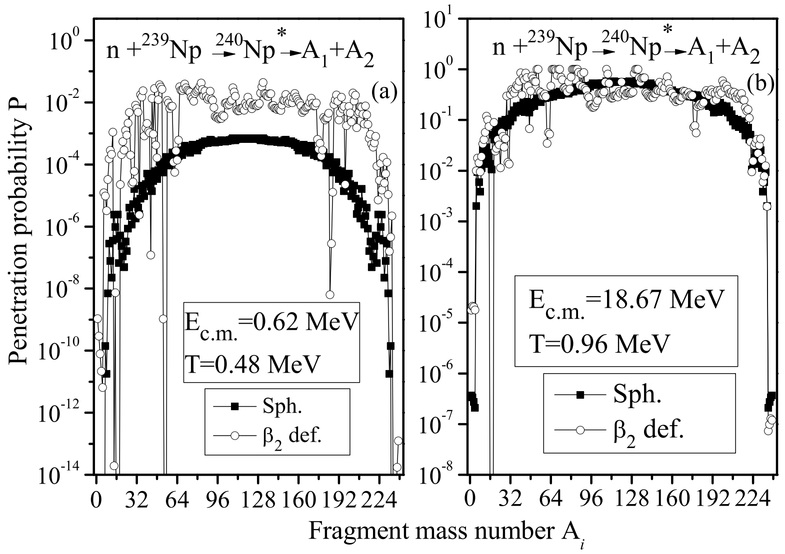

Figure 3.3: Penetrability P as a function of fragment mass A_2, for the decay of compound system ^{240}Np*, plotted at extreme energies (part (a) and (b) respectively) for spherical and deformed nuclei at ℓ=ℓ_{max}.

cross-sections for spherical systems are attained at relatively lower values of ΔR as compared to quadrupole (β_2) deformed approach. Table-3.1 shows the fission cross-sections for the decay of ^{240}Np* nucleus, calculated for the spherical fragmentation and with inclusion of quadrupole deformations within optimum orientation approach, compared with experimental data at extreme energies, $E_{c.m.}$=0.62 MeV and 18.67 MeV along with ΔR and ℓ_{max} values. Further, Fig.3.3 shows the penetrability P as a function of fragment mass A_i plotted for the decay of ^{240}Np* nucleus at ℓ=ℓ_{max} where part (a) corresponds to $E_{c.m.}$=0.62 MeV whereas part (b) corresponds to $E_{c.m.}$=18.67 MeV. It may be noted that the magnitude of P increases on going from $E_{c.m.}$=0.62 MeV to $E_{c.m.}$=18.67 MeV. Also, the difference in magnitude for spherical and deformed fragmentation is considerably large at $E_{c.m.}$=0.62 MeV which otherwise gets minimized at $E_{c.m.}$=18.67 MeV. This further signifies that the effect of deformations is more prominent at below barrier energies. It may be noted that the structure of penetrability shows maxima and minima for the quadrupole (β_2) deformed fragmentation, with some sharp minima emerging in light mass region along with ^{17}B and ^{55}K fragments (and their complementary frag-

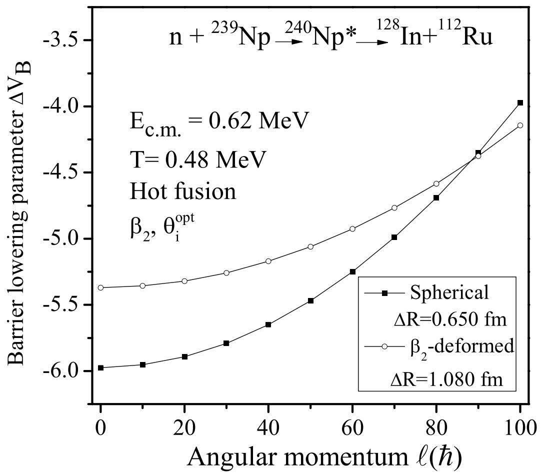

Figure 3.4: The barrier lowering parameter $\triangle V_B$ as a function of angular momentum $\ell(\hbar)$ at minimum energy $E_{c.m.}$=0.62 MeV plotted simultaneously for both spherical and deformed choices of fragmentation corresponding to the decay n+^{239}Np→^{240}Np*→^{128}In+ ^{112}Ru.

Table 3.1: The DCM calculated fission cross sections for the ^{240}Np* actinide nucleus formed in n-induced reaction. The cross-sections have been shown at extreme energies obtained for the spherical and quadrupole β_2-deformed choice of fragmentation as compared with experimental data. Also shown are the respective ΔR and ℓ_{max} values.

S. No.	E_{lab}	$E_{c.m.}$	T	spherical fragmentation			β_2-deformed fragmentation			$\sigma^{Expt.}$
	(MeV)	(MeV)	(MeV)	ΔR(fm)	$\ell_{max}(\hbar)$	σ^{DCM}(b)	ΔR(fm)	$\ell_{max}(\hbar)$	σ^{DCM}(b)	(b)
1	0.62	0.62	0.48	0.650	105	0.05	1.080	101	0.05	0.06
2	18.75	18.67	0.96	1.110	139	1.92	1.250	133	1.93	2.00

ments), as mentioned earlier. However, the structure is relatively smooth for the spherical choice. In framework of DCM, the role of deformations is also analyzed from the variation of barrier modification, ΔV_B (defined in Chapter-2), which is an in-built property of DCM, that enters through the neck-length parameter ΔR. Fig.3.4 depicts the variation of ΔV_B as a function of angular momentum, varying from ℓ=0$\hbar$ up to ℓ_{max}-value, for both spherical and deformed approach at minimum energy, $E_{c.m.}$=0.62 MeV . Fig.3.4 is plotted for the decay ^{240}Np*→^{128}In+ ^{112}Ru and it is observed that the magnitude of barrier modification is large at lower ℓ-values

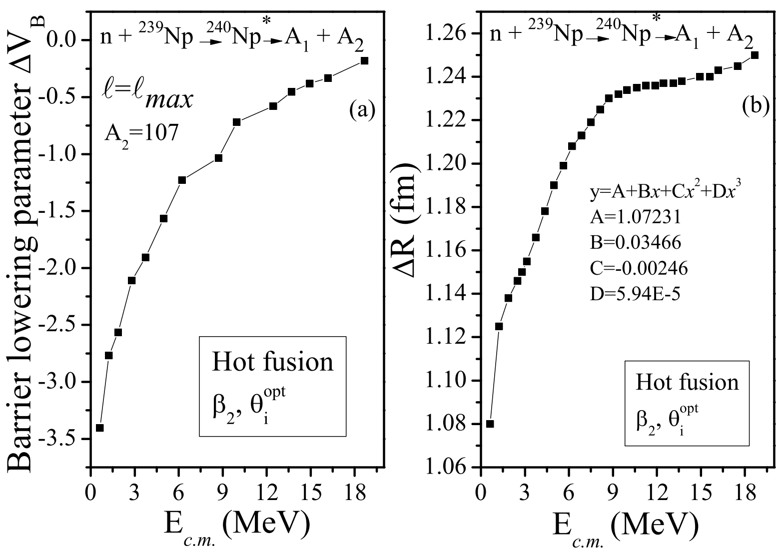

Figure 3.5: (a)The barrier lowering parameter $\triangle$ V_B as a function of $E_{c.m.}$ for deformed choice of fragmentation at ℓ=ℓ_{max} for most probable fission fragment A_2=107. (b)Variation of best-fitted neck-length parameter ΔR as a function of $E_{c.m.}$ for the reaction n+^{239}Np$\rightarrow$^{240}Np*$\rightarrow$$A_1$+$A_2$.

and decreases with increase in angular momentum, independent of the choice of fragmentation. Moreover, for both spherical and deformed considerations, it is observed that barrier modification is minimum for the highest energy $E_{c.m.}$=18.67 MeV and becomes maximum at $E_{c.m.}$=0.62 MeV. This suggests that for both spherical and deformed approach, lower barrier modification is required at highest energy and maximum angular momentum. Moreover, at minimum energy, relatively lesser barrier modification is needed for the quadrupole (β_2) deformations as compared to spherical fragmentation. This relative behavior for spherical and deformed approach justifies the observations drawn so far and suggests that deformations play a crucial role at below barrier energy.

As Fig.3.4 deals with an explicit variation of barrier lowering parameter at minimum energy only, an equivalent variation of ΔV_B is studied over a wide range of center-of-mass energies, varying from $E_{c.m.}$=0.62 MeV to 18.67 MeV as shown in Fig.3.5(a). This figure depicts the behavior of ΔV_B for the decay of most probable fission fragment, with inclusion of quadrupole deformation at ℓ=ℓ_{max}. It is to be noted that ΔV_B, is negative and non-zero at all energies which indicates that the barrier lowering is essential and in built in DCM. Evidently, for higher energies ΔV_B is relatively smaller in magnitude while it increases gradually with decrease in energy being maximum $\sim$ -3.4 MeV at minimum energy, $E_{c.m.}$=0.62 MeV. In framework of DCM, the barrier-lowering, ΔV_B is controlled through only parameter of model, neck-length parameter ΔR. Fig.3.5(b) shows the variation of ΔR as a function of $E_{c.m.}$, for the fission decay of ^{240}Np* nucleus. It is observed that the magnitude of ΔR increases with the increase in center-of-mass energy. The increase in ΔR value as a function of energy can be explained using second order polynomial shown in Fig. 3.5(b). Moreover, the magnitude of ΔR is higher for the β_2-deformed choice of fragmentation as compared to spherical approach (see Table-3.1).

Corresponding to the ΔR values illustrated in Fig.3.5(b), the DCM calculated fission cross-sections are depicted in Fig.3.6 and are compared with the measured experimental data and theoretical results of JENDEL-4.0, ENDF/B-VII.0 and CENDL-3.1. The DCM calculated fission cross-sections (open square) are found to be in nice agreement with the the experimental data within the optimized choice of neck-length parameter ΔR. The fission cross-sections calculated using DCM for the decay of ^{240}Np$*$ system, with quadrupole (β_{2i}) deformed choice of fragmentation, compared with the experimental data [5] are tabulated in Table-3.2 along with the related parameters. Interestingly, the fission cross-sections for the decay of ^{240}Np* show a triple humped variation, representing enhanced cross-sections at three energies viz. $E_{c.m.}$=1.87 MeV, 8.75 MeV and 17.57 MeV. In framework of DCM, the relatively higher cross-sections corresponding to these three energies are achieved using smooth variation in neck-length parameter. This enhancement may be attributed to the consideration of orientational degree of freedom of the decaying fragments and this effect of orientations is explored below.

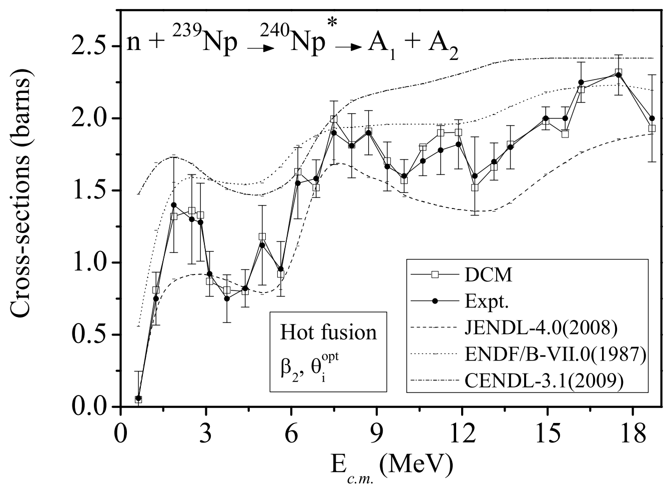

Figure 3.6: Comparison of DCM based cross-sections for the decay of ^{240}Np* system with measured experimental data and other available theoretical estimates over a wide range of energies varying from $E_{c.m.}$=0.625-20 MeV.

3.2.2 Role of orientational degree of freedom in the decay of ^{240}Np*

As clarified from Table-3.2, the fission cross-sections for the decay of ^{240}Np* possess a greater magnitude as compared to the other energies and this may be attributed to the orientational degree of freedom of the decaying fragments. To have a clear picture of the effect of orientations, the fragmentation potential is plotted as a function of fragment mass A_2 for both hot (equatorial) and cold (polar) orientations at (a) $E_{c.m.}$=0.62 MeV and (b)$E_{c.m.}$=1.8 MeV in Fig.3.7. Evidently, a significant change in the structure and magnitude of potential energy surfaces is observed when hot (equatorial) compact orientation is replaced by cold (polar) elongated configuration. The effect of orientation is more prominent for intermediate, heavy mass and fission fragments while the light particles region remains almost unaffected. Also, it is observed that the mass distribution is asymmetric for both the orientations, but it is relatively more symmetric for equatorial configuration as compared to polar orientation. However, despite of the change in mass distribution, the fission fragments contributing towards the decay cross-sections remain the same for both the orientations, ranging from A_2=100-112 (and complementary fragments). Compar-

Table 3.2: The fission cross sections obtained with the inclusion of quadrupole (β_2)-deformation for the ^{240}Np* system at some incident energies across the barrier. Also the experimental measured cross-sections for the n-induced reaction are tabulated along with ΔR and the ℓ_{max} values.

S. No.	E_{lab} (MeV)	$E_{c.m.}$ (MeV)	T (MeV)	ΔR (fm)	ℓ_{max} ($\hbar$)	σ^{DCM} (b)	$\sigma^{Expt.}$ (b)
1	0.62	0.62	0.48	1.080	101	0.05	0.06
2	1.25	1.24	0.51	1.125	104	0.81	0.75
3	**1.87**	1.86	0.53	1.138	106	1.32	**1.40**
4	2.50	2.49	0.56	1.146	106	1.36	1.30
5	2.81	2.80	0.56	1.150	107	1.33	1.28
6	3.13	3.12	0.57	1.155	107	0.87	0.92
7	3.75	3.73	0.59	1.166	107	0.81	0.75
8	4.39	4.37	0.62	1.178	108	0.80	0.82
9	5.00	4.97	0.63	1.190	108	1.18	1.12
10	5.64	5.62	0.65	1.199	109	0.92	0.95
11	6.25	6.22	0.67	1.208	112	1.63	1.55
12	6.90	6.87	0.69	1.213	113	1.52	1.58
13	7.52	7.49	0.71	1.219	116	1.99	1.90
14	8.15	8.12	0.72	1.225	118	1.81	1.81
15	**8.75**	8.71	0.74	1.230	118	1.91	**1.90**
16	9.41	9.37	0.75	1.232	120	1.70	1.66
17	10.00	9.95	0.74	1.234	121	1.57	1.60
18	10.66	10.62	0.79	1.235	122	1.80	1.70
19	11.29	11.24	0.80	1.236	124	1.90	1.78
20	11.92	11.87	0.82	1.236	124	1.90	1.82
21	12.50	12.44	0.83	1.237	124	1.52	1.60
22	13.17	13.12	0.84	1.237	128	1.66	1.70
23	13.75	13.69	0.86	1.238	130	1.82	1.80
24	15.00	14.93	0.88	1.240	130	1.98	2.00
25	15.68	15.62	0.90	1.240	132	1.89	2.00
26	16.25	16.18	0.91	1.240	133	2.20	2.25
27	**17.57**	17.49	0.94	1.245	133	2.32	**2.50**
28	18.75	18.67	0.96	1.250	133	1.93	2.00

ing the fragmentation potential for both hot and cold orientations at two energies, plotted in Fig.3.7(a) and (b) it is observed that effect of orientation is relatively more prominent at $E_{c.m.}$=1.8 MeV, for which the cold orientation is consistently favorable for all fragments. Whereas, at $E_{c.m.}$=0.62 MeV, the hot orientation is favorable for intermediate mass region and is replaced by cold orientation for higher mass fragments. Also, the difference in behavior of PES observed due to change in orientation is more at $E_{c.m.}$=1.8 MeV, which may be associated with relatively enhanced cross-section. The experimentally observed cross-sections for these three

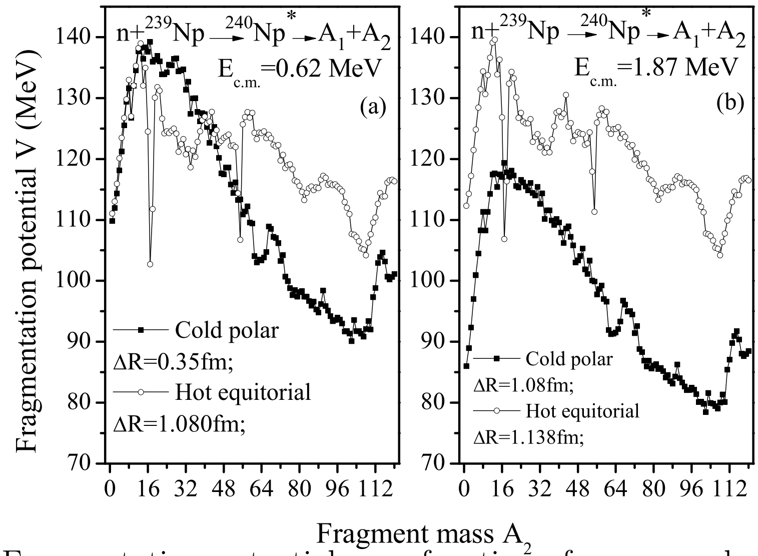

Figure 3.7: Fragmentation potential as a function of mass number for the decay of ^{240}Np* nucleus. Panel (a) is plotted at $E_{c.m.}$=0.62 MeV and panel (b) is plotted at $E_{c.m.}$=1.87 MeV for cold polar orientation (filled blocks) and hot equatorial orientations (hollow circles).

energies have been attained successfully (within error limits) by using the only parameter of the model, the neck-length parameter ΔR. For cold (polar) elongated orientation the values of the best-fit ΔR are 1.08fm, 1.10fm and 1.12fm whereas for hot (equatorial) compact orientation it is 1.138fm, 1.230fm and 1.245fm at energy 1.87 MeV, 8.75 MeV and 17.57 MeV respectively. Thus, the cold orientation criteria seems to work at relatively lower ΔR values.

3.2.3 Role of moment of inertia

After studying the role of deformations and orientations, an attempt is made to investigate another significant parameter- the moment of inertia and we have employed two approaches of moment of inertia namely, the sticking ($I=I_S$) and non-sticking ($I=I_{NS}$) limit of moment of inertia. The effect of moment of inertia enters the DCM via the centrifugal potential V_ℓ [defined in Chapter-2] which forms a part of fragmentation potential. To analyze the effect of choice of limits of moment of inertia, the fragmentation potential for the decay of ^{240}Np* is plotted as a func-

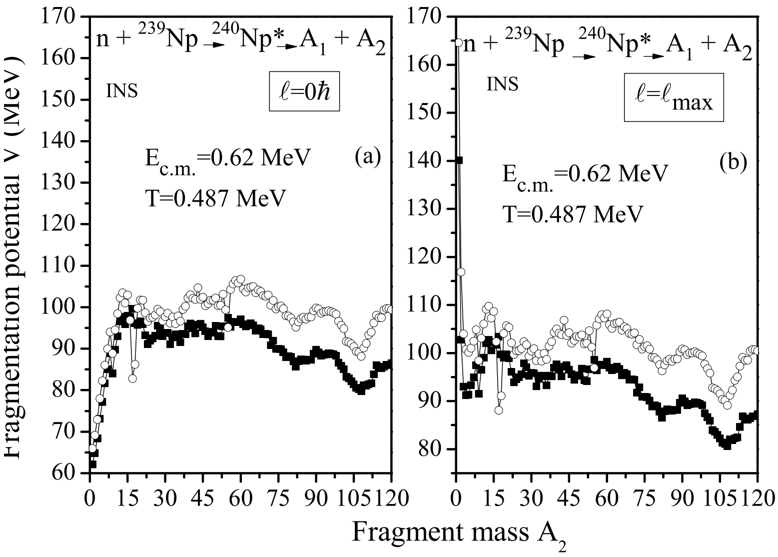

Figure 3.8: Variation of fragmentation potential as a function of fragment mass(A_2) for the decay of ^{240}Np* nucleus at $E_{c.m.}$=0.62 MeV by taking non-sticking limits of moment of inertia simultaneously for spherical and β_2 deformed systems plotted at (a)ℓ=0$\hbar$ and (b)ℓ=ℓ_{max} respectively.

tion of fragmentation mass A_2 using I=I_{NS} in Fig. 3.8. The effect of choice of moment of inertia is more prominent at maximum angular momentum, ℓ=ℓ_{max} as shown in Fig.3.8(b) as compared to ℓ=0$\hbar$, shown in Fig.3.8(a). It is observed that the structure of potential energy surfaces change significantly for the light particles whereas, no much effect is observed on the behavior of intermediate, heavy mass and fission fragments(compare Fig.3.8(b) with Fig. 3.1(a)). Apparently, for the I_{NS} choice, the magnitude of fragmentation potential is higher for quadrupole (β_2) deformed approach as compared to spherical approach. Moreover, it is found that for a given value of centrifugal potential, I_{NS} approach contributes up to fewer units of angular momentum as compared to I_S approach. On replacing the sticking choice with non-sticking one, the ℓ_{max} decreases from 105$\hbar$ and 101$\hbar$ to 18$\hbar$ and 20$\hbar$ for spherical and deformed systems respectively. Also, the fission cross-sections for the non-sticking I_{NS} limit have been fitted at higher neck-length being ΔR=0.960fm and ΔR=1.338fm for spherical and deformed approach respectively as compared to 0.650fm and 1.080 fm for sticking limit. Thus, it may be concluded that for n-induced reaction, the I_S approach is more favorable for fission decay at all energies,

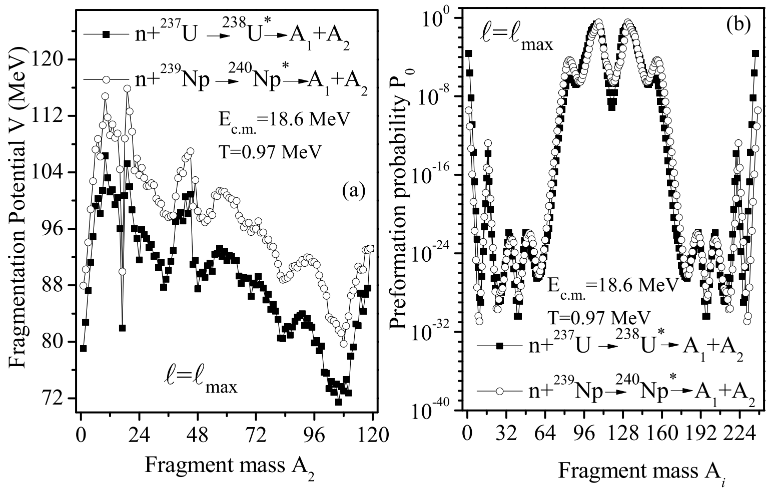

Figure 3.9: (a) Fragmentation potential plotted for the decay of ^{238}U* and ^{240}Np* nuclei at maximum angular momentum(ℓ_{max}) and at $E_{c.m.}$=18.6 MeV for β_2 deformed choice of fragmentation with optimum orientations. (b)Represents the same but for preformation probability P_0.

while the I_{NS} choice of moment of inertia seems good at near and below barrier region.

3.2.4 Comparative analysis of decay profile of ^{240}Np* and ^{238}U*

In order to have a comprehensive study of n-induced reactions, the decay profile of ^{240}Np* is compared with another even mass system, ^{238}U* nucleus, formed in n-induced reaction [19] at same $E_{c.m.}$. It is worth mentioning that, both these nuclei have same iso-spin ratio (N/Z=1.58) and are formed at similar incident energies. Fig.3.9(a) and (b) show the comparative study of these nuclei in terms of fragmentation potential and the preformation probability respectively for the quadrupole deformed approach at maximum energy, $E_{c.m.}$=18.67 MeV. It is observed that apart from some change in magnitude of fragmentation potential (see Fig.3.9(a)), no change in structure of PES is observed for ^{238}U* and ^{240}Np* nuclei. Moreover, for both the nuclei an asymmetric mass distribution is observed with almost similar prominent decay fragments. This suggests that the heavy mass ac-

Table 3.3: The DCM calculated fission cross sections for the ^{238}U* actinide nucleus formed in n-induced reaction. The cross-sections have been shown at extreme energies obtained for the quadrupole β_2-deformed choice of fragmentation and for the spherical choice of fragmentation compared with experimental data. Also shown are the respective ΔR and ℓ_{max} values.

S. No.	E_{lab}	$E_{c.m.}$	T	spherical fragmentation			β_2-deformed fragmentation			$\sigma^{Expt.}$
	(MeV)	(MeV)	(MeV)	ΔR(fm)	$\ell_{max}(\hbar)$	σ^{DCM}(b)	ΔR(fm)	$\ell_{max}(\hbar)$	σ^{DCM}(b)	(b)
1	0.67	0.67	0.52	0.788	107	0.41	1.100	103	0.42	0.42
2	18.68	18.60	0.98	1.120	134	1.20	1.240	133	1.14	1.12

tinide nuclei formed in n-induced reaction are more favorable towards fission, with fragments lying in mass range A_2=100-112 (and complementary fragments). Thus, from the identical behavior of the fragmentation path and mass distribution for both the nuclei, it may be concluded that results obtained for the ^{240}Np* nucleus may also be valid for neighboring nuclei, formed via n-induced reaction. The neck-length parameter, ΔR and maximum angular momentum, ℓ_{max} used to calculate fission cross-sections for ^{238}U* nucleus, at extreme energies across the barrier for both the choices of fragmentation are tabulated in Table-3.3. The cross-sections are found to be in nice agreement with measured experimental data.

3.3 Conclusions

This chapter presents the reaction dynamics governing the decay of compound nucleus ^{240}Np* formed in n-induced reactions over incident beam energy of E_n=0.62-18.75 MeV [5]. The heavy mass nucleus ^{240}Np* formed here decays via fission channel and the cross-sections are fitted using the neck-length parameter ΔR of the DCM. The decay of ^{240}Np* is analyzed for spherical and deformed fragmentation and it is concluded that with inclusion of deformations, the decay profile becomes more asymmetric, however, the fragments contributing towards the decay cross-sections remain same (A_2=100-112). The enhancement in cross-sections at the three energies (see Fig. 3.6) may be attributed to the orientations of the decaying fragments as change in structure is observed when hot (equatorial) orientations are replaced with cold (polar) configuration. The moment of inertia also plays a significant role in the decay analysis of ^{240}Np* because of the structural variations that come in to picture when the sticking limits of moment of inertia are replaced with non-sticking limits. The variations are prominent for lighter fragments. Additionally, the comparative analysis of decay profiles of ^{240}Np* and ^{238}U* reveals that both the nuclei possess identical fragmentation structures with small variations in magnitude. The cross-sections for the decay of ^{238}U* also find nice agreement with the experimental data [19].

It is emphasized that the compound nucleus ^{240}Np* decays mainly via fission channel attributed to its heavy mass. the role of deformations, orientations and moment of inertia is duly addressed. In order to explore the competing decay mechanism called evaporation residue, we have explored the decay of a light mass system ^{61}Ni* formed in n-induced reaction. The related studies and observations are presented in the next chapter, where in addition to the study of decay of light mass nuclei formed in n-induced reactions, the decay analysis for the compound nuclei formed in p-induced reactions is also presented. The decay of few more light mass nuclei is also explored for comprehensive analysis of decay patterns observed in light mass region.

Bibliography

[1] D. Karadimos *et al.*, Phys. Rev. C **89** 044606 (2014).

[2] C. Bhatia *et al.*, Phys. Rev. C **91** 064604 (2015).

[3] P. Salvador-Castiňeira *et al.*, Phys. Rev. C **92** 014620 (2015).

[4] N. Fotiades et al. Phys. Rev. C **91** (2015) 064614.

[5] A. Czeszumska *et al.*, Phys. Rev. C **87** 034613 (2013).

[6] R. K. Gupta, M. Balasubramaniam, R. Kumar, D. Singh, and C. Beck, Nucl. Phys. A **738** 479-482 (2004); M. Kaur, and M. K. Sharma, Eur. Phys. J. A **50** 61 (2014).

[7] R. K. Gupta, S. K. Arun, R. Kumar, and M. Bansal, Nucl. Phys. A **834** 176c-179c (2010).

[8] D. Jain, R. Kumar, M. K. Sharma, and R. K. Gupta, Phys. Rev. C **85** 024615 (2012).

[9] R. Kumar, K. Sandhu, M. K. Sharma, and Raj K. Gupta, Phys. Rev. C **87** 054610 (2013); K. Sandhu, G. Kaur and M. K. Sharma, Nucl. Phys. A **921** 114 (2014).

[10] G. Sawhney and M. K. Sharma, Eur. Phys. J. A **48** 57 (2012); G. Kaur and M. K. Sharma, Phys. Rev. C **87** 044601 (2013); G. Kaur, D. Jain, R. Kumar, M. K. Sharma, Nucl. Phys. A **916** 260 (2013).

[11] G. Sawhney, G. Kaur, M. K. Sharma, and R. K. Gupta Phys. Rev. C **88** 034603 (2013).

[12] M. Kaur, R. Kumar, and M. K. Sharma, Phys. Rev. C **85** 014609 (2012); K. Sandhu, M. K. Sharma and R. K. Gupta, Phys. Rev. C **85** 024604 (2012).

[13] S. S. Malik, and R. K. Gupta, Phys. Rev. C **39** 1992 (1989).

[14] R. K. Gupta, and W. Greiner, Int. J. Mod. Phys. E **3** 335 (1994).

[15] G. Sawhney, M. K. Sharma, and R. K. Gupta, Phys. Rev. C **83** 064610 (2011).

[16] P. Möller, J. R. Nix, W. D. Myers, and W. J. Swiatecki, At. Data Nucl. Data Tables, **59** 185 (1995).

[17] R. K. Gupta, M. Balasubramaniam, R. Kumar, N. Singh, M. Manhas, and W. Greiner, J. Phys. G: Nucl. Part. Phys. **31** 631 (2005); R. K. Gupta, Monika Manhas, and W. Greiner, Phys. Rev. C **73** 054307 (2006).

[18] G. Kaur, N. Grover, K. Sandhu, and M. K. Sharma, Nucl. Phys. A **927** 232-248 (2014); R. K. Gupta, Niyti, M. Manhas, and W. Greiner, J.Phys.G; Nucl. Part. Phys. **36** 115105 (2009).

[19] J. T. Burke et al. Phys. Rev. C **73** 054604 (2006).

Chapter 4

Investigation of particle evaporation from the nuclei formed in n and p-induced reactions

4.1 Introduction

The previous chapter presents the analysis of the decay mechanism of ^{240}Np* formed in n-induced reaction and as the mass of the compound nucleus A_{CN}>200, the preferable decay mode is observed to be fission [1]. However, it would be quite interesting to explore the decay of a compound nuclei formed in similar n-induced reaction and to analyze the fragmentation structure and the associated decay paths. For this purpose, the decay analysis of ^{61}Ni* formed in n+^{60}Ni reaction is carried out and this investigation helps us in analyzing the effect of mass the decaying CN on the chosen decay path, that means the present study helps in establishing a comprehensive investigation of the decay of CN with heavy (A_{CN}=240) and relatively lighter mass (A_{CN}=61) nuclei formed in n-induced reactions which in turn may impart valuable understanding of the dynamics.

Keeping this in mind, the decay of ^{61}Ni* nucleus formed in n+^{60}Ni reaction is studied via DCM [2–8] which is reformulation of PCM [9–11] over an energy spread of E_{beam}=1-100MeV in reference to experiment [12]. The compound nucleus with A_{CN}=61 prefers to decay via particle evaporation popularly known as evaporation residue. Interestingly, the experimental data provides cross-sections for the formation of daughter nucleus ^{57}Fe and the excitation function plot for particle evaporation shows a double humped variation with incident beam energy $E_{c.m.}$ where the peak at lower energy corresponds to α-emission while the one at higher energy originates from $2p2n$-emission. Hence, the effect of increment in incident energy is such that at higher excitation energies, the α-emission is transmuted by $2p2n$-emission in the decay channel. To analyze the role of deformations, the calculations are done for hot-deformed fragments having optimized orientations taken from the tables of [13] and the experimental data is fitted nicely using the methodology of DCM. Also, within the sticking limits of moment of inertia, I_S (discussed in Chapter-2) the data could be addressed only for limited range of incident beam energy i.e. E_n∼1-10MeV but when sticking limits of moment of inertia (I_S) is replaced with non-sticking limits (I_{NS}) [14] the comparison with experimental data improves significantly. Another point to be noted here is that the transmutation observed in the emission of α-particles at lower energies and $2p2n$-emission at higher energies is explained on the basis of temperature dependance of binding energy exercised within the frame-work of DCM [15]. Also, the effect of mass and hence charge, of the compound nucleus on α and $2p2n$-emission is investigated and a comparative analysis is done for various systems involving light to heavy mass nuclei formed in similar reactions [16–18].

In addition to this, the dynamics of p-induced reactions is also explored, which helps us to investigate the role of different projectile on the decay of the compound nuclei with masses lying in similar light mass region A_{CN}∼70-80. For this purpose, DCM has been employed to work out the dynamics involved in decay of three compound nuclei ^{77}As*, ^{83}Br* and ^{86}Sr* formed in proton-induced reactions p+^{76}Ge, p+^{82}Se and p+^{85}Rb at incident beam energies of E_{beam}=1-5 MeV. Here again, $E_{c.m.}$ corresponding to the beam energy lies in the same range. The data for n-evaporation has been addressed adequately in accordance with the experimental results of [19–21]. The role of angular momentum and deformations of the decaying fragments has been explored and in addition to this, the sensitivity of DCM calculated cross-sections is investigated in reference to level density parameter (LDP) by varying its magnitude from 6 to 10 and by including mass dependence in LDP in ref. to [22]. The corresponding significance of the involved parameters is studied from the variations in fragmentation structure.

Section-4.2 comprises of the calculations and results related to decay patterns of the compound systems formed in n and p-induced reactions. In the following Section-4.3, the conclusions drawn so far are highlighted.

4.2 Results and discussion

This sections presents the decay analysis of ^{61}Ni* formed in n+^{60}Ni reaction over an energy beam of E_n=1-100 MeV [12] and that of ^{77}As*, ^{83}Br* and ^{86}Sr* formed in proton-induced reactions p+^{76}Ge, p+^{82}Se and p+^{85}Rb at incident beam energies of E_{beam}=1-5 MeV [19–21].

4.2.1 Competing analysis of α and $2p2n$-emission from ^{61}Ni*

(a) Role of moment of inertia: This sections deals with the decay analysis of compound nucleus ^{61}Ni* formed in n+^{60}Ni reaction over an energy spread of E_n=1-100 MeV. The compound nucleus chooses to decay via α-emission at low energies and $2p2n$-multinucleon emission at high energies leaving behind the daughter nucleus ^{57}Fe and the experimental cross-sections are fitted by optimizing the neck-length parameter ΔR. The calculations are done with non-sticking limits I_{NS}, as with the use of sticking limits (I_S), the experimental data could not be addressed adequately.

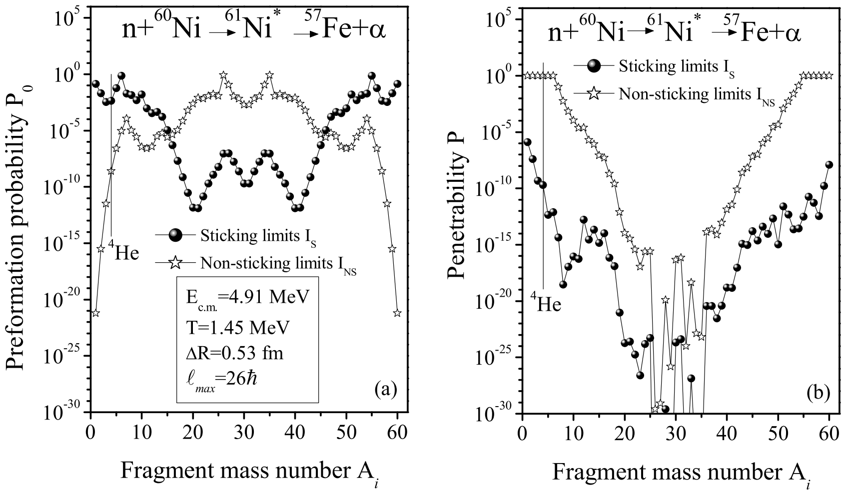

Figure 4.1: (a) Preformation probability and (b) Penetrability P plotted as a function of fragment mass A_2 for the decay of $^{61}Ni^*$ nucleus at $E_{c.m.}$=4.918 MeV at ℓ_{max}. The solid sphere represents the results using sticking limits (I_S) and stars represent the use of non-sticking limits (I_{NS}).

This may be explained in terms of modifications in preformation P_0 and penetrability P, that emerge from the replacement of I_S with I_{NS}. For this purpose, preformation probability P_0 and penetrability P are plotted as a function of fragment mass A_2 at $E_{c.m.}$=4.91 MeV, using both the limits of moment of inertia sticking(I_S) and non-sticking(I_{NS}) as shown in Fig.4.1. This figure clarifies that a change in structure as well as magnitude is observed for both P_0 and P when the two limits of moment of inertia are interchanged.

The magnitude of P_0 of lighter fragments is higher for I_S choice as compared to I_{NS} choice signifying that I_S choice favors the α-emission while the penetrability P-values for light charged particles is enhanced significantly and this enhancement in the penetrability shows up in the estimation of cross-sections, thereby making the non-sticking approach more relevant for this analysis. Also, Fig.4.1(b) reveals that the non-sticking approach I_{NS} gives a relatively smoother variation for penetrability P as compared to that for sticking approach I_S. The corresponding values of P_0 and P for α-cluster are taken as marked in Fig.4.1(a) and (b) by vertical lines and it is

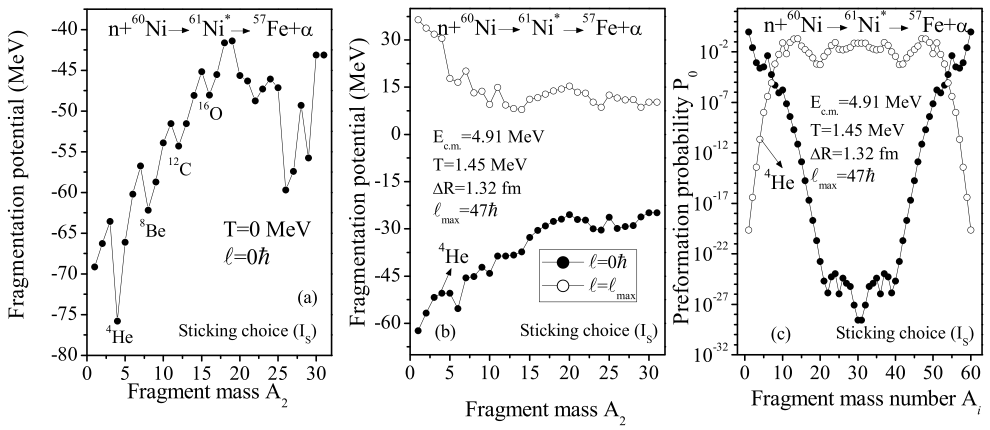

Figure 4.2: Study of fragmentation potential [(a)T=0MeV and (b) T=1.45 MeV] and (c) preformation probability P_0 for the decay of $^{61}Ni^*$ nucleus plotted at center of mass energy $E_{c.m.}$=4.91 MeV (equivalently E_n=5.00 MeV) using sticking limits of moment of inertia (I_S) at $\ell=0\hbar$ and $\ell=\ell_{max}$ values

noted that for an α-cluster, $P_0(I_{NS})=10^{-6}\times P_0(I_S)$ and $P(I_{NS})=10^9\times P(I_S)$. Hence, by interchanging the limits of moment of inertia, penetrability plays the lead role in making the non-sticking approach more favorable towards light charged particle cross-sections. It is to be added that with the use of non-sticking approach the experimental data is addressed successfully over the whole energy range $E_n\sim$1-100 MeV for optimum neck-length parameter ΔR and corresponding values of ℓ_{max}. The DCM calculated cross-sections are shown along with best-fit values of ΔR and the other terms involved in calculations in Table-4.1.

(b) Role of temperature and angular momentum: The temperature and angular momentum play vital role in affecting the fragmentation path of a compound nucleus. To investigate the role of temperature and ℓ-values, the fragmentation potential for the decay of compound nucleus $^{61}Ni^*$ is plotted as a function of fragment mass A_2 at T=0 MeV ($\ell=0\hbar$ case) as shown in Fig.4.2(a) and is compared with the fragmentation structure of the decay of $^{56}Ni^*$ (Fig.3 of [23]). It has been observed that the structure of fragmentation potential is similar for both the systems at T=0 MeV signifying that the LPs are favored at $\ell=0\hbar$ attributed to their lower magnitudes of fragmentation potential. The strong dips seen in the fragmentation curve for both the compound systems correspond to α-structuring at T=0 MeV. Further to analyze the effect of beam energy or temperature T and to pursue the competing analysis of emergence of α-emission at lower incident beam energies and $2p2n$-emission at higher incident energies, the fragmentation potential is plotted at lower beam energy $E_{c.m.}$=4.91 MeV (or T=1.45 MeV) in Fig.4.2(b) and it again infers the emission of light charged particles at lower ℓ-values and a change in fragmentation pattern favoring the decay of fragments with $A_2 \geq 5$ at higher values of angular momentum(ℓ_{max}). Along with it, the preformation probability P_0 is also plotted at same $E_{c.m.}$ in Fig.4.2(c) and it is clear that lower ℓ-values (shown by filled circles) favor the emission of light charged particles with $A_2 \leq 4$ as they have higher P_0 values and again as ℓ_{max} values are approached, the potential energy surface signify the decay of the compound nucleus via near symmetric fragments and some intermediate mass fragments (IMFs) as the competing decay mode. Here IMF refers to fragments with A_2=5-20.

Further in Fig.4.3(a) and (b), fragmentation potential is plotted as a function of fragment mass A_2 for the three energies $E_{c.m.}$=4.91, 49.30 and 96.39 MeV (and equivalently temperature T=1.45, 2.96 and 3.99 MeV) covering the whole spread of experimentally available data [12] respectively for $\ell=0\hbar$ and $\ell=\ell_{max}$ values. From Fig.4.3(a) it is clear that at $\ell=0\hbar$, the light charged particles with $A_2 \leq 4$ correspond to lower magnitudes of fragmentation potential as compared to that for heavier mass fragments. It seems to suggest that the compound nucleus $^{61}Ni^*$ prefers to decay via emission of light charged particles at lower angular momentum values. On the other hand when we transmute towards higher values of angular momentum, a change in fragmentation structure is observed indicating that heavier fragments tend to have lower magnitude of fragmentation potential. Moreover, if we compare the magnitude of fragmentation potential for α-emission for all the three energies, it is seen that the fragmentation value is least for minimum energy $E_{c.m.}$=4.91 MeV (T=1.45

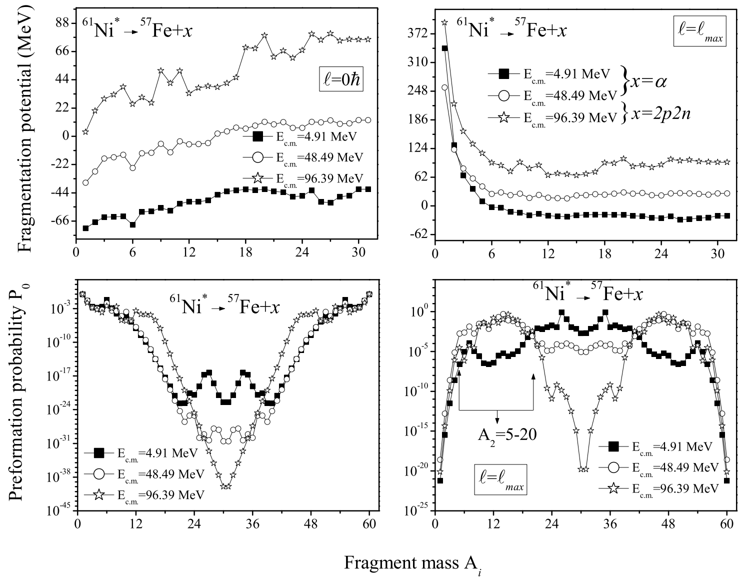

Figure 4.3: Fragmentation potential and Preformation probability plotted as a function of fragment mass A_2 for the decay of $^{61}Ni^*$ nucleus plotted for (a) ℓ=0$\hbar$ and (b) $\ell=\ell_{max}$ case at peak energies $E_{c.m.}$=12.39 MeV and 48.49 MeV using non-sticking (I_{NS}) approach.

MeV). The minimum value of fragmentation potential for α-cluster at $E_{c.m.}$=4.91 MeV signifies that the emission of α-cluster is favored at lowest energy. The effect of angular momentum and center of mass energy ($E_{c.m.}$) or T on the decay of compound nucleus is also analyzed via the preformation probability pattern as shown in Fig.4.3(c) and (d). Here Fig.4.3(c) and (d) are same as Fig.4.3(a) and (b) but plotted for preformation probability. Same results are evident here and one may clearly see that the decay of light charged particles is favored at lower angular momentum. Also, it is observed that the decay pattern of compound nucleus $^{61}Ni^*$ gets modified at different center of mass energies and hence temperature T. From Fig.4.3(d); it is clear that at $E_{c.m.}$=4.91 MeV (T=1.45 MeV) the preformation probability is higher for heavy mass fragments signifying that the compound nucleus undergoes near symmetric decay at high ℓ-values. As the center of mass energy $E_{c.m.}$ or T is increased, a change in potential energy surface (PES) is observed and a drift from symmetric to asymmetric configuration is observed. At

Table 4.1: DCM based cross sections for the decay of compound system ^{61}Ni* via α and $2p2n$-emission along with ΔR and the ℓ_{max} values. The experimentally measured cross-sections are also tabulated

S. No.	E_n (MeV)	$E_{c.m.}$ (MeV)	T (MeV)	ΔR (fm)	ℓ_{max} ($\hbar$)	cross-sections σ_α	σ_{2p2n}	$\sigma_{expt.} \pm \Delta\sigma$
1	5.00	4.91	1.45	0.53	26	2.12	0.62	2.00±1.1
2	5.70	5.60	1.49	0.70	26	5.05	0.67	4.50±1.1
3	6.50	6.39	1.53	0.79	27	6.39	0.89	6.00±1.1
4	7.50	7.37	1.58	0.80	29	5.88	0.98	6.10±1.1
5	8.80	8.65	1.64	1.67	30	8.03	3.31	8.00±1.1
6	10.40	10.22	1.71	2.05	32	12.10	6.57	12.60±1.3
7	12.60	12.39	1.81	2.25	33	12.80	5.72	12.50±1.4
8	15.40	15.14	1.92	1.95	33	8.34	3.38	8.50±1.4
11	29.30	28.81	2.40	2.05	33	8.59	6.40	8.20±1.1
12	34.30	33.73	2.55	2.40	34	10.80	8.67	11.50±1.1
13	40.80	40.13	2.74	2.40	35	13.50	11.90	14.20±1.1
14	49.30	48.49	2.96	2.45	35	13.30	14.70	15.80±1.1
15	61.00	59.99	3.24	2.45	35	10.40	12.10	12.10±0.9
16	74.90	73.67	3.37	2.20	33	6.69	8.27	8.90±1.0
17	98.00	96.39	3.99	2.20	33	4.62	7.33	7.30±0.9

$E_{c.m.}$=48.49 MeV (T=2.96 MeV), the compound nucleus ^{61}Ni* starts following the asymmetric decay mode with fragments of intermediate mass region (with A_2=5-20 plus their complimentary fragments) forming the decay path. And at $E_{c.m.}$=96.39 MeV (T=3.99 MeV), the fragmentation pattern of the compound nucleus becomes relatively more asymmetric, with IMFs forming the preferred decay mode.

(c)Relative emergence of α and $2p2n$ at different $E_{c.m.}$ or T values:

The experimentally available excitation functions for the decay of ^{61}Ni* or for the formation of daughter nucleus ^{57}Fe show a double humped structure where the peak at lower energy correspond to α-emission and another peak at higher energy signifies $2p2n$-emission. In order to understand the α-emission at lower energy and $2p2n$-emission at higher energy, the preformation probability P_0 of the respective

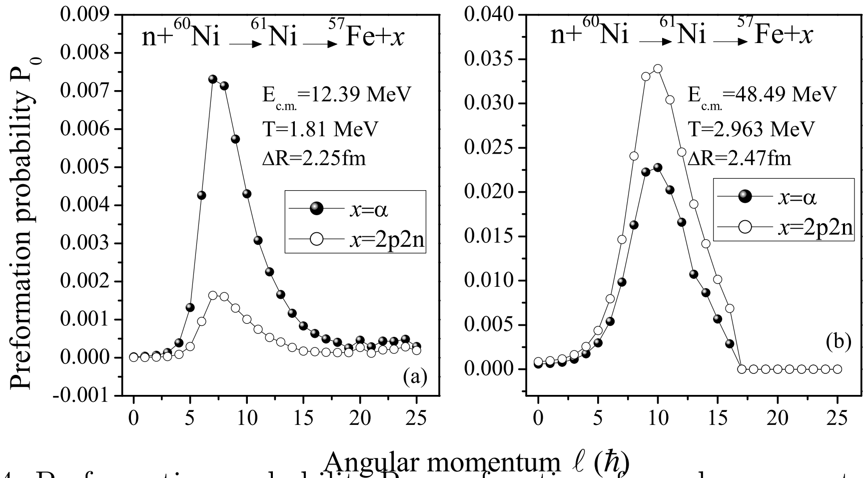

Figure 4.4: Preformation probability P_0 as a function of angular momentum (ℓ) plotted simultaneously for α and $2p2n$-emission at the two peak energies (a)$E_{c.m.}$=12.39 MeV and (b) $E_{c.m.}$=48.49 MeV at corresponding values of ΔR and ℓ_{max}.

clusters is plotted as a function of angular momentum(ℓ) in Fig.4.4 at energies corresponding to the peaks in excitation function plot. Fig.4.4(a) is plotted at $E_{c.m.}$=12.39 MeV while part (b) is plotted for $E_{c.m.}$=48.49 MeV and these energies lie across the point where transmutation is observed experimentally [12]. It is clear that at $E_{c.m.}$=12.39 MeV, the preformation probability of α-emission (filled spheres) has much higher magnitude than that of $2p2n$-emission (hollow circles) and the trend gets reverted as we shift towards higher energy signifying $2p2n$-emission to be more prominent. In other words the formation probability of $2p2n$-emission starts superseeding the α-emission with increase in incident energy. Also, it is seen that α and $2p2n$-emission show maximum probability of emission around angular momentum ℓ=10$\hbar$ while for $\ell \leq 5\hbar$ and $\ell \geq 18\hbar$, both α and $2p2n$-emission seems to be equally probable. So it can be concluded that light cluster or multi-nucleon emission from a hot excited compound nucleus is highly sensitive towards energy as well as angular momentum of the decaying system. Note that in DCM based calculations, α and $2p2n$-emission are differentiated on the basis of binding energies and the transmutation is associated with the temperature dependence of the binding energies, which forms the essential part of the fragmentation potential. The various

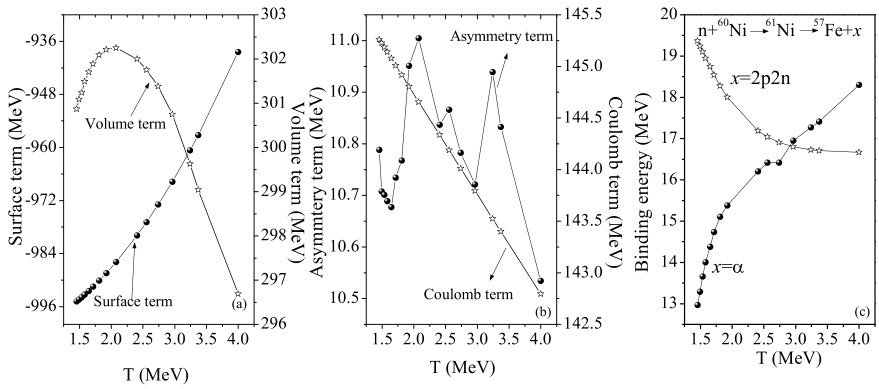

Figure 4.5: The ingredients of liquid drop model(LDM) potential terms are plotted as a function of excitation energy (temperature) of the compound nucleus ^{61}Ni*. Here (a) shows the surface term and volume term and (b) shows the variation of asymmetry and Coulomb component and (c) shows the comparative binding energy for α and $2p2n$-emission.

terms involved in liquid drop potential term (V_{LDM}) (defined in Chapter-2) for the compound nucleus ^{61}Ni* formed in fast neutron induced reaction n+^{60}Ni are plotted as a function of compound nucleus temperature T (in MeV) in Fig.4.5. The surface energy term and the volume energy term are plotted in Fig.4.5(a) while asymmetry energy term and the Coulomb energy term are plotted in Fig.4.5(b). It is clear that all these terms are highly sensitive towards the temperature of the compound nucleus and this temperature dependance enters through the temperature-dependent coefficients involved in these terms [15, 24]. Thus, the total binding energy of the fragment, which is the sum of all these terms gets modified significantly with respect to temperature there by, suggesting that the compound nucleus follows different decay paths at different beam energies.

In addition to this, the binding energies of α-cluster and $2p2n$-multinucleon system are plotted as a function of compound nucleus temperature T (MeV) in Fig.4.5(c) where solid spheres represent the binding energy values of α-cluster and stars represent those for $2p2n$-multinucleon system. It may be noted that binding energy of α-cluster increases with rise in temperature of the compound nucleus while that of $2p2n$ shows an opposite behavior and decrease with rise in temperature. It has been observed that within the Seeger's semi-empirical formula [25], the mass dependency vanishes for proton and neutron A=1 and for the case of neutron the contribution due to Coulomb term also becomes zero as Z=0. Due to this, the LDM potential term gets reduced to the following form for a proton (A=1, Z=1):

$$V_{LDM}(A,Z,T) = \alpha(T) + \beta(T) + 3(\gamma(T) - \eta(T)) + \frac{1}{r_0(T)} \times (1 - 0.7636 - \frac{2.29}{r_0(T)}) + \delta(T) \tag{4.1}$$

while for a neutron it becomes;

$$V_{LDM}(A,Z,T) = \alpha(T) + \beta(T) + 3(\gamma(T) - \eta(T)) + \delta(T) \tag{4.2}$$

It is clear that the V_{LDM} term comprises of the Seeger's constants only. Since these constants $\alpha(T), \beta(T), \gamma(T), \eta(T)$ and $\delta(T)$ decrease with temperature, consequently, V_{LDM} also decreases with temperature for the case of proton and neutron. And, since, the binding energies of $2p2n$-multinucleon system is calculated from the binding energies of proton and neutron as given by equation;

$$B(A_2 = xnyp) = xB_n + yB_p - a_c A_L^{5/3} \tag{4.3}$$

so the binding energy of $2p2n$-multinucleon system shows the trend as in Fig.4.5(c).

From Fig. 4.5(c), it can be seen that at around T=2.9 MeV a transition is seen and below this point, the magnitude of binding energy of α-cluster is lesser than that of $2p2n$ while above this point, the trend is reverted. This binding energy goes as an input in the fragmentation potential defined in Chapter-2, and lower the value of fragmentation potential higher is the probability of decay of that cluster. Therefore, the lower binding energy values of α-cluster for T<2.9 MeV make it more probable to form the preferred emission channel of the compound nucleus ^{61}Ni* while for T>2.9MeV the trend gets reverted and one gets $2p2n$ multinucleon emission from ^{61}Ni*.

(d) Effect of mass of decaying compound nucleus on fragmentation path:

Finally, the effect of mass (and charge) of the compound nucleus on the relative emission of α and $2p2n$ emission is seen and for this, the excitation functions of three more systems formed in fast neutron induced reactions, lying in different mass regions (from light to heavy) are exercised. The other three reactions studied in addition to this reaction are n+^{16}O, n+^{48}Ti and n+^{92}Mo forming the compound nuclear systems ^{17}O*, ^{49}Ti* and ^{93}Mo* over the incident beam energy of E_{beam}=1-100 MeV. In Fig.4.6, the cross-sections for α or $2p2n$-emission from compound nuclear systems ^{17}O*, ^{49}Ti*, ^{61}Ni* and ^{93}Mo* are plotted as a function of incident beam energy (E_{beam}). Here solid circles represent the experimental data while solid and dotted lines represent the DCM calculated cross-sections for α and $2p2n$-emission respectively. For the compound nuclear systems ^{49}Ti*, ^{61}Ni* and ^{93}Mo*, the DCM based calculations find reasonable agreement with the experimental data. The calculations are carried out by using the non-sticking approach in moment of inertia. It is clear that at lower beam energies, the DCM calculated cross-sections for α-cluster match with the experimental data at lower energies while the cross-sections for $2p2n$-emission are very less in magnitude as compared to α-cluster. And at higher incident energies, the trend seems to be reverted where $2p2n$-emission cross-sections follow the experimental cross-sections (as shown by dotted line) but the cross-sections for α-cluster (shown solid lines) falls to much smaller values. It may be noted that the cross-sections for α and $2p2n$ emission are calculated at same values of neck-length parameter ΔR (and respective values of ℓ_{max}) for each energy. Another point to be noted here is that for all the three systems the point where the trend of binding energies reverses its magnitude for α and $2p2n$-emission lies approx. at T$\simeq$2.9

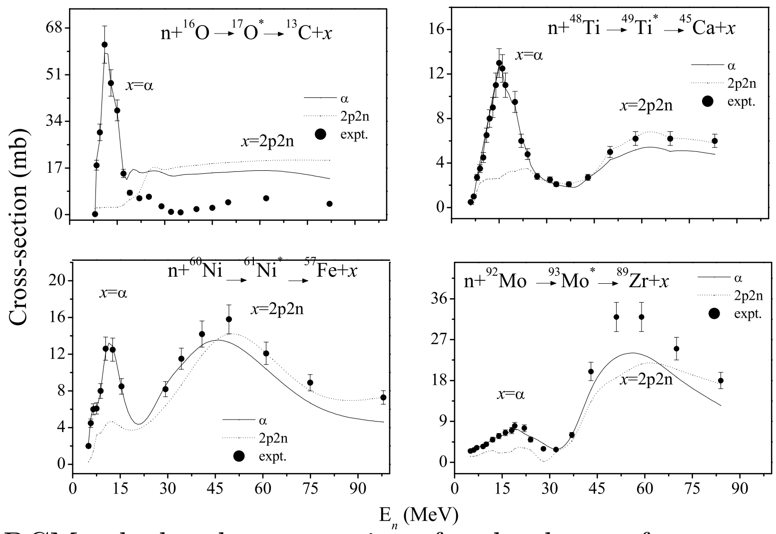

Figure 4.6: DCM calculated cross-sections for the decay of compound nuclei ^{17}O*, ^{49}Ti*, ^{61}Ni* and ^{93}Mo* formed in fast neutron induced reactions via x-emission (where x=α and $2p2n$ cluster) as a function of center of mass energy $E_{c.m.}$ along with experimental data (shown by filled cirlces).

MeV although it corresponds to different $E_{c.m.}$ (and E_{beam}) values. In summary, the emergence of $2p2n$-multinucleon emission at expense of α-emission is visible in all the chosen reactions.

For the compound system ^{17}O*, the experimental data could be addressed for beam energies $E_{beam}\leq$ 15 MeV, but for higher energies, the DCM calculations overestimate the data by few orders although a transition is seen for α and $2p2n$-emission at around $E_{beam}\sim$25MeV. The inadequacy in the addressal of the data may be due to the excessive small mass of compound system ^{17}O*. It is relevant to mention that DCM works out in coordinates of mass asymmetry and the collective clusterization involves the distribution of preformation probability amongst all the possible decay channels emerging from a compound system. In other words, collective clusterization means all the possible out-going fragments like light particles, intermediate mass fragments, heavy mass fragments and fission fragments are treated on equal footing. Mass asymmetry (η_A) (η_A=$\frac{A_T-A_P}{A_T+A_P}$) for each decay mode from a particular compound nucleus is calculated for α-emission channel and its values come out to be 0.529, 0.836, 0.868 and 0.913 respectively for ^{17}O*, ^{49}Ti*, ^{61}Ni* and ^{93}Mo* systems.

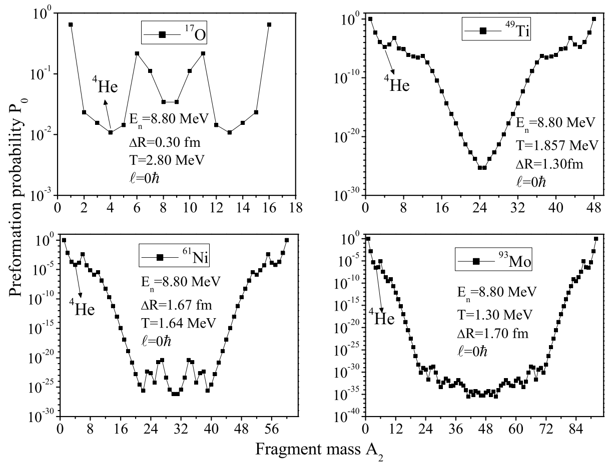

Figure 4.7: Preformation probability P_0 plotted for the decay of compound nuclear systems $^{17}O^*$, $^{43}Ti^*$, $^{61}Ni^*$ and $^{93}Mo^*$ minimized in mass coordinates at the common center of mass energy $E_{c.m.}$=8.80 MeV and ℓ=0$\hbar$.

Due to small mass of compound system and relatively much lower mass asymmetry, the dynamics of the lightest system $^{17}O^*$, do not go in accordance with the dynamics of other heavier systems i.e. $^{49}Ti^*$, $^{61}Ni^*$ and $^{93}Mo^*$. This point is further clarified in Fig.4.7, where the preformation probability P_0 for the decay of all the aforementioned compound systems is plotted as a function of fragment mass number A_i at common incident beam energy E_{beam}=8.80 MeV and ℓ=0$\hbar$. It is clear from the Fig.4.7 that the distribution of preformation probability P_0 shows somewhat similar trend for three heavy mass compound nuclear systems $^{49}Ti^*$, $^{61}Ni^*$ and $^{93}Mo^*$ except for the case of $^{17}O^*$. Fig.4.7(b), (c) and (d) shows that at ℓ=0$\hbar$, the preformation probability P_0 for light particles lie close to 1 making them more probable towards the decay while for heavier fragments i.e. for fragments lying around $\frac{A}{2} \pm 20$, the value of preformation probability is negligibly small and lie close to 0 which signifies that their possibility to form the decay path is negligibly small at lower ℓ-values. While for the case of $^{17}O^*$ (Fig. 4.7(a)), due to very small value of A, the preformation probability of fragments with A_2=1,6 and 7 (plus their complementary fragments) lie close to 1 and for fragments with A_2=2,3,4,5(plus their complementary fragments) have relatively lesser magnitude which means, the decay of compound nucleus $^{17}O^*$ does not opt for one decay path at a particular value of $E_{c.m.}$ and angular momentum (ℓ) and hence the dynamics of decay of $^{17}O^*$ does not seem to be adequately explained within the opted methodology. Also, experimentally, it is observed that the probability for an α-cluster emission depends upon the mass (and charge) of the compound nucleus from which it is emitted. The lightest system $^{17}O^*$, shows the maximum probability of α-emission while the same goes on decreasing with increase in mass number of the compound system. This observation is further analyzed using the preformation probability curve and it is found that magnitude of P_0 for α-cluster emission is maximum for the lightest compound nuclear system $^{17}O^*$ and least for heaviest nucleus $^{93}Mo^*$. This shows that the preformation behavior is in accordance with the experimental observations.

4.2.2 Analysis of n-evaporation from the nuclei formed via p-induced reactions

In this sub-section, the reactions p+^{76}Ge→^{77}As*, p+^{82}Se→^{83}Br* and p+^{85}Rb→^{86}Sr* using proton beams as projectiles are studied within the framework of DCM at incident beam energy range 1-5 MeV and the analysis of the decay of the three, thus formed compound systems- ^{77}As*, ^{83}Br* and ^{86}Sr* is carried out at common beam energy E_{beam}∼3.6 MeV (and hence common center of mass energy $E_{c.m.}$∼3.55 MeV). The proton beam of same energy i.e. E_{beam}=3.6 MeV when incident upon targets of different masses (^{76}Ge, ^{82}Se and ^{85}Rb) produce compound systems having different excitation temperatures i.e. T=1.24 MeV, 1.20 MeV and 1.27 MeV for ^{77}As*, ^{83}Br* and ^{86}Sr* respectively. This is because of the distribution of energy of incoming beam amongst different number of nucleons in the chosen systems.

(a) Role of deformations: As already stated that the calculations are done for spherical choice of fragmentation and in order to study the relevance of deforma-

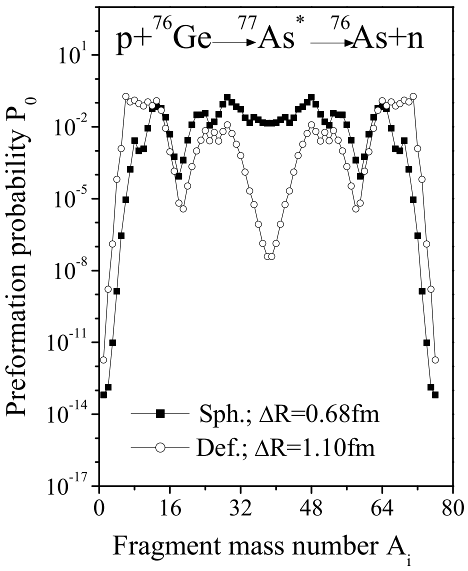

Figure 4.8: Preformation probability P_0 as a function of fragment mass number A_i for the decay of ^{77}As* at ℓ_{max}-value using spherical as well as β_2-deformed approach at E$c.m.$=3.55 MeV.

tion in p-induced reactions forming the compound systems, the calculations are also done by including β_2-deformations of the decaying fragments for the decay of ^{77}As*. Note that by including β_2-deformations, higher values of neck-length parameter and consequently lower values of angular momentum are required for addressal of the experimental data and the fitted values of neck length ΔR. It may be noted that we are always interested in those fragments in the decay channel which possess lower magnitudes of fragmentation potential and since due to absence of contribution from the Coulomb term, the magnitude of fragmentation potential for n-evaporation is always lesser as compared to other light charged particles. Therefore the presence of neutrons (1n) and neutron clusters (2n, 3n or 4n) hinders the emission of proton (1p), proton clusters (2p,3p) or other charged particles (^{2}H, ^{3}H, ^{4}He and so on) when the compound system chooses to decay via light particle evaporation (with $A_2 \leq 4$). Interestingly, it has been found that when β_2-deformations are included in the decay of the compound system ^{77}As*, a strong competition between the minimization of n and p is observed. That means, the fragment corresponding to mass number A_2=1 is identified to be 1n for lower ℓ-states while 1p for higher ℓ-states. This may be attributed to the large oblate (negative) β_2-deformation of the daughter nucleus ^{76}As (β_2=-0.258) formed with n-evaporation as compared to the deformations of ^{76}Ge (β_2=0.143) resulted from p-evaporation. Hence, due to such large β_2-values, the deformations play an important role for fragment minimization in the decay of ^{77}As*. For proper addressal of the data for 1n-evaporation, the probability of the presence of 1p in the decay channel is taken to be 0 in the collective clusterization process. The effect of deformations is analyzed via Fig.4.8, where preformation probability P_0 is plotted as a function of fragment mass number A_i for the decay of ^{77}As* using spherical as well as β_2-deformed fragmentation approaches. The curve is plotted at the respective best-fit values of neck-length parameter ΔR for both the choices of fragmentation. It is evident that the inclusion of deformations affects not only the magnitude but also the structure of the decay profile of ^{77}As* as shown in Fig. 4.8. For the system ^{77}As*; the decay profile adopts a more asymmetric structure after inclusion of deformation effects, which is seen to be relatively symmetric for the spherical case. This result is consistent with the one observed in the decay of CN formed in n-induced reaction where the decaying system adopts more asymmetric path when deformations of the decaying fragments are considered while the decay path remains relatively symmetric for spherical fragments. Along with this, the secondary asymmetric shoulders lying in IMF region also become broader and more probable towards the decay in the deformed case as compared to spherical approach. The structural variations in the region A_2=6-13 is due to the oblate deformations (negative β_2-deformations) of the fragments while that in region A_2=23-31 is due to prolate deformations (positive β_2-deformations). The decreased magnitude in region A_2=31-38 is due to the collective clusterization effect, that is, by including deformations, there is an enhancement in the preformation probability of some fragments at the expense of the lowered preformation probabilities of the remaining fragments.

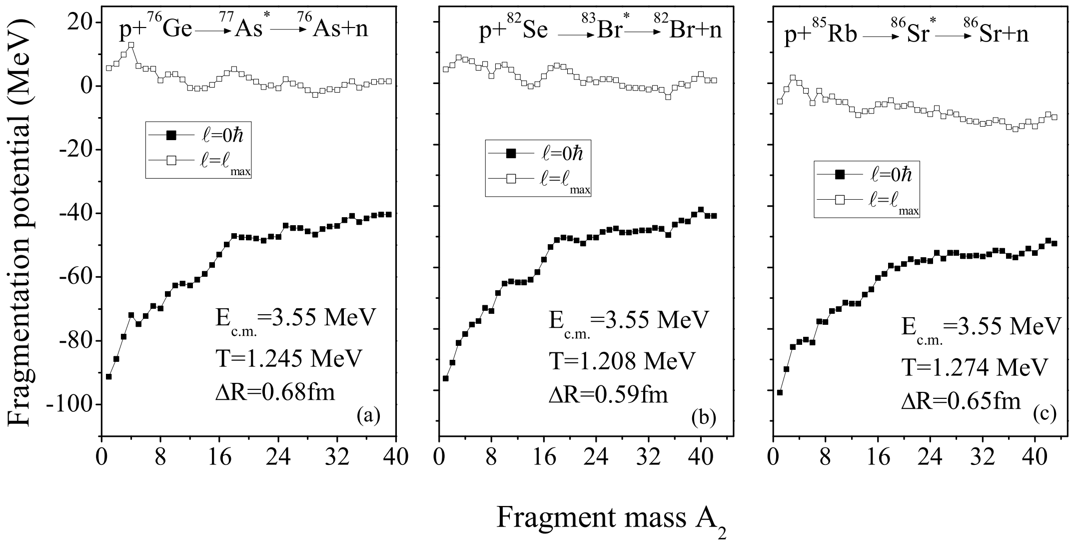

Figure 4.9: Fragmentation potential plotted as a function of fragment mass A_2 for the decay of (a)^{77}As*, (b)^{83}Br* and (c)^{86}Sr* at common incident beam energy E_{beam}=3.6 MeV at ℓ=0$\hbar$ and ℓ_{max}.

(b) Role of angular momentum: To analyze the role of angular momentum for the decay of these compound nuclei formed in p-induced reaction, the fragmentation potential for the decay of (a)^{77}As*, (b)^{83}Br* and (c)^{86}Sr* is plotted as function of fragment mass A_2 at common beam energy $E_{beam}\sim$3.6 MeV and at the best-fit values of neck-length parameter ΔR in Fig. 4.9. Note that the graph is plotted at the two extreme values of angular momentum ℓ=0$\hbar$ and ℓ_{max} using spherical fragmentation approach. The analysis of this figure shows that all the three compound systems prefer to decay via neutron or light particle evaporation at lower values of angular momentum (ℓ=0$\hbar$) supported by their lowered magnitude of fragmentation potential as compared to the intermediate and heavy fragments(IMF and HMF/ff). As the values of angular momentum are increased, a change in the decay structure is observed and eventually the magnitude of fragmentation potential for intermediate and heavier fragments(IMF and HMF/ff) gets lowered, there by suggesting the possibility of their emission at higher ℓ-values. Similar results were obtained in n-induced reactions forming ^{61}Ni* compound nucleus.

Also, the comparative analysis of the decay structure of the three chosen system reveals that the magnitude of fragmentation potential for n-evaporation is -91.26,

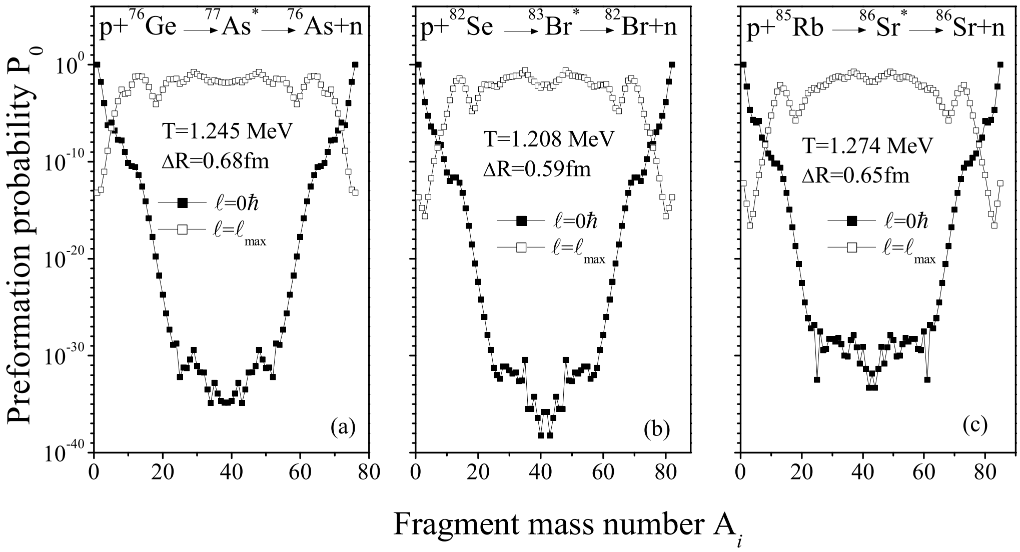

Figure 4.10: Preformation probability as a function of fragment mass number A_i for the decay of (a)^{77}As*, (b)^{83}Br* and (c)^{86}Sr* at common beam energy E_{beam}~3.6 MeV for the best-fit values of neck-length parameter ΔR and ℓ=0$\hbar$ and ℓ_{max}.

-96.17 and -100.73 MeV for ^{77}As*, ^{83}Br* and ^{86}Sr* respectively showing that for the same beam energy E_{beam}=3.6 MeV, the neutron is most probable to evaporate from the heaviest system (^{86}Sr*) amongst the systems under investigation because of the least magnitude of fragmentation potential. Along with this, some structural variations are also observed in intermediate and heavy mass region which are further clarified from the preformation probability (P_0) curve as shown in Fig.4.10. In Fig. 4.10, the preformation probability P_0 is plotted as a function of fragment mass number (A_i) for the decay of (a)^{77}As*, (b)^{83}Br* and (c)^{86}Sr* at common beam energy E_{beam}~3.6 MeV (and hence common center of mass energy $E_{c.m.}$~3.5 MeV) at ℓ=0$\hbar$ and ℓ_{max}. All the three systems have broad symmetric fragment distribution along with asymmetric peaks emerging in intermediate mass region. In other words, at ℓ_{max} there is a strong competition between the emergence of IMF along with HMF/ff with n-evaporation channel channel of the compound systems and this result is consistent for all the three chosen systems. Since DCM calculated cross-sections

Table 4.2: DCM based cross-section for 1n-decay channel for the three chosen systems-^{77}As*, ^{83}Br* and ^{86}Sr* at $E_{c.m.}$=3.55 MeV. Also, the summed up cross-sections calculated for other decay channels A_2=1-4, A_2=5-20 (IMF) and A_2=21-A/2 (HMF/ff) are also tabulated.

cross-sections(mb)	^{77}As*	^{83}Br*	^{86}Sr*
$\sigma_{DCM}(1n)$	39.60	12.70	9.05
$\sigma_{DCM}(A_2 = 1-4)$	42.10	20.50	9.17
$\sigma_{DCM}(IMF)$	33.20	8.00	3.78
$\sigma_{DCM}(HMF/ff)$	1.63	0.62	0.94

are the product of the probability of preformation P_0 of a decaying fragment and its probability of tunnelling through the barrier P, so even though these fragments lying in IMF and HMF/ff region have high preformation probabilities at ℓ_{max} but there net contribution towards the decay cross-sections is still less as compared to n-evaporation cross-sections due to lowered barrier penetrability values. The DCM calculated cross-sections for all the possible exit channels i.e. 1n, LP, IMF or HMF/ff channel of these compound systems are tabulated in Table-4.2 and it may be noted that the cross-sections for IMF and HMF/ff are predicted at the same values of ΔR as used for the fitting of n-evaporation cross-sections. Also, it should be noted that amongst the light particle evaporation i.e. the emission of fragments with A_2=1-4, the major contribution is from 1n-evaporation only and the IMF includes fragments with A_2=5-20 while HMF/ff includes fragments with A_2=21 to A/2. Also, the DCM has been employed to calculate the n-evaporation cross-sections from the three compound systems-^{77}As*, ^{83}Br* and ^{86}Sr* formed in reactions p+^{76}Ge→^{77}As*, p+^{82}Se→^{83}Br* and p+^{85}Rb→^{86}Sr* lying over a low energy range of E_{beam}=1-5 MeV and the experimentally available data is nicely addressed at all the reported energies. The calculations are done for spherical choice of fragmentation and the data is fitted by optimizing the neck-length parameter, ΔR. The optimized values of ΔR along with the DCM calculated cross-sections are tabulated in Table-4.3 and 4.4 and the same are plotted in Fig.4.11 as a function of center of mass energy $E_{c.m.}$ for all the

Table 4.3: The DCM calculated cross sections for the decays ^{77}As*→^{76}As+n and ^{83}Br*→^{82}Br+n obtained for the spherical choice of fragmentation along with experimental data. The optimized values of ΔR are also tabulated at ℓ=ℓ_{max}.

S. No.			^{77}As*→^{76}As+n		
	$E_{c.m.}$ (MeV)	T (MeV)	ΔR (fm)	σ^{DCM} (mb)	σ^{expt} (mb)
1	1.97	1.16	0.090	0.40	0.37±0.04
2	2.36	1.18	0.300	2.01	1.90±0.20
3	2.76	1.20	0.450	6.190	6.80±0.80
4	3.15	1.22	0.572	16.40	17±2
5	3.55	1.24	0.680	38.60	40±4
6	3.94	1.26	0.742	60.90	62±7
7	4.34	1.28	0.837	124.00	115±13
			^{83}Br*→^{82}Br+n		
1	1.86	1.12	-0.15	6.11×10^{-2}	7.98×10^{-2}±0.014
2	2.16	1.14	0.11	0.40	0.367±0.03
3	2.45	1.15	0.263	1.29	1.14±0.10
4	2.75	1.17	0.370	3.06	3.33±0.31
5	3.05	1.18	0.470	6.81	6.77±0.6
6	3.35	1.19	0.552	12.7	12.44±1.2
7	3.55	1.20	0.595	18.5	19.32±2.25

three systems. It is clear that for all the three systems, the values of ΔR increases with increase in center of mass energy $E_{c.m.}$ and the value of ΔR≤1 fm.

Moving further, the effect of angular momentum is also analyzed from Fig. 4.12 where the fragmentation potential for the decay of ^{77}As* is plotted as a function of fragment mass A_2 at $E_{c.m.}$=3.55 MeV for β_2-deformed approach at different values of angular momentum lying between ℓ=0$\hbar$ to ℓ_{max}. This figure helps us to clarify that at a particular angular momentum value, the light particles have lower magnitude

Table 4.4: The DCM calculated cross sections for the decay $^{86}Sr^{*}\rightarrow^{85}Sr+n$ obtained for the spherical choice of fragmentation along with experimental data. The optimized values of ΔR are also tabulated at $\ell=\ell_{max}$.

S. No.	$^{86}Sr^{*}\rightarrow^{85}Sr+n$				
	$E_{c.m.}$	T	ΔR	σ^{DCM}	σ^{expt}
	(MeV)	(MeV)	(fm)	(mb)	(mb)
1	2.15	1.21	0.10	5.46×10^{-2}	$5.80\times10^{-2}\pm0.006$
2	2.55	1.23	0.34	0.51	0.56±0.05
3	2.75	1.24	0.44	1.36	1.20±0.12
4	3.15	1.25	0.55	3.60	3.77±0.35
5	3.55	1.27	0.65	9.05	9.60±0.87
6	3.95	1.29	0.73	19.40	19.65±1.82

of fragmentation potential and above that ℓ-value, there is a switching in the decay structure there by lowering the magnitude of fragmentation potential for fragments lying in IMF and HMF/ff region. This behavior is consistent for all the three systems but is shown only for the lightest system $^{77}As^{*}$ here to avoid repetition.

(c)Role of level density parameter: In view of the experimental results in ref. to [19], the effect of variation of level density parameter (LDP) on the DCM calculated results has also been analyzed by varying the magnitude of level density parameter and by using mass dependent level density parameter $a(A)$ defined in Chapter-2. It may be noted that in DCM usually the value of level density is taken to be $a = 9$ for compound systems lying in medium and heavy mass region while a=11 for superheavy mass region. For investigating the effect of level density and to check the sensitivity of DCM calculated cross-sections towards the choice of level density, the value of level density is taken in range $a = 6$ to $a = 10$ and its effect on the n-evaporation cross-sections is observed. Noting that while using the various values of level density parameter, the value of neck-length is fixed at ΔR=1.10 fm within deformed approach for the decay of $^{77}As^{*}$. This is the optimized value of ΔR at

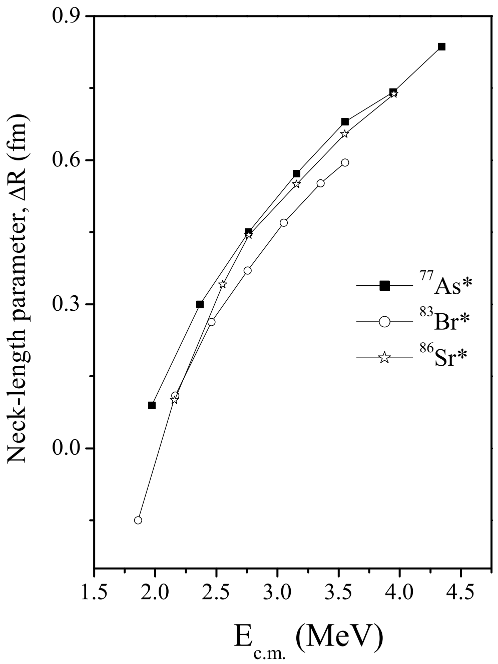

Figure 4.11: Neck-length parameter ΔR plotted as a function of $E_{c.m.}$ for all the three systems-^{77}As*, ^{83}Br* and ^{86}Sr*.

which the experimental data is fitted for 1n-decay channel i.e. n-evaporation by using a=9. It has been found that the DCM calculated cross-sections for n-evaporation in present case are not sensitive to the variation of level density up to a certain value of angular momentum. Hence, we may conclude that the DCM calculated results for n-evaporation are insensitive to the choice of level density at lower values of angular momentum, which support the dominance of neutrons in decay channel. Further, for higher ℓ-values, i.e. where the IMF and HMF/ff fragments start competing in the decay channel, the cross-sections seem to be affected by the variation in level density. Thus, the IMF or HMF/ff cross-sections may be sensitive to the choice of level density parameter as they appear in the decay channel at higher ℓ-values. Also, it has been observed that if level density is taken as a=8 and 10, there is still not much effect on the n-evaporation cross-sections, but opting a=6 and 7 influences the cross-sections significantly.

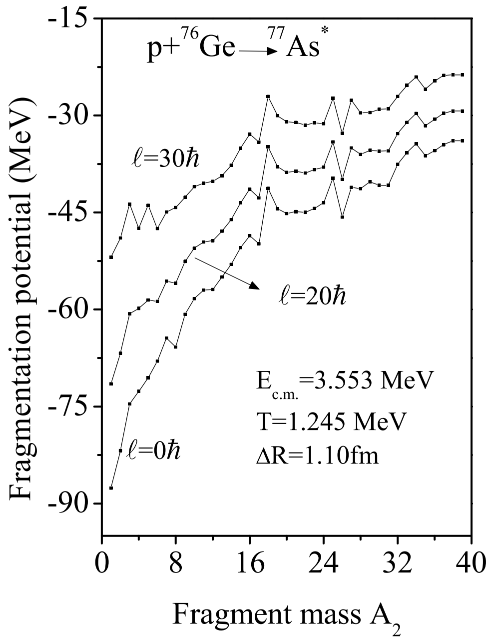

Figure 4.12: Fragmentation potential as a function of fragment mass A_2 for the decay of ^{77}As* at various values of ℓ at $E_{c.m.}$=3.55 MeV for β_2-deformed approach.

4.3 Conclusions

This chapter presents the decay analysis of compound nucleus ^{61}Ni* formed in n-induced reaction over an incident beam energy range of E_n=1-100MeV within the framework of Dynamical Cluster-decay Model (DCM). Due to lighter mass of ^{61}Ni*, the system chooses to decay via light particle evaporation, unlike, the compound nucleus ^{240}Np*, which decays via fission channel due to its heavy mass and is discussed in the previous chapter. For appropriate addressal of the experimental data the I_S limits are replaced with I_{NS} and the cross-sections for the α-cluster emission or $2p2n$-multinucleon emission are estimated by opting appropriate values of neck-length parameter. It has been observed that the emission of light charged particles is favored at lower angular momentum values and the compound nucleus ^{61}Ni* undergoes near symmetric fragmentation at lower center of mass energies $E_{c.m.}$ and with increase in $E_{c.m.}$, the structure becomes highly asymmetric. Also, with increase in energy, the magnitude of fragmentation potential of α-cluster increases and hence the probability of its decay decreases. The transmutation of α-emission at lower energies and $2p2n$-emission at higher energies is explained on the basis of temperature dependence of the binding energies used in DCM calculations. The binding energy of α-cluster as emitted from ^{61}Ni* possesses lower magnitude at lower temperature (T in MeV) as compared to that of $2p2n$-cluster. While above a particular temperature T=2.9 MeV, the trend gets reverted with $2p2n$-cluster having lower values of binding energies. Also, the effect of mass (and charge) of the compound nucleus on α and $2p2n$-multinucleon emission is analyzed and comparative analysis is done for the decay of various compound nuclei having mass ranging from light to intermediate mass region.

Further, the decay analysis of compound systems- ^{77}As*, ^{83}Br* and ^{86}Sr* formed in p-induced reactions is also carried out at common beam energy $E_{beam}\sim$3.6 MeV. The compound systems fall in light mass region and decays via n-evaporation. The experimentally available data is addressed adequately by using the collective clusterization technique of DCM and initially the calculations are done using spherical fragmentation approach. The role of deformations is also analyzed and for this purpose, the preformation profile of spherical fragmentation is compared with that after inclusion of β_2-deformations. Lastly, the DCM calculated cross-sections are analyzed for their dependence on the nuclear level density (LDP) parameter by varying the value of LDP from 6-10 and by including mass-dependence in it. The results show that the DCM calculated cross-sections for n-evaporation are insensitive to the choice of level density up to those ℓ-values up to which the n-evaporation dominates in decay channel, and as soon as the ℓ-values are increased further, due to competing heavier fragments, a variation in the cross-sections can be observed. Similar results are obtained when mass-dependent level density parameters are used.

After decay analysis of light mass compound nuclei formed in n and p-induced reactions, this thesis proceeds through the analysis of mechanisms involved in the decay of compound nuclei formed in α and heavy-ion induced reactions. The observations and results recorded from the investigation of the decay profiles of the compound systems formed in these above-mentioned reaction channels are elaborated in the next chapter.

Bibliography

[1] C. Bhatia *et al.*, Phys. Rev. C **91** 064604 (2015).

[2] R. K. Gupta, M. Bansal, Int. Rev. Phys. (I. RE. Phys.) 5, 74, (2011); M. K. Sharma, S. Kanwar, G. Sawhney, R. K. Gupta, Phys. Rev. C **85**, 064602 (2011).

[3] M. K. Sharma, S. Kanwar, G. Sawhney, R. K. Gupta, W. Greiner, J. Phys. G:Nucl. Part. Phys. **38**, 055104 (2011), R. K. Gupta, in *Clusters in Nuclei*, ed. by C. Beck, Lecture notes in Physics 818, Vol I (Springer, Berlin, 2010) p.223.

[4] R. K. Gupta, S. K. Arun, R. Kumar, Niyti, Int. Rev. Phys. (I. RE. Phys.) **2**, 369 (2008).

[5] Niyti, R. K. Gupta, W. Greiner, J. Phys. G:Nucl. Part. Phys. **37**,115103 (2010), R. K. Gupta, Niyti, M. Manhas, W. Greiner, J. Phys. G:Nucl. Part. Phys. **36**, 115105 (2009).

[6] R. K. Gupta, Niyti, M. Manhas, S. Hofmann, W. Greiner, Int. J. Mod. Phys. E, **18**, 601 (2009).

[7] K. Sandhu, M. K. Sharma, R. K. Gupta, Phys. Rev. C **85**, 024604 (2012).

[8] M. Kaur, R. Kumar, M. K. Sharma, Phys. Rev. C **85**, 014609 (2012), G. Kaur, M. K. Sharma, Nucl. Phys. A **884**, 36 (2012).

[9] S. S. Malik, and R. K. Gupta, Phys. Rev. C **39** 1992 (1989).

[10] R. K. Gupta, and W. Greiner, Int. J. Mod. Phys. E **3** 335 (1994).

[11] G. Sawhney, M. K. Sharma, and R. K. Gupta, Phys. Rev. C **83** 064610 (2011).

[12] N. Fotiades et al. Phys. Rev. C **91** (2015) 064614.

[13] P. Möller, J. R. Nix, W. D. Myers, and W. J. Swiatecki, At. Data Nucl. Data Tables, **59** 185 (1995).

[14] G. Kaur, N. Grover, K. Sandhu, and M. K. Sharma, Nucl. Phys. A **927** 232-248 (2014); R. K. Gupta, Niyti, M. Manhas, and W. Greiner, J.Phys.G; Nucl. Part. Phys. **36** 115105 (2009).

[15] B. B. Singh, M. K. Sharma, R. K. Gupta, Phys. Rev. C **77**, 054613 (2008).

[16] D. Dashdorj et. al., Nucl. Sci. Eng., **157**, 65 (2007).

[17] P. E. Garrett et. al., Phys. Rev. C **62**, 054608 (2000).

[18] R. O. Nelson, M. B. Chadwick, A. Michaudon and P. G. Young, Nucl. Sci. Eng. **138**, 105 (2001).

[19] G. G. Kiss, Gy. Gyürke, Z. Elekes, Zs. Fülöp, and E. Somorjai, Phys. Rev. C **76**, 055807 (2007).

[20] Gy. Gyürke, Zs. Fülöp, and E. Somorjai, Phys. Rev. C **68**, 055803 (2003).

[21] G. G. Kiss, T. Rauscher, Gy Gyürke, A. Simon, Zs. Fülöp, and E. Somorjai, PRL **101**, 191101 (2008).

[22] J. P. Lestone, Phys. Rev. C **52**, 2 (1995).

[23] R. K. Gupta et al., Phys. Rev. C **68**, 014610 (2003); R. K. Gupta et al., Phys. Rev. C **71**, 014601 (2005).

[24] N. J. Davidson, S. S. Hsiao, J. Markram, H. G. Miller, and Y. Tzeng, Nucl. Phys. A **570**, 61c (1994).

[25] P. A. Seeger, Nucl. Phys. **25**, 1 (1961).

Chapter 5

Decay of nuclei formed in α and heavy ion induced reactions

5.1 Introduction

The previous chapters demonstrate the dynamics of n and p induced reactions and the fragmentation structures, preformation profiles and the study of other important parameters like moment of inertia, deformations and orientations and so on helps us to extract a better description of the dynamics governing these reactions. Such reactions form highly asymmetric incoming channels and the use of such lighter projectiles possess a greater significance in the field of nuclear reactions. With an idea to expand the understanding of nuclear reaction mechanism, an effort is made to extend this analysis to the decay dynamics of the compound systems formed in reactions where projectiles heavier than n and p are used. Hence, this chapter covers the role of use of α and heavy-ions as projectiles and subsequently, their effect on fragmentation profile, barrier penetrating probability and barrier characteristics, barrier height V_B, barrier position R_B is investigated. As already stated that the use of heavier projectile alters the asymmetry of the incoming channel and as a result, E_{beam} converting in to $E_{c.m.}$ gets attuned. Hence, for the use of α and heavy-ions, $E_{c.m.}$ is less than E_{beam}.

In order to pursue the above-mentioned aim; the dynamics of α and heavy-ion induced reactions is explored using the DCM [1]- [8] which is reformulation of PCM [9–11] and the decay of the compound systems ^{117}Sb*, ^{145}Pm* and ^{191}Ir* formed in α-induced reactions [12–14] and $^{98,104}_{48}Cd^*$ formed in ^{40}Ca-induced reactions [15] are studied. The decay mechanisms of compound nuclei ^{117}Sb*, ^{145}Pm* and ^{191}Ir* are investigated for n-evaporation [12–14] over an incident beam energy $E_\alpha \sim$ 10 to 15 MeV and the same are addressed within collective clusterization technique of DCM. It is to be noted here that the corresponding center of mass energy $E_{c.m.}$ lies in range $\sim$ 9.5 to 14.5 MeV. The calculations are done via spherical fragmentation approach and the cross-sections, addressed by optimizing the neck-length parameter(ΔR) find nice agreement with the available experimental data. The present study also deals with amalgamation of same projectile with different targets forming compound nuclei with different masses and important information regarding the reaction mechanism can be extracted from the structural variations that are incorporated into the decay profiles of these compound systems. In addition to this, the comparative studies of ^{117}Sb*, ^{145}Pm* and ^{191}Ir* is important from the view point that these systems possess different neutron-proton asymmetry values where I=(N-Z)/A. The lightest system ^{117}Sb* has the least value of neutron-proton asymmetry (I=0.128) while its value increases for heavier systems ^{145}Pm*(I=0.158) and ^{191}Ir* (I=0.193). Thus, an effort is made to see the influence of neutron-proton asymmetry dependence in Bulk constant α (used in semi-empirical mass formula [16]) as well as the radius term R_i used in present calculations. The neutron-proton asymmetry dependence in α is included in ref. to [17] while the neutron-proton asymmetry dependent radius term R_i is taken from [18]. It may be noted that the values of the Bulk constant α are refitted according to experimental binding energies [19]. If the experimental data is not available then theoretical estimates of Moller et al. [20] are used and the new set of alphas which comes out to be neutron-proton asymmetry dependent (I-dependent), are obtained by rescaling the conventional set of Bulk constant (α) used in DCM by a factor of (1-kI^2), with I=(N-Z)/A and value of k is taken from [17]. As expected, the effect of inclusion of I-dependence vanishes for N=Z. The refitting is done at T=0 MeV and subsequently, the temperature dependence is included as per [21]. It is relevant to mention here that similar efforts have been done previously [4] where α were refitted only but no neutron-proton asymmetry dependence was included. The choice of radius term R_i plays an eminent role in the reaction dynamics as it alters the various potential terms (V_P, V_C and V_ℓ) etc. discussed in Chapter-2. The inclusion of neutron-proton asymmetry dependence in radius terms alters the magnitude of the potential terms and consequently its effect can be seen on the preformation factor estimated by solving Schrodinger equation in mass-asymmetry η-coordinate. Moreover it would be of interest to understand the effect of neutron-proton asymmetry dependent radius on the asymmetric (light particle emission) as well as symmetric (HMF or fission) decay fragments of the compound systems, as different decaying fragments possess different neutron-proton asymmetry values. In addition to this, the use of R(I) also alters the barrier characteristics- barrier height (V_B) and barrier position (R_B) which in turn affect the position of first turning point R_a and consequently its effect on the barrier penetrability provide useful insights.

While for the ^{40}Ca-induced reactions, the decay of compound nuclei ^{98,104}Cd* is carried out over an energy spread E_{beam}=105-155 MeV with deformations and orientation [20] effects included in it and the experimental cross-sections for particle evaporation are fitted adequately by optimizing the neck-length parameter(ΔR) of the model. The corresponding $E_{c.m.}$=65-85 MeV which is very less as compared to beam energy E_{beam}. The model uses the Prox-1977 potential and sticking limits of moment of inertia (I_S) with inclusions of quadrupole deformations (β_2) and optimum orientations (θ_i) [20]. The comparative analysis of decay profiles of isotopic compound nuclei ^{98,104}Cd* is worked out by introducing angular momentum and temperature effects and the relevant information is extracted from the fragmentation structures and barrier characteristics.

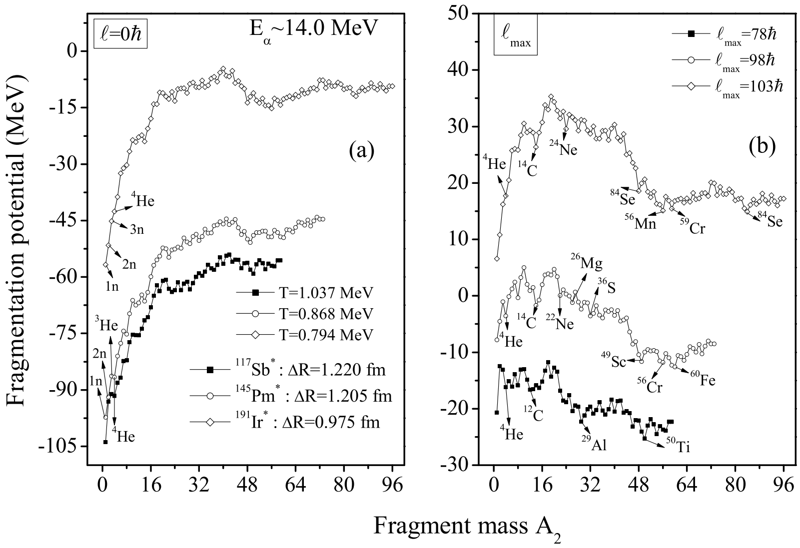

Figure 5.1: Fragmentation potential plotted as a function of fragment mass A_2 for the decay of ^{117}Sb*, ^{145}Pm* and ^{191}Ir* at common incident beam energy $E_\alpha\sim$14.0 MeV at (a)ℓ=0$\hbar$ and (b)$\ell=\ell_{max}$.

This chapter is categorized in two parts where the calculations and results are presented in section-5.2 while the conclusions are drawn in section-5.3

5.2 Calculations and Results

This section is segregated in two parts. The first part i.e. sub-section-5.2.1 presents the dynamics involved in α-induced reactions while the second part i.e. sub-section-5.2.2 presents the studies involving the dynamics of heavy-ion induced reactions i.e. ^{40}Ca-induced reactions.

5.2.1 Fragmentation analysis of α-induced reactions using clusterization approach

(a) Effect of mass of compound nucleus on the fragmentation structure:

In Fig.5.1, the fragmentation potential minimized in mass/charge coordinates is plotted against fragment mass A_2 for the three compound systems ^{117}Sb*, ^{145}Pm* and ^{191}Ir* at common incident beam energy $E_\alpha\sim$14.0 MeV at (a) ℓ=0$\hbar$ and (b)

ℓ=ℓ_{max}. The graph is plotted for the spherical choice of fragmentation at respective best-fit values of neck-length parameter ΔR. The CN excitation energy is related to mass of CN and T as: $E_{CN} = \frac{A_{CN}}{9}T^2 - T$. For same beam energy E_α, the compound nucleus excitation energy (equivalently the temperature T) of the compound nucleus (CN) decreases with increasing mass of the compound nucleus (A_{CN}) and the values of T are 1.037 MeV, 0.868 MeV and 0.795 MeV respectively for ^{117}Sb*, ^{145}Pm* and ^{191}Ir* nuclei. From the fragmentation profiles, it has been observed that with increase in mass of the compound system, the magnitude of fragmentation potential shifts to higher values and this result is consistent for both ℓ-values (ℓ=0$\hbar$ and ℓ=ℓ_{max}). This observation seems to suggest that the heaviest CN i.e. ^{191}Ir* possesses the highest magnitude of fragmentation potential. This can be justified from the fact that for decay of any CN; A_{CN}→A_1+A_2, if the mass of the lighter fragment is fixed i.e. A_2 is fixed, the mass asymmetry of the decay channel increases with increase in A_{CN}. Hence, the mass and charge of the heavier fragment A_1 and Z_1 increases and consequently a significant increase in the values of Coulomb potential (V_C) is observed. Although for each decay channel with fixed A_2, the proximity potential (V_P) and binding energy (BE) also show variation in their magnitudes but these variations are suppressed by the increment in Coulomb potential V_C thereby altering the overall fragmentation potential V (=V_C+V_P+V_ℓ+BE) significantly. For example, if A_2(=40) is fixed for the decay of each CN i.e. for decay channels ^{117}Sb*→^{77}As+^{40}Ar, ^{145}Pm*→^{105}Tc+^{40}Ar and ^{191}Ir*→^{151}Pm+^{40}S, the mass asymmetry increases from 0.3 to 0.4 to 0.5 because the corresponding heavier fragment is ^{77}As, ^{105}Tc and ^{151}Pm as A_{CN} increases from 117 to 145 to 191 and the V_C values for these decays are 97.968 MeV, 119.793 MeV and 139.678 MeV. Hence, the observed increment in magnitude of fragmentation potential with increase in A_{CN} is attributed to increment in V_C values due to increased mass asymmetry of the decay channel. Another point of observation here is that, at ℓ=0$\hbar$ (Fig.5.1(a)) the structure of the curve suggests that light particles (LP) with A_2=1-4 possess lower

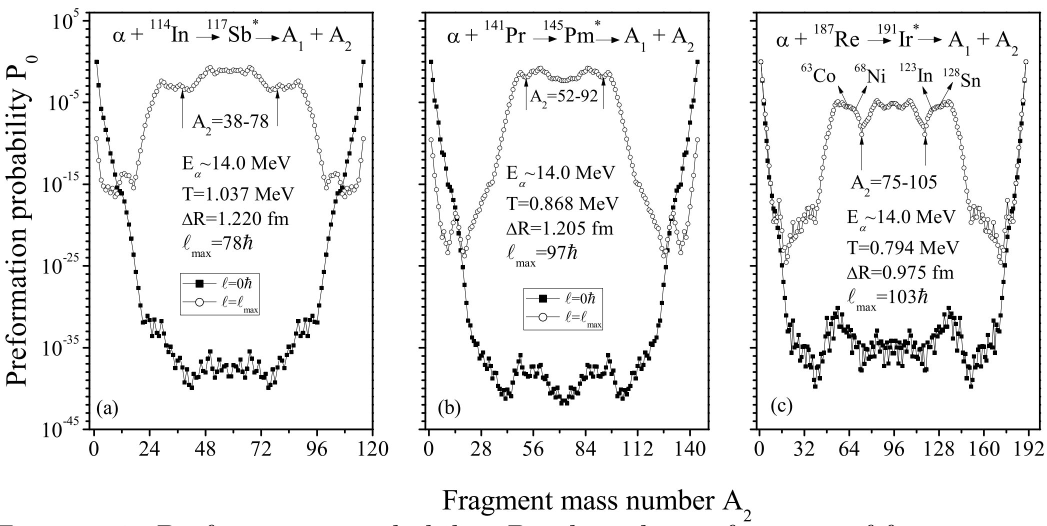

Figure 5.2: Preformation probability P_0 plotted as a function of fragment mass A_2 for the decay of (a)^{117}Sb*, (b)^{145}Pm* and (c)^{191}Ir* at common incident beam energy E_α~14.0 MeV at ℓ=0$\hbar$ and $\ell=\ell_{max}$.

magnitudes of fragmentation potential for all the three compound nuclei and are consequently emitted from the compound systems with higher probability as compared to other heavier fragments. This means that all the three compound systems are equally likely to decay via light particle emission (n-emission) at lower angular momentum states. However, at high ℓ-values, the increased centrifugal energy reinforces the CN to undergo HMF or fission decay and this is supported by the presence of valleys with lowered magnitude of fragmentation potential in HMF/fission region. This result is consistent with that observed for n and p-induced reactions.

This is further investigated from Fig.5.2 where preformation probability P_0 is plotted for all the three compound systems (a)^{117}Sb*, (b)^{145}Pm* and (c)^{191}Ir* at fixed value of incident beam energy, E_α~14.0 MeV at ℓ=0$\hbar$ and $\ell=\ell_{max}$. It is clear that at ℓ=0$\hbar$, the LPs have high values of preformation probabilities while at $\ell=\ell_{max}$, the fragments corresponding to the heavier mass and fission region show an elevation in the preformation profile. It has also been observed that the decay of lightest CN ^{117}Sb* is symmetric in nature where fragments lying in fission region ($\frac{A_{CN}}{2}\pm 20$) have higher P_0 values. A shoulder lying in HMF region (plus complementary fragments) with elevated P_0 values as compared to lighter fragments is seen but its contribution

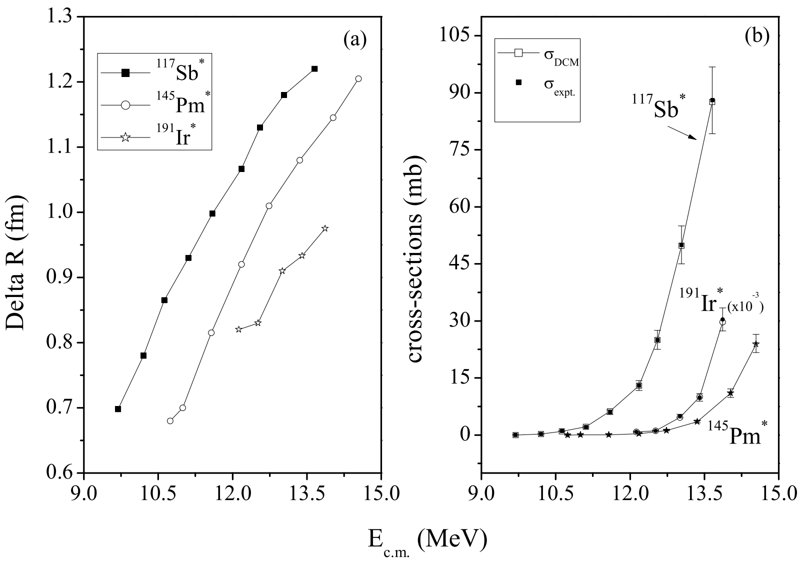

Figure 5.3: (a)The neck-length parameter ΔR and (b)DCM calculated cross-sections along with experimentally available data plotted as a function of $E_{c.m.}$ for all the three systems $^{117}Sb^*$, $^{145}Pm^*$ and $^{191}Ir^*$.

is negligible as compared to fission fragments, with ratio $\frac{P_0(ff)}{P_0(HMF)}\simeq$62.8. As we move towards heavier mass of the CN i.e. $^{145}Pm^*$; the fragmentation becomes relatively asymmetric and the HMF shoulder has raised P_0 values as compared to that in $^{117}Sb^*$ with $\frac{P_0(ff)}{P_0(HMF)}\simeq$6.98. Similarly, for the heaviest CN $^{191}Ir^*$, in addition to the symmetric peak in fission region, a strong maxima in HMF region (plus in complementary region), forming asymmetric shoulders is observed. The contribution of these HMF fragments becomes comparable to that of fission fragments, being slightly lesser in magnitude making the ratio $\frac{P_0(ff)}{P_0(HMF)}\simeq$1.26. The raised asymmetric shoulder for heaviest system may be attributed to the structural effects which seem to be arising due to the closed shell configuration of ^{68}Ni and ^{128}Sn (with Z=28 and 50). Hence one may conclude that, for α-induced reactions forming CN of heavier masses, the contribution due to the fragments lying in adjoining HMF region gets enhanced. The corresponding fission region is marked in the figure for each system and HMF region corresponds to the fragments with $A_2\geq$21 up to fission region.

For the three compound systems $^{117}Sb^*$, $^{145}Pm^*$ and $^{191}Ir^*$ formed in α-induced

Table 5.1: The DCM calculated cross sections for the reactions ^{117}Sb$^{*}\rightarrow^{116}$Sb+n obtained for the spherical choice of fragmentation along with experimental data. The optimized values of ΔR are also tabulated.

S. No.	$E_{c.m.}$ (MeV)	T (MeV)	ΔR (fm)	σ^{DCM} (mb)	σ^{expt} (mb)
1	9.689	0.870	0.698	0.07	0.07±0.02
2	10.203	0.893	0.780	0.26	0.27±0.04
3	10.623	0.911	0.865	0.99	1.00±0.08
4	11.106	0.933	0.930	2.20	2.10±0.20
5	11.592	0.953	0.998	5.85	6.00±0.50
6	12.180	0.978	1.067	13.01	13.00±1.00
7	12.555	0.993	1.130	24.56	25.00±2.00
8	13.038	1.012	1.180	49.78	50.00±4.00
9	13.658	1.037	1.220	78.89	88.00±6.00

reactions, the data for n-evaporation is duly addressed by varying neck-length parameter (ΔR). The values of the fitted ΔR are plotted as a function of $E_{c.m.}$ for the chosen cases in Fig. 5.3(a) and it is observed that the ΔR increases almost linearly as a function of center of mass energy. Similar pattern is observed for all the compound nuclei. In addition to this for a fixed value of $E_{c.m.}$, the data for n-evaporation requires higher neck values for the lightest system ^{117}Sb*, while the heaviest system ^{191}Ir* demands the lowest value of ΔR. So at fixed $E_{c.m.}$ values the ΔR decreases with increase in A and according to a linear fit with negative slope follows the equation: $\Delta R = 1.58 - 0.003A$. This equation may be used to estimate the ΔR values for some other cases governing α-induced dynamics and hence be used to predict the corresponding n-evaporation cross-sections. The DCM calculated cross-sections for the reactions ^{117}Sb$^{*}\rightarrow^{116}$Sb+n, ^{145}Pm$^{*}\rightarrow^{144}$Pm+n and ^{191}Ir$^{*}\rightarrow^{190}$Ir+n are plotted as a function of $E_{c.m.}$ in Fig. 5.3(b) and are presented in Tables 5.1-5.2 along with

Table 5.2: The DCM calculated cross sections for the reactions ^{145}Pm*→^{144}Pm+n and ^{191}Ir*→^{190}Ir+n obtained for the spherical choice of fragmentation along with experimental data. The optimized values of ΔR are also tabulated.

S. No.	$E_{c.m.}$ (MeV)	T (MeV)	ΔR (fm)	σ^{DCM} (μb)	σ^{expt} (μb)
1	10.742	0.714	0.680	0.007	0.008±0.001
2	10.998	0.724	0.700	0.013	0.015±0.001
3	11.570	0.749	0.815	0.069	0.07±0.02
4	12.182	0.775	0.920	0.347	0.35±0.07
5	12.736	0.798	1.010	1.188	1.20±0.24
6	13.357	0.822	1.080	3.556	3.58±0.68
7	14.028	0.848	1.145	11.000	11.02±1.37

S. No.	$E_{c.m.}$ (MeV)	T (MeV)	ΔR (fm)	σ^{DCM} (μb)	σ^{expt} (μb)
1	12.124	0.741	0.820	0.837	0.850±0.19
2	12.517	0.753	0.830	1.090	1.130±0.29
3	13.007	0.769	0.910	4.990	4.970±1.12
4	13.402	0.782	0.933	1.010	9.900±2.00
5	13.866	0.794	0.975	29.876	30.400±8.80

experimental data and other parameters of DCM.

(b) Role of deformations: It has been discussed in previous chapters that deformations of the decaying fragments play a crucial role in deciding the fragmentation structures of the compound nuclei irrespective of the fact whether the compound nucleus is formed using n or p as a projectile. Following this, it would be interesting to analyze the role of deformations in regards to α-induced reactions and the same has been explored in Fig. 5.4, where P_0 is plotted as a function of frag-

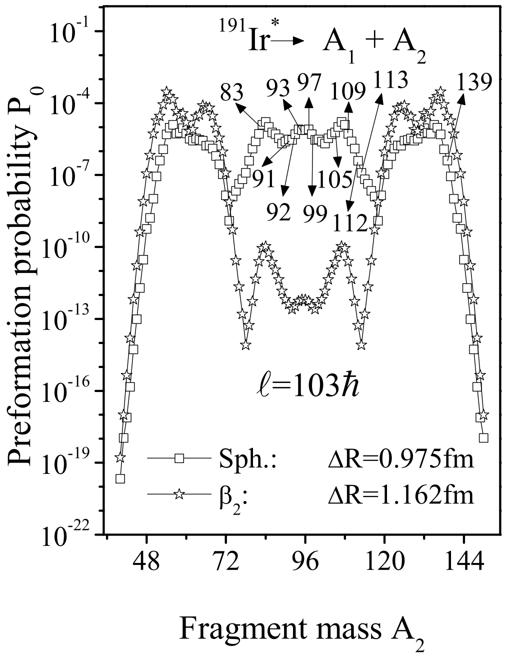

Figure 5.4: Preformation probability P_0 plotted as a function of fragment mass A_2 for the decay of $^{191}Ir^*$ at E_α~14.0 MeV using spherical as well as deformed approach.

ment mass A_2 for the decay of $^{191}Ir^*$ at ℓ=ℓ_{max} for spherical as well as β_2-deformed choices of fragmentation. A significant change in structure is observed by inclusion of $\beta_2$deformations and this figure infers that the spherical approach suggests that the decay channel of the CN consists primarily of symmetric fission fragments (with A_2=80-110) with some contribution of asymmetric shoulders in HMF region having A_2=52-70 (and complementary region). On the other hand, when deformations are included, the decay pattern becomes highly asymmetric with maximum contribution from A_2=52-70 fragments. This result seem to be in agreement with that obtained in case of decay of CN formed in n and p-induced reactions. In that case also, the inclusion of deformations alters the fragmentation structure, there by making it asymmetric in nature, which otherwise was symmetric for spherical approach. The experimental data that is available for the fission of $^{191}Ir^*$ [22] suggests that the fission channel of the compound system comprises of fragments having masses A_2=80-110 which lie on the symmetric peak (SP). This means that the spherical approach gives much better agreement with [22], so the calculations are done for spherical choice of fragmentation only and the deformation effects are not included in further analysis.

(c) Role of neutron-proton asymmetry in parameters: Further analysis of the compound systems ^{117}Sb*, ^{145}Pm* and ^{191}Ir* is done on the basis of their different neutron-proton asymmetry values (0.128, 0.158 and 0.193 respectively). Firstly, the effect of neutron-proton asymmetry dependence is included in terms of Bulk constant α of liquid drop energies used in DCM and its effect on fragmentation potential is worked out. The effect of using neutron-proton asymmetry dependent Bulk constant is analyzed from the corresponding fragmentation potentials for all the three compound systems but is graphically shown for ^{191}Ir* only as it possesses highest I-values. In Fig.5.5, the fragmentation potential for the decay of ^{191}Ir* is plotted at $\ell = 0\hbar$ for the choice of both Bulk constants i.e. the conventionally used α_{DCM}(T) (solid line) and the refitted neutron-proton asymmetry-dependent α_{asym}(T) (dotted line). Since the calculations deal with excited state decays, so the temperature dependence is incorporated in ref. to [21]. From the figure it is clear that no significant effect on overall structure is observed for the use of α_{asym}(T), while minor variations in magnitude for individual fragments are found. Those decaying fragments which have high neutron-proton asymmetry values are observed to be affected more. Note that for the lighter systems, ^{145}Pm* and ^{117}Sb* similar observations are made (not shown here), but with slightly lesser difference in magnitudes due to their lower neutron-proton asymmetry values. So, it is clear that although the overall structure is not affected yet significant variations in magnitude of fragmentation potential for individual fragments can be seen by using neutron-proton asymmetry-dependent α_{asym}(T). Moreover, the refitting of α is done according to experimental binding energies so the variations in magnitude may also be observed due to inclusion of temperature dependence in the Bulk constant. This means that the inclusion of neutron-proton asymmetry dependence in the values of Bulk con-

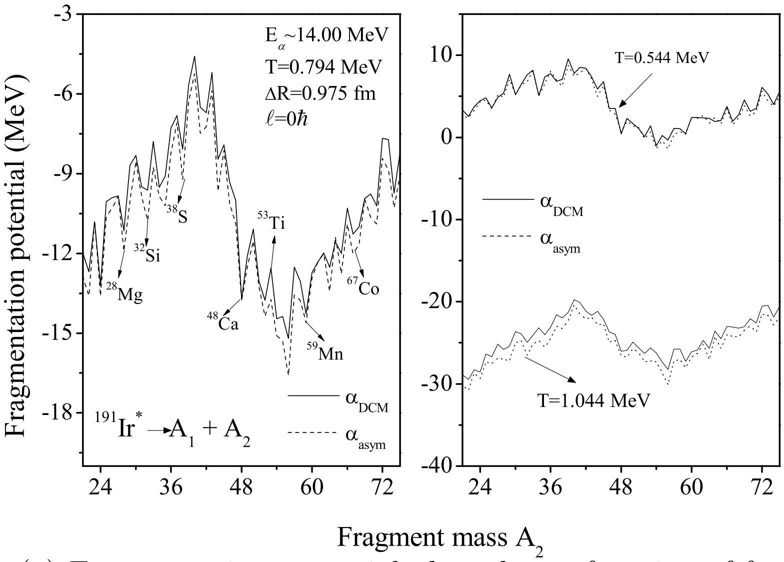

Figure 5.5: (a) Fragmentation potential plotted as a function of fragment mass for the decay of ^{191}Ir* at incident beam energy $E_\alpha \sim 14.0$ MeV using α_{DCM} and newly refitted neutron-proton asymmetry dependent α_{asym} (b) same as (a) but for T=0.544 MeV and T=1.044 MeV.

stant α provides new set of α which are varied to different extents by the inclusion of temperature dependence. The effect of temperature on neutron-proton asymmetry dependence is shown in Fig.5.5(b) where the fragmentation potential is plotted at two different temperatures which are $T_{CN}\pm0.25$ MeV i.e. T=0.544 MeV and T=1.044 MeV for the system ^{191}Ir*. Clearly, one can see that the fragmentation structure is affected to a greater extent at higher temperatures.

In addition to this the inclusion of neutron-proton asymmetry in radius term R_i is also analyzed by making use of neutron-proton asymmetry dependent radius as suggested by [18] in DCM based calculations. It is a well known fact that the radius term plays a crucial role in dynamics of nuclear systems, as the various potential terms, vary as a function of R. The comparative effect of use of R(I) is investigated in Fig.5.6 where (a)fragmentation potential, (b)preformation probability P_0 and (c)penetrability P is plotted as a function of fragment mass A_2 for the decay of ^{191}Ir* at $E_\alpha \sim 14.0$ MeV and $\ell = 0\hbar$. It may be noted that the graphs are plotted for both the choices of radius terms R(A) as well as R(I) defined in Chapter-2.

From the analysis of Fig. 5.6(a) and (b) the following points have been ob-

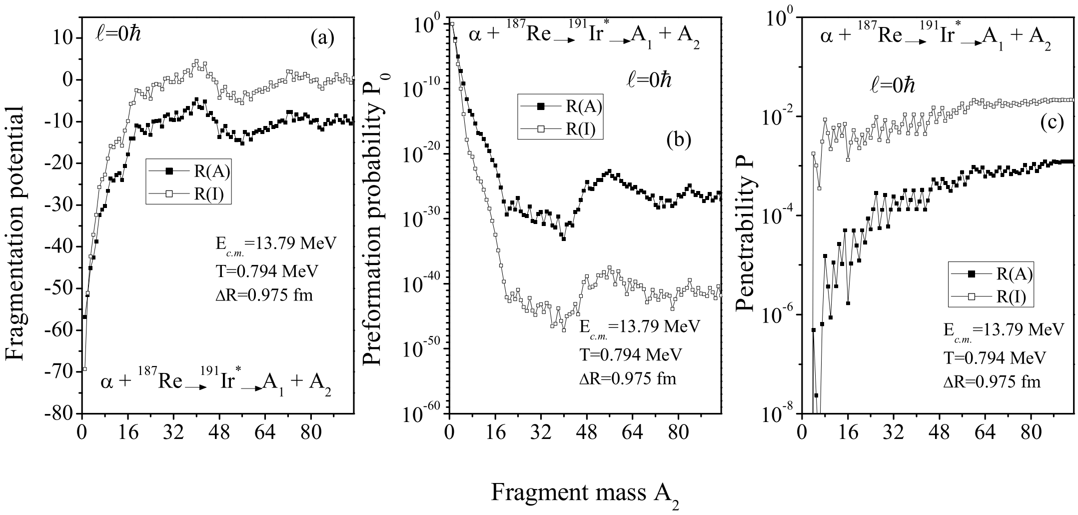

Figure 5.6: (a)Fragmentation potential, (b)Preformation probability P_0 and (c) penetrability P plotted as a function of fragment mass for the decay of the heaviest system $^{191}Ir^*$ by using mass dependent R(A) as well as neutron-proton asymmetry dependent R(I) terms.

served: (i) the replacement of R(A) with R(I) leaves no significant change on the overall decay pattern, while significant variations in magnitude is observed. At same value of ΔR, the magnitude of fragmentation potential is lower for the use of R(A) as compared to that of the use of R(I) which signifies that R(A) seems to provide more adequate option in governing the reaction dynamics of α-induced reactions. Consequently, the magnitude of Preformation factor (P_0) is much higher for the use of radius term R(A) for most of the decaying fragments. All the three compound nuclear systems are found to show similar trends while the heavier system shows greater variation in magnitude due to its high neutron-proton asymmetry as compared to the lighter ones. Here, the graphical variation is shown only for the heaviest system $^{191}Ir^*$.

(ii) Although the overall decay pattern is not affected while a closer look of the curve reveals that the minor variations in the structure of the potential energy surface at individual fragment level can be observed when plotted with the use of R(I) and this is because the different choices of R affect the magnitude of P_0 of decaying fragments to different extents. Obviously, the fragments which have greater neutron-proton asymmetry values are affected to greater extent as compared to others. This means the role of R(I) is appearing at individual fragments level while is silent for overall fragmentation structure.

(iii) In addition to this, the effect of use of R(I) is more pronounced for intermediate mass fragments (IMFs), heavier fragments (HMF) and fission region as compared to light particles (LP). This result is consistent for all the three systems and is attributed to the fact that heavier fragments have greater neutron-proton asymmetry values as compared to evaporation residues or lighter fragments. While specifically for A_2=1, i.e. for the most asymmetric decay the trend seems to be reverted, where magnitude of fragmentation potential is lesser when R(I) is used as compared to that of R(A). It should be noted that for fragment A_2=1, the neutron-proton asymmetry factor(N-Z/A) reduces to 1 and hence the values of R are altered in such a way that it leads to lowering in fragmentation potential.

On the other hand, the penetration probability P seems to show an opposite trend. The use of R(I) enhances the penetrability of decaying fragments as compared to R(A) for all the three systems and is shown for the decay of ^{191}Ir* only in Fig.5.6(c). This increase in penetrability values is explained in terms of shift in the first turning point R_a and is justified from scattering plot as shown in Fig.5.7. This figure represents the total scattering potential V (=V_C+V_P+V_ℓ) for the decay ^{191}Ir*$\rightarrow$^{144}La+^{47}Ca, at ℓ_{max} by using R(A) (solid line) and R(I) (dotted line). Note that the mass asymmetry η_A for this reaction is 0.5. It may be noted that the results related to replacement of R(A) with R(I) are consistent for all the compound systems. The role of the neck-length parameter ΔR, emerges very clearly from this figure as it offers modification via barrier lowering parameter ΔV_B=V(R_a)-V_B. The barrier lowering parameter ΔV_B=-2.845 MeV for the use of R(A) and -6.645 MeV for the use of R(I) for this decay channel. This means that the use of R(I) lowers the barrier up to greater extents as compared to the use of R(A), hence makes the penetration of decaying fragments relatively easier. The potential V(R_a) corresponds to the first turning point R_a defined as R_a=R_1+R_2+ΔR and is the effective barrier

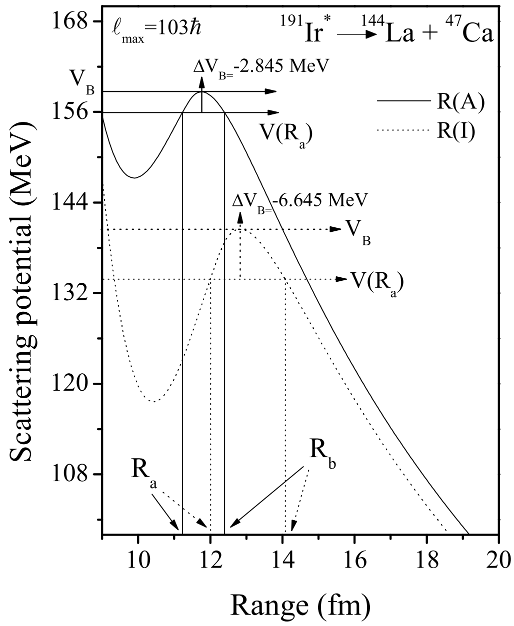

Figure 5.7: Scattering potential plotted as a function of range R(fm) for the decay ^{191}Ir*→^{144}La+^{47}Ca, at ℓ_{max} by using R(A) (solid line) and R(I) (dotted line).

experienced by the decaying fragment(s). The plot clearly signifies that when R(A) is replaced with R(I), the barrier characteristics i.e. barrier height (V_B) and barrier position (R_B) get significantly modified, and consequently a shift in first turning point R_a is observed. For this decay channel, the position of R_a shifts from 11.217 fm to 12.003 fm when R(A) is replaced with R(I). Note that the use of R(I) not only defines different ΔR value as compared to R(A) but it also modifies R_1 and R_2. The shifting of R_a is such that the use of R(I) signifies a higher penetration probability of the decaying fragments. For the decay ^{191}Ir*→^{144}La+^{47}Ca, the position of R_a and R_b are marked for both choice of radius terms and for the use of R(I), the values of R_a and R_b cover more area under the curve, and give enhanced value of penetration probabilities.

It should be noted that the effect of R(I) in the preformation probability comes from the R-dependence of the potentials used in solving the Schrödinger equation whereas the effect of R(I) on penetrability comes in to picture via the shifting of the

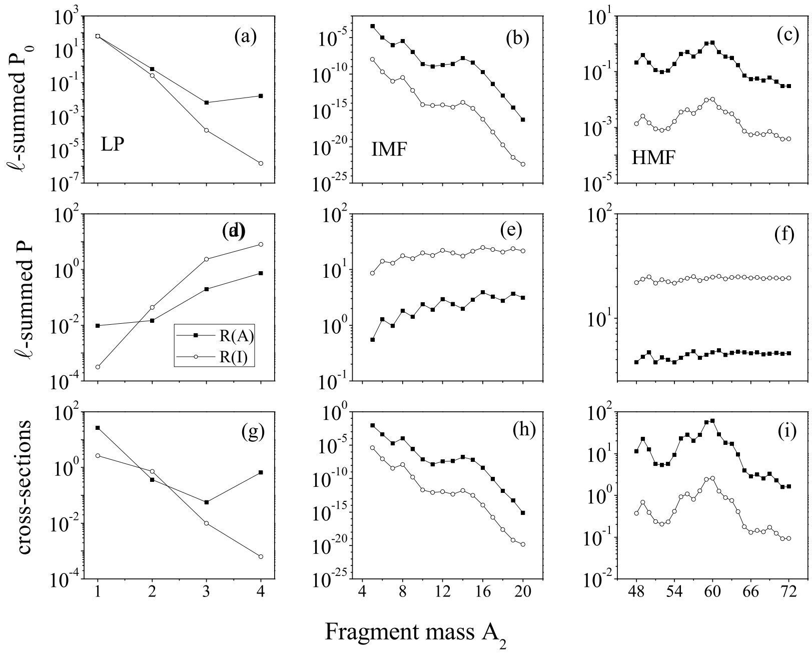

Figure 5.8: ℓ-summed preformation probability P_0, penetrability P and cross-sections plotted for light particles (LP), intermediate mass fragments (IMF) and heavy fragments (HMF) or fission fragments using R(A) and R(I).

first turning point R_a. So the effect of R(I) that appears in the structure of P_0 and P, eventually appears in the cross-sections. To analyze this, the ℓ-summed values of P_0, P and channel cross-sections are plotted as a function of fragment mass A_2 in Fig.5.8 for compound system $^{145}Pm^*$ at $E_\alpha \sim 14.0$ MeV respectively for LP[(a), (d), (g)], IMF[(b), (e), (h)] and HMF or fission fragments [(c), (f), (i)]. Note that the curves are plotted by the use of both radius terms R(A) (filled squares) and R(I) (hollow circles) and at fixed ΔR value i.e. the best-fit value used with R(A) for comparative purposes. In addition to this, it is an important point to note that the LP, IMF and HMF or fission decay are highly sensitive towards the ℓ-states. So the values of P_0, P and hence cross-sections are plotted by summing over all values up to ℓ_{max}. From Fig.5.8, it is quite clear that the P_0 values show high magnitude with R(A) for all the decay channels-LP, IMF and HMF or fission decay. Also, the magnitude of the difference in P_0 values by the use of R(A) and R(I) increases with increase in the mass of decaying fragments. The effect of replacing R(A) with R(I) is minimal for A_2=1 and maximum for fission decay. Similarly, the ℓ-summed

P values shows that the use of R(I) enhances the P-values for all the fragments except A_2=1 and this increase is maximum for fission decay channel. This may be because for A_2=1 (n-channel here), the scattering potential follows the structure of proximity potential (V_P) and the barrier gets modified in such a way that with the replacement of R(A) with R(I) there is a shift in turning point R_a leading to the decreased barrier penetrability. Since, the DCM based cross-sections depend upon the product of both P_0 and P, and magnitude of decrement in P_0 is greater than increment in P, so the overall reaction cross-sections follows the trend of P_0 values. That means, there is a net decrease in cross-section values when R(A) is replaced with R(I). This is attributed to the fact that the enhancement in P-values is dominated by the corresponding decrement in P_0 values. So, it may be concluded that at a fixed value of ΔR, there is a net decrement in P_0 value and an increment in P-value for each fragment (except A_2=1). But the reaction cross-sections follow the structure and trend of P_0 and show net decrement in cross-sections.

Following this, the next sub-section involves the analysis for the reaction dynamics using heavy-ion as projectiles.

5.2.2 Decay analysis of ^{98,104}Cd* isotopes formed in heavy-ion induced reactions

After analyzing the reaction mechanism of α-induced reactions within the DCM approach in the previous sub-section, the decay of compound systems formed in heavy-ion induced reactions is presented in this sub-section. This sub-section deals with an isotopic analysis of the compound nuclei formed in the two reactions ^{40}Ca+^{58}Ni and ^{40}Ca+^{64}Ni by using collective clusterization approach of DCM.

The role of angular momentum emerges from Fig. 5.9 where the fragmentation potential for the decay of isotopic compound nuclei ^{98,104}Cd* is plotted as a function of fragment mass A_2 at highest energy $E_{c.m.}$=88.20 MeV (approx.) (corresponding beam energy $E_{beam}\sim$150 MeV) and extreme values of angular momentum. It is

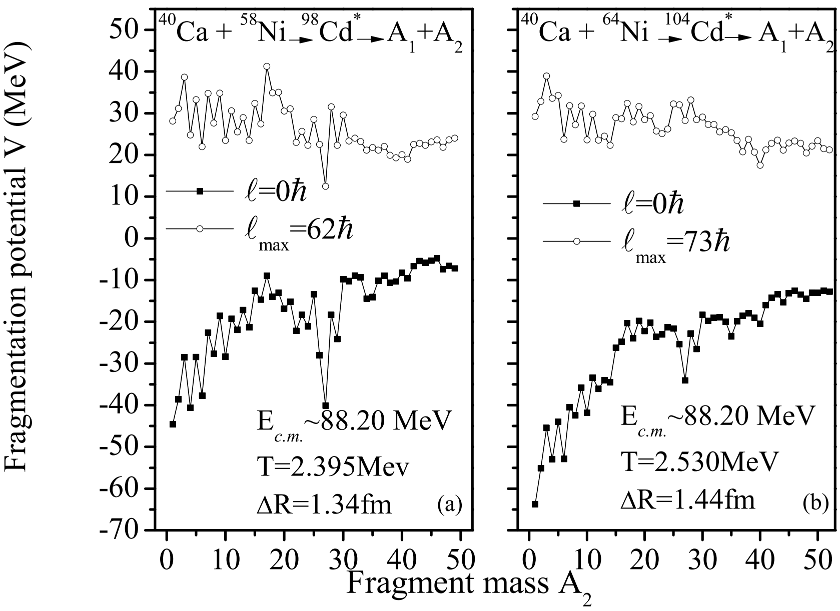

Figure 5.9: Fragmentation potential as a function of fragment mass number (A_2) plotted at E$_{c.m.}$=88.20 MeV (approx.) where part (a) is for the decay of $^{98}_{48}$Cd* nucleus and part (b) is for the decay of $^{104}_{48}$Cd* nucleus.

evident from the lower magnitude of fragmentation potential that the evaporation residues (ERs) are the prominent decaying channel at ℓ=0$\hbar$. While when we transmute towards higher values of angular momentum, the contribution from IMF and fission region also seems evident but we have confinedourselves to ER study only in this paper. This result lies in agreement with the earlier results i.e. for the case of n, p and α-induced reactions also, the compound system adopts the asymmetric decay path emitting light particles at lower ℓ-values and with the increase in ℓ-values, the centrifugal energy increases and IMF and HMF/ff start competing with light particles in the decay channel. Moreover, a comparative study of the graph reveals that the decay pattern for both the CN systems ^{98,104}Cd* is similar but there is a difference in the magnitude of fragmentation potential particularly at ℓ=0$\hbar$ with ^{104}Cd* showing lower magnitude signifying that it is more prone to decay at lower ℓ-values. On the other hand, when we shift to higher ℓ-values, this difference in the magnitudes starts vanishing thereby making them equally probable towards decay process. Other interesting observation in Fig.5.9 is that the α-structure prevails even at high

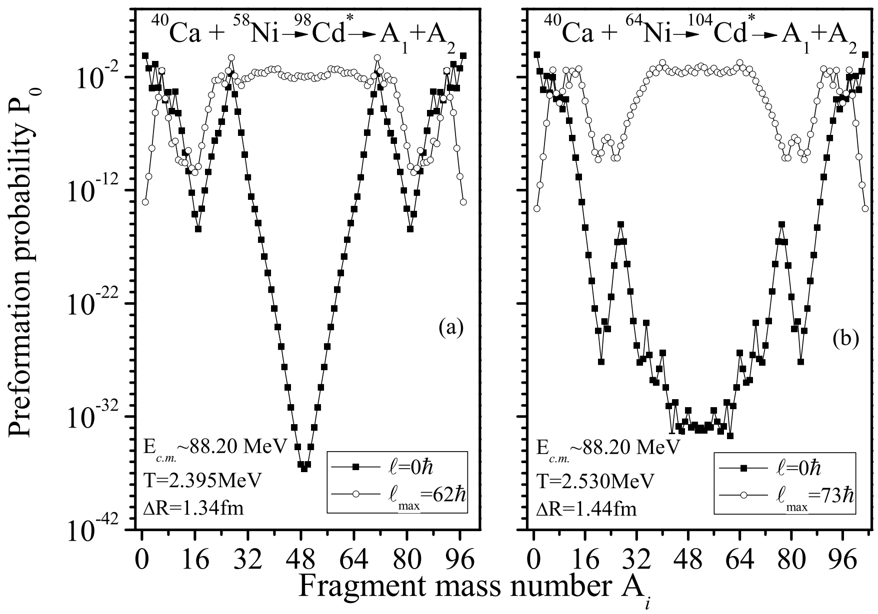

Figure 5.10: Preformation probability as a function of fragment mass number (A_i) plotted at $E_{c.m.}$=88.20 MeV(approx.) (corresponding beam energy E_{beam}∼150 MeV) where part (a) is for the decay of $^{98}_{48}Cd^*$ nucleus and part (b) is for the decay of $^{104}_{48}Cd^*$ nucleus.

excitation energy (T=2.53MeV) and it persists at higher ℓ-values as well. Further, the insight of the decay pattern and structural effects can also be understood from the preformation curve as shown in Fig.5.10. This figure shows the variation of preformation probability of the fragments formed at compound nuclear stage as a function of fragment mass number A_i where (a) part is plotted for $^{98}Cd^*$ and (b) part is plotted for $^{104}Cd^*$ at the highest energy $E_{c.m.}$=88.20 MeV (approx.) (corresponding beam energy E_{beam}∼150 MeV) and respective extreme values of angular momentum. From this figure it may be concluded that the dominant decay mode of $^{98,104}Cd^*$ nuclei is via evaporation residues as they have higher preformation probabilities than other fragments at $\ell=0\hbar$. Secondly, one can infer from Fig.5.10 that the pattern of potential energy surfaces for the decay of both CN systems is similar for lighter fragments although a difference in magnitude is observed for intermediate and heavier mass fragments. Broadly speaking, both the nuclei exhibit near symmetric fission division and larger number of fragments seem to contribute towards

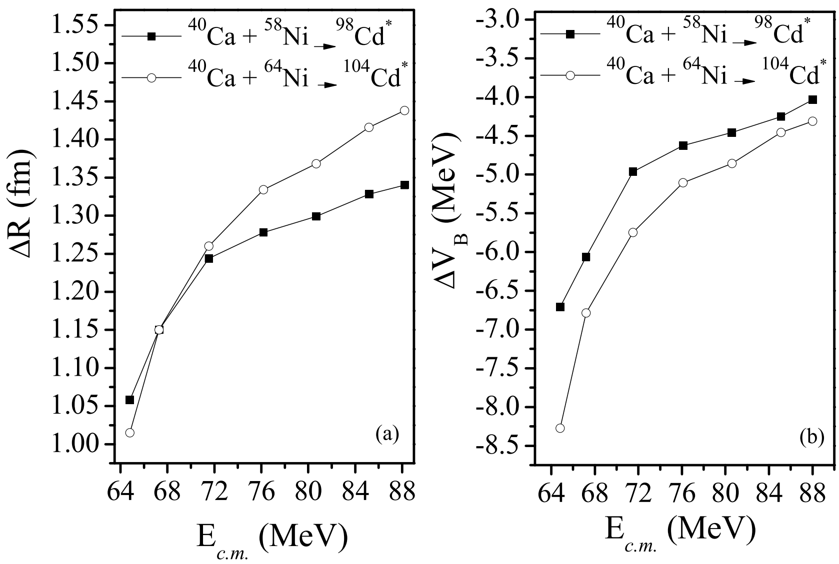

Figure 5.11: (a) Variation of the neck-length parameter ΔR with $E_{c.m.}$ obtained for the best fit to evaporation residue data for the reactions ${}^{40}_{20}Ca$+${}^{58}_{28}Ni$ and ${}^{40}_{20}Ca$+${}^{64}_{28}Ni$ using DCM. (b) same for part(a) but for ΔV$_B$.

fission region of lighter isotope, when compared with heavier one. Some asymmetric peaks in IMF region also indicate the possible emergence of some competing decay channels.

The DCM calculated cross-sections are compared with the experimentally available data for optimized choice of the neck length parameter (ΔR). The experimental cross-sections and DCM calculated cross-sections are shown in Table-5.3 along with other ingredients of DCM. Further, Fig.5.11(a) shows the variation of ΔR as a function of $E_{c.m.}$ and it shows that the value of ΔR increases with increase in $E_{c.m.}$. At higher energies, the cross-sections for ^{104}Cd* are fitted at relatively higher neck-length values as compared to those of ^{98}Cd*. Also, we can see a common energy $E_{c.m.}$=67.3 MeV at which the cross-sections for both compound nuclei ^{98,104}Cd* are achieved at same neck-length values and below this energy, the trend seems to be reverted as ΔR value for the cross-sections of ^{98}Cd* is more than that of ^{104}Cd*. Fig.5.11(b) shows the variation of barrier lowering parameter ΔV$_B$ as a function of $E_{c.m.}$ at ℓ_{max} values corresponding to 1n-evaporation for both reactions ^{40}Ca+^{58}Ni→^{98}Cd* and ^{40}Ca+^{64}Ni→^{104}Cd*. It may be noted that ΔV$_B$is negative and non-zero for both the reactions and its value is observed to be least for higher

Table 5.3: The DCM calculated cross sections for the decay of ${}^{98,104}_{48}$Cd* via evaporation residues in contrast to the experimental data along with other parameters.

S. No.	$E_{c.m.}$	${}^{40}_{20}$Ca+${}^{58}_{28}$Ni→${}^{98}_{48}$Cd*				${}^{40}_{20}$Ca+${}^{64}_{28}$Ni→${}^{104}_{48}$Cd*			
		T	ΔR	σ_{DCM}	$\sigma_{expt.}$	T	ΔR	σ_{DCM}	$\sigma_{expt.}$
		MeV	fm	mb	mb	MeV	fm	mb	mb
1	64.8	1.886	1.058	4.73×10^{-03}	4.43×10^{-03}	2.07	1.015	0.40	0.38
2	67.3	1.940	1.150	0.26	0.22	2.14	1.150	3.60	3.40
3	71.5	2.040	1.244	7.73	7.34	2.22	1.260	12.65	12.77
4	76.2	2.150	1.278	17.20	17.02	2.31	1.334	22.60	22.90
5	80.6	2.250	1.299	24.50	25.01	2.39	1.368	28.20	28.60
6	85.2	2.338	1.328	39.20	39.36	2.48	1.416	42.68	42.13
7	88.2	2.395	1.340	44.80	44.31	2.53	1.438	47.60	47.86

energies which keeps on increasing with decrease in $E_{c.m.}$-value. Thus we can say that a larger barrier modification is needed at lower energies and this behavior is analogous for both the compound nuclear systems. The higher barrier modification at lower energy region facilitate the DCM to address the data at near and below Coulomb barrier region [23].

5.3 Conclusions

This chapter deals with the study of reaction mechanisms involving decay of compound nuclei formed in α and heavy-ion induced reactions using the methodology of DCM. The use of α and heavy ion (^{40}Ca in this case) as projectile decreases the asymmetry of the incoming channel as compared to the use of n and p as projectiles and consequently, the fraction of beam energy converted in to $E_{c.m.}$ gets modified, which in turn may affect the excitations produced in the respective CN formed.

Firstly, the decay analysis of the compound systems ^{117}Sb*, ^{145}Pm* and ^{191}Ir* formed in α-induced reactions is carried out over an incident beam energy E_α=10 to 15 MeV, and secondly the dynamics involved in the decay of ^{98,104}Cd* systems formed in ^{40}Ca-reactions are investigated over a beam energy range of E_{beam}=105-

155 MeV. The compound nuclei formed in the above-mentioned reactions are investigated for light particle evaporation and the DCM calculated cross-sections find nice agreement with the available experimental data. For the CN formed in α-induced reactions, the role of mass of the CN on the fragmentation structure is analyzed along with the role of deformations of the decaying fragments. The role of excitation energy and angular momentum is analyzed for both α as well as heavy-ion induced reactions. In addition to this, the neutron to proton asymmetry effects are also investigated and for this purpose asymmetry dependence is included in bulk constant α (used in LDM term) and the radius expression and the corresponding effect on fragmentation structure is investigated. It is observed that by including asymmetry in Bulk constant α, the overall fragmentation structure remains similar however the magnitude of fragmentation potential changes at individual fragment level. For the use of asymmetry dependent radius, a decrement in preformation probability P_0 and an enhancement in barrier tunnelling probability P is observed while the decay cross-sections follow the trend of P_0 leading to a net decrement in the magnitude.

A comprehensive analysis of the decay dynamics of CN formed in α and heavy-ion induced reactions have been presented in this chapter while that of n and p-induced reactions have been presented in the previous chapters. Now it would be of further interest to extend this analysis to super-heavy mass regime and the same has been explored in the next chapter.

Bibliography

[1] R. K. Gupta, M. Bansal, Int. Rev. Phys. (I. RE. Phys.) 5, 74, (2011); M. K. Sharma, S. Kanwar, G. Sawhney, R. K. Gupta, Phys. Rev. C **85**, 064602 (2011).

[2] M. K. Sharma, S. Kanwar, G. Sawhney, R. K. Gupta, W. Greiner, J. Phys. G:Nucl. Part. Phys. **38**, 055104 (2011), R. K. Gupta, in *Clusters in Nuclei*, ed. by C. Beck, Lecture notes in Physics 818, Vol I (Springer, Berlin, 2010) p.223.

[3] R. K. Gupta, S. K. Arun, R. Kumar, Niyti, Int. Rev. Phys. (I. RE. Phys.) **2**, 369 (2008).

[4] B. B. Singh, M. K. Sharma, R. K. Gupta, Phys. Rev. C **77**, 054613 (2008).

[5] Niyti, R. K. Gupta, W. Greiner, J. Phys. G:Nucl. Part. Phys. **37**,115103 (2010), R. K. Gupta, Niyti, M. Manhas, W. Greiner, J. Phys. G:Nucl. Part. Phys. **36**, 115105 (2009).

[6] R. K. Gupta, Niyti, M. Manhas, S. Hofmann, W. Greiner, Int. J. Mod. Phys. E, **18**, 601 (2009).

[7] K. Sandhu, M. K. Sharma, R. K. Gupta, Phys. Rev. C **85**, 024604 (2012).

[8] M. Kaur, R. Kumar, M. K. Sharma, Phys. Rev. C **85**, 014609 (2012), G. Kaur, M. K. Sharma, Nucl. Phys. A **884**, 36 (2012).

[9] S. S. Malik, and R. K. Gupta, Phys. Rev. C **39** 1992 (1989).

[10] R. K. Gupta, and W. Greiner, Int. J. Mod. Phys. E **3** 335 (1994).

[11] G. Sawhney, M. K. Sharma, and R. K. Gupta, Phys. Rev. C **83** 064610 (2011).

[12] C. Yalçin et al., Phys. Rev. C **79**, 065801 (2009).

[13] A. Sauwerin et al., Phys. Rev. C **84**, 045808 (2011).

[14] P. Scholz et al., Phys. Rev. C **90**, 065807 (2014).

[15] D. Bourgin *et al.*, Phys. Rev. C **90** (2014) 044610.

[16] P. A. Seeger, Nucl. Phys. 25, 1 (1961).

[17] W. Myers, and W. J. Swiatecki, Nucl. Phys. **81** 1 (1996).

[18] B. Nerlo-Pomorska, and K. Pomorski, Z. Phys. A **348** 169-172 (1994).

[19] G. Audi, A. H. Wapstra and C. Thiboult, Nucl. Phys. A **729** 337 (2003).

[20] P. Möller, J. R. Nix, W. D. Myers, and W. J. Swiatecki, At. Data Nucl. Data Tables, **59**, 185 (1995).

[21] N. J. Davidson, S. S. Hsiao, J. Markram, H. G. Miller, and Y. Tzeng, Nucl. Phys. A **570**, 61c (1994).

[22] E. F. Neuzil et al., J. Inorg. Nucl. Chem. **30** 1161-1167 (1968).

[23] G. Kaur, M. K. Sharma, Nucl. Phys. A **884-885**, 36-50 (2012).

Chapter 6

Decay analysis of superheavy nucleus (Z=118) formed in ^{48}Ca-induced reaction

6.1 Introduction

So far, the previous chapters report the observations that emerge from the decay analysis of compound nucleus formed in nuclear reactions using a variety of projectiles-n, p ,α and heavy-ions. It was observed that the mass of the decaying system, excitation energy, deformations and angular momentum play a crucial role in governing the decay channel. It has been reported that the CN ^{240}Np* formed in n-induced reaction prefers to decay via fission channel while the relatively lighter mass CN formed in n, p α and heavy-ion induced reactions choose to decay via particle evaporation and their corresponding decay patterns are addressed in terms of fragmentation potential and preformation factor in the previous chapters. In view of this, the analysis carried out in the present work is extended to superheavy mass region and for this purpose the investigation for the decay of ^{297}118* formed in ^{48}Ca+^{249}Cf reaction has been carried out in order to probe in to the decay dynamics.

The synthesis of superheavy elements (SHE) has always been an important research area and a number of nuclei having atomic number up to Z=118 with half-lives stable enough on nuclear time scales have been synthesized either via cold fusion reactions using ^{208}Pb or ^{209}Bi as the target [1–3] or as hot-fusion ones induced by ^{48}Ca projectiles [4–7]. The superheavy nuclei formed in above-mentioned fusion reactions undergo neutron evaporation and the residual nuclei have relatively longer half-lives and decay primarily through α-emission which terminantes at spontaneous-fissioning nucleus. The recent experimentation of Z=118 has been carried out at JINR, Dubna [6, 7], to analyze the $3n$ evaporation channel of ^{297}118* compound nucleus (CN) formed in ^{249}Cf+^{48}Ca reaction at E^*_{CN}=29.2±2.5 and 34.4±2.3 MeV (E_{beam}= 245 and 251 MeV, respectively).

Also, an α-decay chain is observed [5] from the residual SHN ^{294}118, after 3n emission from the CN ^{297}118*. The T-dependent PCM, the PCM(T≠0), is applied to α-decay chain of Z=118 SHN ^{293}118, which is extended here to show that it removes the otherwise required scaling factor of 10^4 for α-decay half-lives calculated on PCM(T=0), applied to the cold fusion reaction [14] and ^{287,288,289}115 nuclei [16].

In addition to the above study, an extensive calculation using PCM(T≠0) to address the, not yet observed, but theoretically proposed [17, 18], heavy cluster emissions from even-Z ^{294}118, ^{290}116 and ^{286}114 parents occurring in α-decay chain of ^{294}118 has been carried out. In previous works [17, 18] using PCM(T=0), the possibility of heavy cluster decays of odd-Z ^{278}113, $^{287-289}$115 and ^{293,294}117 parents, corresponding to ^{208}Pb daughter having double magic shell closure or its nearer nuclei has been examined. It is relevant to remind here that PCM is the equivalent of using DCM for heavy-ion collisions at angular momentum ℓ=0. Also, the α-decay as well as heavy cluster emissions are analyzed first by using the PCM(T=0) and then by using PCM(T≠0) with deformations included up to quadrupole (β_2) and hot "optimum" orientations [20] of nuclei. The calculations are done by choosing nuclear proximity potentials Prox-1977 [21] and Prox-2000 [22] and then compared with other available theoretical calculations.

This chapter comprises of two sections, where section-6.2 provides the details of calculations involved while the conclusions are drawn in section-6.3.

6.2 Results and discussion

This section is categorized in to two subsections. In sub-section-6.2.1, the calculations for the decaying $^{297}118^*$ formed in ^{48}Ca induced reaction at $E_{c.m.}$=204.53 and 209.86 MeV (equivalently, at T=1.060 and 1.145 MeV, respectively) using the DCM are presented. Here, the fragmentation potential $V(\eta)$ of the decaying CN, preformation probability P_0, penetrability P, their ℓ-summed values, xn (x=2-4) evaporation channel cross sections, the decay barrier heights, and 'barrier-lowering' effects are analyzed for related nuclear structure effects. Furthermore, the cross-sections for the residue nucleus $^{294}118^*$ synthesized in ^{48}Ca+^{250}Cf reaction after 4n-evaporation from $^{298}118^*$ CN are also calculated. Then in sub-section-6.2.2, the half-lives of α-decays, along with the possibility of heavy cluster emission in the decay chain of recoiled SHN $^{294}118^*$, are studied within the framework of PCM(T≠0). For comparisons, the α-decay half-lives are also calculated for the ground-state decays using PCM(T=0 case). All these calculations are performed by using two different versions of nuclear proximity potential, namely, Prox-1977 and Prox-2000, including the quadrupole deformations (β_{2i}) and "hot-optimum" orientations (θ_i) of decay fragments, taken from Table-1 of [20].

6.2.1 Fusion-evaporation cross sections of $^{297}118^*$ and $^{298}118^*$ compound nuclei

(a)Role of deformations: Firstly, attempt has been made to address the experimental data [7] for ER cross-sections in reference to the decay of CN $^{297}118^*$ formed in ^{48}Ca+^{249}Cf reaction, by optimizing the neck values (ΔR) for the spherical choice of fragmentation using Prox77. However, the measured cross-sections [7] could not

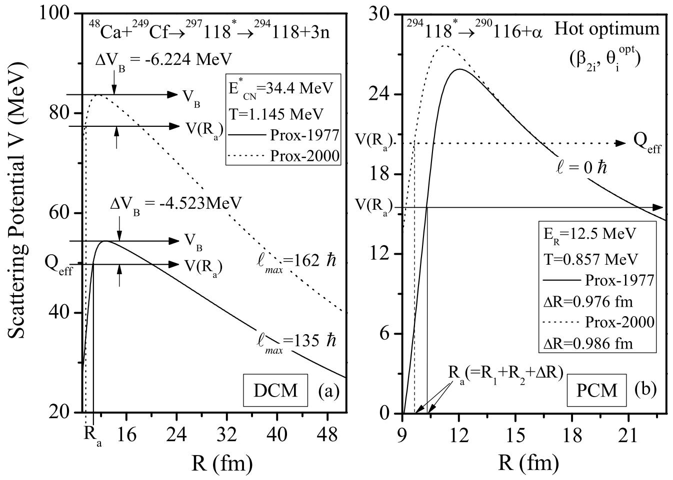

Figure 6.1: (a) Scattering potentials $V(R)$ for $^{297}118^{*}\rightarrow^{294}118+3n$ using the DCM, at a fixed temperature T=1.145 MeV, corresponding to E^{*}_{CN}=34.4 MeV, calculated at $\ell = \ell_{max}$. The barrier lowering parameter $\Delta V_B = V(R_a) - V_B$ is also depicted. (b) the same as for (a) but for α-decay of $^{294}118^{*}$, formed in the ^{48}Ca+^{249}Cf reaction after $3n$ emission, using the PCM at T=0.857 MeV (equivalently, E_R=12.5 MeV) for ℓ=0 case. Solid lines are for the Prox-1977 and dotted lines for Prox-2000 nuclear proximity potentials for deformed nuclei.

be addressed well at both E^{*}_{CN}=29.2 and 34.4 MeV, which in turn suggests the importance of including the deformation effects. Consequently, we included the deformation effects of decay fragments up to quadrupole deformations (β_2), in reference to "optimum" orientations of hot compact configurations. Interestingly, the experimental data on neutron evaporation channels at both the excitation energies was adequately addressed when deformation effects are included. Hence, it may be concluded that the deformations play a significant role as mass of the decaying compound nucleus approaches superheavy region. The importance of deformation is evident from Fig.6.2 where the fragmentation potential $V(A)$ is plotted with respect to A_2 for the case of Prox00 at $\ell = 0\hbar$ and ℓ_{max} values for the spherical as well as deformed considerations. Fig. 6.2 reveals that the fusion-ERs (LPs: $1n$, $2n$, $3n$ and $4n$) form the pre-dominant decay channel at ℓ=ℓ_{min}, whereas fission fragments start appearing in the decay process at ℓ=ℓ_{max}. Interestingly, as deformation and orientation effects are taken in to consideration, strong variations in the structure

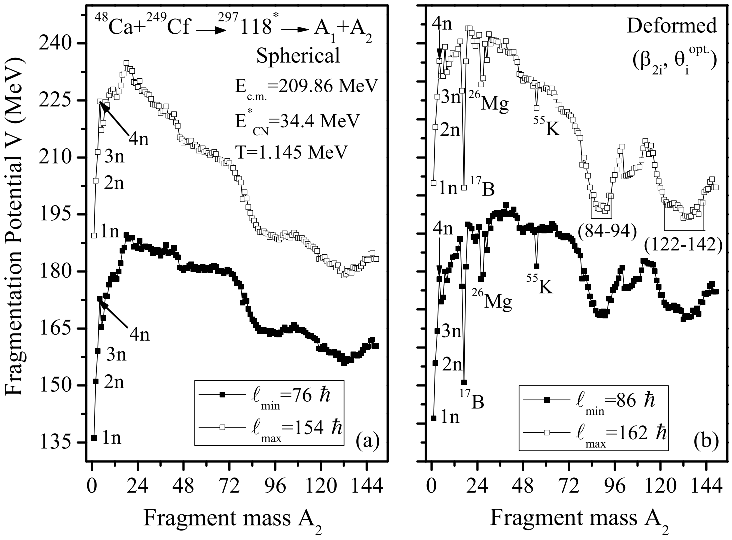

Figure 6.2: Mass fragmentation potential for $^{297}118^*$ using Prox00 for (a) spherical as well as (b) deformed configurations.

of potential energy surfaces (Fig. 6.2) can be seen which was observed to be smooth for spherical approach(Fig. 6.2). The dips emerging at ^{17}B, ^{26}Mg and ^{55}K nuclei are attributed to the inappropriate β_{2i} values. However, no effect on the total cross-section is seen due to these dips as they carry negligible penetrability P values as shown later in Fig. 6.5. Also, the fragmentation potential in Fig. 6.2 favors two strong minimas at A_2=84-94 and A_2=122-142, which constitute the not yet experimentally explored fusion-fission channel in the decay of $^{297}118^*$. An experimental verification of these predictions would be of further interest. From this discussion, we may conclude that the deformations and orientations play an essential role in understanding the neutron evaporation process in the decay of superheavy systems.

The DCM-calculated results for 2n and 3n evaporation σ_{2n} and σ_{3n} of CN $^{297}118^*$, using both nuclear potentials Prox-1977 and Prox-2000, with various neck-length parameters ΔR where the respective experimental data is fitted [7] at the two E^*_{CN}'s are presented in Table-6.1. Also, σ_{4n} is given for comparisons and apparently, the DCM reproduces the experimental data nicely within one parameter fitting, indicating negligible contribution for $4n$ cross-sections. The choice of different ΔR's

Table 6.1: The cross sections σ_{xn}, x=2, 3, 4 calculated using DCM for the decay of $^{297}118^*$ at two different E^*_{CN}'s, compared with available experimental data [7], for β_2 deformed and optimum oriented nuclei.

			Prox-1977		Prox-2000		
E^*_{CN} (MeV)	T (MeV)	Decay channel	ΔR (fm)	σ^{DCM}_{ER} (pb)	ΔR (fm)	σ^{DCM}_{ER} (pb)	$\sigma^{expt.}_{ER}$ (pb)
29.2	1.060	$2n$	1.35	0.210	0.96	0.609	-
		$3n$	1.65	0.391	1.065	0.310	$0.3^{+1.0}_{-0.27}$
		$4n$	1.75	2.22×10^{-4}	1.2	1.80×10^{-2}	-
34.4	1.145	$2n$	1.35	0.837	0.92	0.825	≤ 0.9
		$3n$	1.628	0.597	1.02	0.468	$0.5^{+1.6}_{-0.30}$
		$4n$	1.75	7.50×10^{-4}	1.2	6.54×10^{-3}	-

for different decay channels (here xn) refers to their occurrence in different time scales. A similar calculation has been made for 4n-evaporation cross-sections from $^{298}118^*$, formed in $^{48}Ca+^{250}Cf$ reaction, using both nuclear potentials Prox-1977 and Prox-2000, at the two above mentioned E^*_{CN}'s, taking the same ΔR as obtained in Table-6.1 for $^{297}118^*$. The calculated values of σ_{4n}=1.31×10^{-3} pb and 3.54×10^{-3} pb for Prox-1977, and 6.43×10^{-2} pb and 5.93×10^{-2} pb for Prox-2000, respectively, at E^*_{CN}=29.2 and 34.4 MeV. Interestingly, these DCM-calculated cross-sections are of similar orders as obtained in Table-6.1 for σ_{4n} of CN $^{297}118^*$ formed in $^{48}Ca+^{249}Cf$ reaction.

(b) Role of proximity potential: It has already been stated that the choice of proximity potential holds an eminent role in nuclear reaction dynamics. The role of proximity potential emerges from the above observation where the experimental data could not be achieved by using spherical approach within Prox77 potential but when Prox00 is used, the same could be addressed at optimized values of ΔR. In order to see the relative contributions of Prox77 and Prox00 potentials, the barrier height V_B is varied in terms of angular momentum ℓ and is shown in Fig.6.3. It

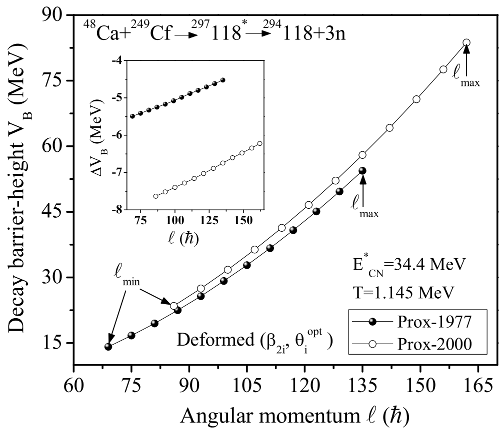

Figure 6.3: The barrier height V_B plotted as a function of angular momentum ℓ for $3n$ decay of the $^{297}118^*$ compound nucleus at E^*_{CN}=34.4 MeV, with use of Prox-1977 and Prox-2000. The comparison of "barrier-lowering" parameter ΔV_B is also shown as an inset.

is evident that, independent of the choice of proximity potential, V_B increases with increase of ℓ. A higher barrier height V_B is obtained for Prox-2000, as compared to that for Prox-1977, and the difference increases more at higher ℓ values. The variation of barrier modification ΔV_B with ℓ is also shown as an inset of the figure. It is clear that for the $3n$ decay channel at E^*_{CN}=34.4 MeV, ΔV_B turns out to be small for Prox-1977, as compared to that for Prox-2000. Apparently, the magnitude of ΔV_B decreases with ℓ, and one may conclude that large barrier modification is required for lower ℓ values.

Further it is known that in DCM, the decay cross-sections are a combined effect of both the preformation probability P_0 and penetrability P, Figs. 6.4(a) and (b) show the variations of calculated P_0 and P for $2n$ and $3n$ decay channels (or clusters emitted) from $^{297}118^*$ in terms of angular momentum ℓ for both Prox-1977 and Prox-2000 potentials. One may fix the ℓ_{max} and ℓ_{min} limits where the contribution of cross-sections becomes negligibly small. In other words, Fig.6.4(c) fix the limited range of angular momentum between ℓ_{min} and ℓ_{max} values, which give significant contribution towards the total cross-section values. It is seen that both xn (x=2, 3) clusters are highly preformed upto certain ℓ values for Prox-1977 and Prox-2000,

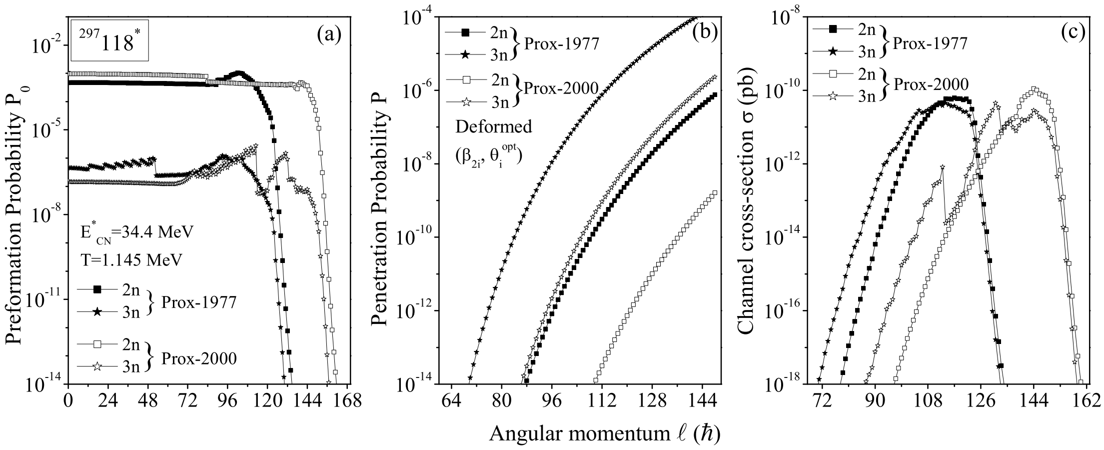

Figure 6.4: (a) P_0 values, (b)P values, and (c) the channel cross-sections σ_{2n} and σ_{3n} as a function of ℓ, for the two proximity potentials, illustrated for E^*_{CN}=34.4 MeV, for CN $^{297}118^*$ with deformations up to β_2 and optimum orientations.

and then P_0 drops to negligible values. On the other hand, in contrast to P_0, Fig. 6.4(b) depicts that the contribution of P goes on increasing as the ℓ value increases, irrespective of the choice of different proximity potentials i.e. while the preformation factor P_0 for $2n$ and $3n$ clusters decreases, the penetrability P increases as one goes from lower to higher ℓ values. The difference between the two approaches lie in the fact that higher value of ℓ_{max} and corresponding lower value of ΔR (see Table-6.1) is required to fit the available $2n$ and $3n$ channel cross-sections with the use of Prox-2000 as compared to Prox-1977. This happens because the barriers for the two proximity potentials come out to be different (see Fig. 6.1) and hence consequently a smaller neck-length is required when Prox00 is used, in comparison to Prox77. Also, Fig. 6.4 reveals that P_0 and P values depend significantly on the type of nuclear interaction potential used, thereby altering the overall decay cross sections.

Further, Fig. 6.5 presents the ℓ-summed P_0, P, and cross section σ, plotted as a function of fragment mass number for the two proximity potentials. It can be seen from this figure that the structure of σ is similar to that of P_0. The fragments with A_2=84-94 and A_2 =122-142 (and complementary fragments), corresponding to HMFs and AFF peaks are observed to contribute towards the net fission cross

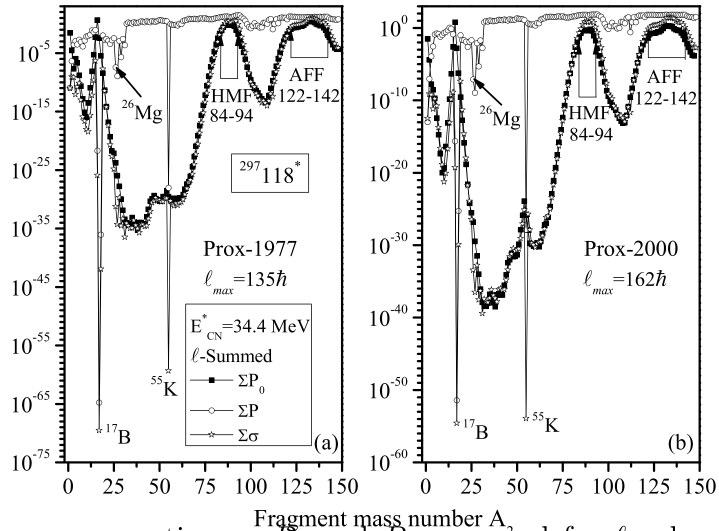

Figure 6.5: Decay cross section σ, P, and P_0, summed for ℓ values, plotted with respect to light fragment mass number A_2 for the decaying $^{297}118^*$ using (a) Prox77, and (b) Prox00.

sections. Also, it is noticed that summed P is almost constant there by contributes only towards the magnitude of the cross sections. The strongly preformed fragments ^{17}B, ^{26}Mg and ^{55}K which occur at dips in the fragmentation potential curve of Fig. 6.2, are shown to have very small penetrability values in Fig. 6.5 and hence, do not have any significant contribution towards final cross-section.

6.2.2 α-decay chain of SHN $^{294}118^*$ and the heavier cluster emissions from respective nuclei in α-decay chain

In this sub-section, an attempt is made to analyze the α-decay half-lives $T^{\alpha}_{1/2}$ using PCM (T=0) and T≠0, for the measured decay chain of $^{294}118^*$ formed via ^{48}Ca+^{249}Cf→$^{297}118^*$ reaction subsequent to $3n$ emission [5]. In addition, α-decay chains and the most probable cluster emission possibilities are worked out. In this process, the role of spherical and deformed magic shell closures of daughter nuclei is analyzed in view of exotic cluster emission.

Table 6.2: Comparison of experimental α-decay half lives for Z=114-118 SHEs occurring in α-decay chain of ^{294}118, synthesized in ^{48}Ca+^{249}Cf reaction via $3n$ emission, with our PCM(T≠0) calculations, using Prox77 and Prox00 at a temperature equivalent of recoil energy E_R=12.5 MeV and other available theoretical results. Calculated half-lives using PCM($T = 0$) for Prox77 for the deformed choice of nuclei are also listed.

α-decay of	ΔR (fm)		Half-lives, $T^{\alpha}_{1/2}$ (ms)							
			PCM(T≠0)		Expt. [5]	CYEM [40]	CPPMDN [41]	DDM3Y [42]	GLDM [43]	PCM(T=0)×10^4
	Prox77	Prox00	Prox77	Prox00						Prox77
^{294}118	0.976	0.986	0.69	0.65	$0.69^{+0.64}_{-0.22}$	2.188	$0.53^{-0.16}_{+0.22}$	$0.66^{+0.23}_{-0.18}$	$0.15^{+0.05}_{-0.04}$	0.69
^{290}116	0.950	0.938	8.51	8.57	$8.3^{+3.5}_{-1.9}$	56	$20.8^{-8.2}_{+13.8}$	$13.4^{+7.7}_{-5.2}$	$3.47^{+1.99}_{-1.26}$	8.39
^{286}114	0.941	0.934	118	118	120^{+40}_{-20}	831.7	170^{-60}_{+90}	160^{+70}_{-50}	50^{+20}_{-20}	119

In one of the earlier work [16] on PCM(T=0), applied to the decay of $^{287,288,289}115$ superheavy nuclei, the α-decay chain of $^{294}118$ was analyzed using Prox-1977 within PCM(T=0) for spontaneous decays, including quadrupole deformations β_{2i} and optimum orientations θ_i, taking the view that decay fragments get settled in the ground-state. It was found that the PCM(T=0) based half-lives for the measured [5] decay of $^{294}118$ agree well with experimental data with in a constant empirical factor of 10^4, for the value of neck-length ΔR lying in the range of 1.0-1.7 fm (see Table-6.2, last column). However, on the other hand, the experimental data could not be addressed to for use of the Prox-2000 potential. Therefore, it may be concluded that for spontaneous α-decays of superheavy nuclei, the use of Prox-1977 is relatively better than Prox-2000. While for the addressal of xn-evaporation cross-sections, Prox00 seems equally good.

Secondly, as an extension of the previous work [8] based on Prox-1977, the possibility of including temperature T effects in PCM, i.e., use PCM(T≠0) is investigated to account for the fact that the (residual) superheavy nucleus $^{294}118^*$, subsequent to 3n emission, has a recoil energy E_R (=7 to 18 MeV from experiments [5]) associated with it. Table-6.2 shows the results of calculated α-decay half lives $T^{\alpha}_{1/2}$ and other characteristic quantities (the neck-length ΔR's) for use of Prox-1977 and Prox-2000 potentials at an average (fixed) E_R=12.5 MeV to superheavy nuclei Z=118, 116 and 114 occurring in α-decay chains of $^{294}118^*$. Table-6.2 also shows a comparison of PCM(T≠0) for the two proximity potentials with other available theoretical formalisms such as CYE model [24], CPPMDN [25], DDM3Y effective interaction [26], and GLDM [27]. Interestingly, in agreement with earlier result [8], Table-6.2 shows that PCM(T≠0) calculations agree nicely with the experimental data, independent of the choice of proximity interaction. Another interesting result to note in Table-6.2 is that the α-decay half-life for $^{286}114$ is higher than for $^{290}116$ and $^{294}118$ parents, which illustrates the stability of Z=114 parent nucleus against α-emission than the Z=116 and 118. The stability of $^{286}114$ may be associated with the expected magic

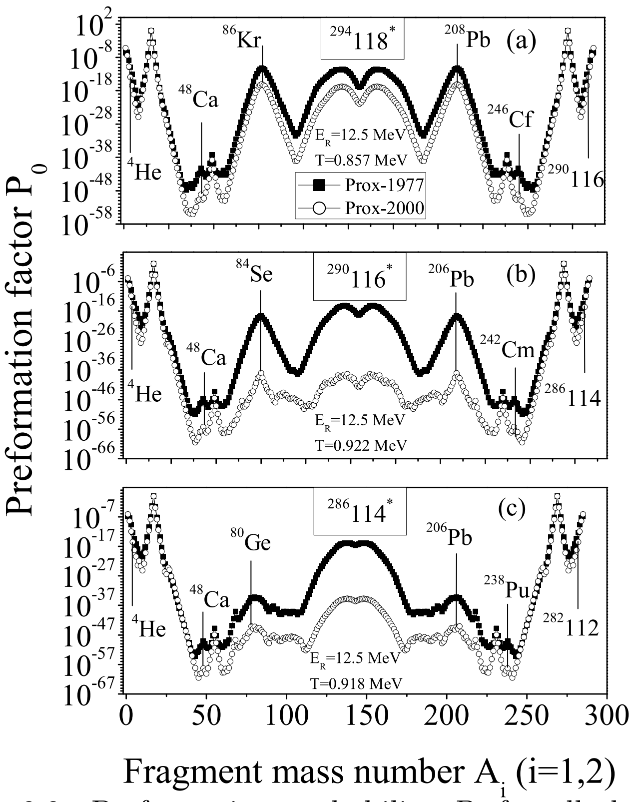

Figure 6.6: Preformation probability P_0 for all the parents occuring in α-decay chain of $^{294}118^{*}$ using PCM(T$\neq$0) for nuclear potentials Prox-1977 and Prox-2000 at recoil energy E_R=12.5 MeV. Calculations are done using β_{2i} deformations and "hot" optimum orientations for all the possible combinations at the respective ΔR values given in Table-5.2.

number of protons at Z=114, or of neutrons at N=172 or both.

Furthermore, the competition of α-decay with other possible cluster emissions is also probed by investigating the potential energy surfaces (PES) as presented in Fig. 6.6 for the decay process of $^{294}118^{*}$ at the temperature equivalent of recoil energy E_R=12.5 MeV. From this fig., it is clear that in addition to α-particle, the most prominent clusters emerging in the decay channel are ^{48}Ca and a heavier cluster, such as ^{80}Ge, ^{84}Se and ^{86}Kr, are emitted from Z=114, 116 and 118 nuclei, respectively. This result is consistent for different choices of proximity potential and only a slight change in structure is observed. Note that ^{48}Ca is a doubly magic nucleus, and the daughter nucleus of heavy clusters is the doubly magic ^{208}Pb or its

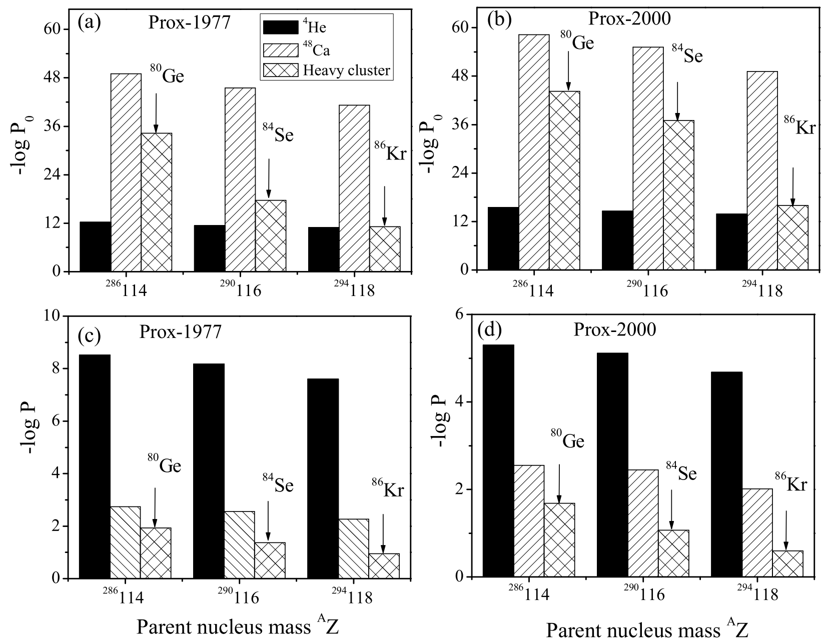

Figure 6.7: (a, b) Preformation and (c, d) penetration probability for alpha and other heavier cluster decays of the parents occurring in decay chain of $^{294}118^{*}$, using nuclear potentials Prox-1977 and Prox-2000 for deformed (up to β_2) choice of fragments.

neighboring nucleus, in agreement with recent work on PCM(T=0) [17].

Fig. 6.7 represents the PCM(T≠0)-calculated preformation P_0 and penetration P probabilities for α- and other most probable cluster decays from each of the parents in the α-decay chain of $^{294}118^{*}$ nucleus. It is clear that ^{4}He is always preformed with the largest probability (smallest -$log_{10}P_0$ value), though its P-values are very small. The shell structure effects are evident in P_0 because its magnitude is larger for clusters with doubly closed shell ^{208}Pb or its neighboring daughter nucleus. Also, it is noticed that heavy clusters ^{86}Kr, ^{84}Se and ^{80}Ge are preformed with larger P_0 values, compared to ^{48}Ca, respectively, in $^{294}118^{*}$, $^{290}116^{*}$ and $^{286}114^{*}$ parents. This happens possibly due to the deformed shell effects at Z_2=36 for light fragments or heavy clusters (actually at Z_2=36, 34 and 32) reinforce the spherical shell closure at Z_1=82 (^{208}Pb) for heavy-fragment. This result holds good for both the Prox77 and Prox00 used, thereby providing important information for the overall understanding

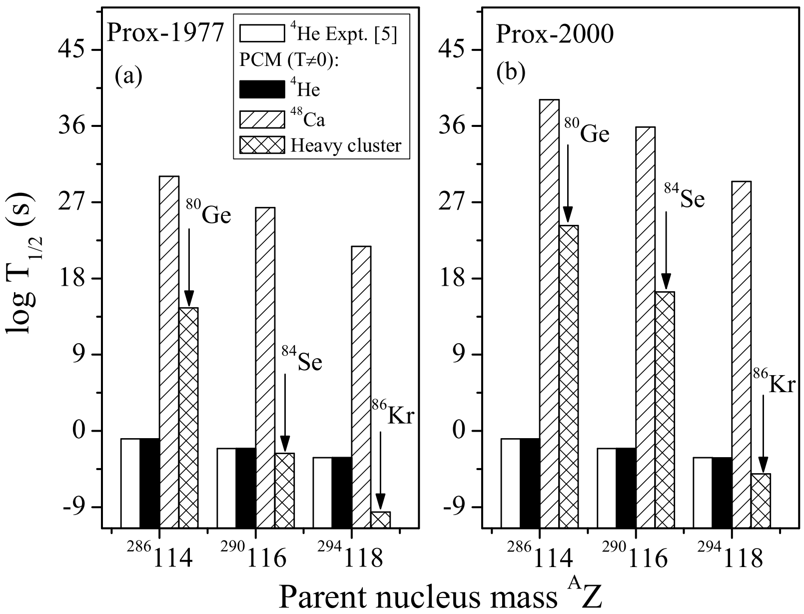

Figure 6.8: The logarithm of decay half-lives calculated on PCM (T≠0) for alpha and other cluster decays using (a) Prox-1977 and (b) Prox-2000 potentials, plotted as a function of parent nucleus mass for the α-decay chain of $^{294}118^*$.

of cluster dynamics from a variety of parent nuclei.

The consequences of the above results, for P_0 and P, are shown explicitly for the half-life time $T_{1/2}$ in Fig. 6.8, for both choices of the nuclear proximity force. It is noticed that calculated $T^{\alpha}_{1/2}$ agree well with the experimental data. Since $T_{1/2}$ is a combined effect of both P_0 and P (ν_0 being a constant, $\sim 10^{21}$ s^{-1}), it is observed in Fig. 6.8 that, in addition to the α-decay, the clusters corresponding to doubly magic ^{208}Pb, or its neighboring daughter nucleus, have minimal decay half-lives, independent of the choice of nuclear proximity potential. As noted above, this effect is solely due to the combined effect of spherical doubly magic ^{208}Pb and the deformed magic shells around Z_2=36. On the other hand, for ^{48}Ca cluster, though doubly spherical magic, the predicted decay half-life lies far above the heavy clusters because the heavier fragments (^{246}Cf, ^{242}Cm or ^{238}Pu) are strongly deformed nuclei. Thus, the present study indicates the interesting possibility of heavier clusters like ^{86}Kr, ^{84}Se and ^{80}Ge, in addition to α-decay, for the decay of $^{294}118^*$ and its subsequent parents

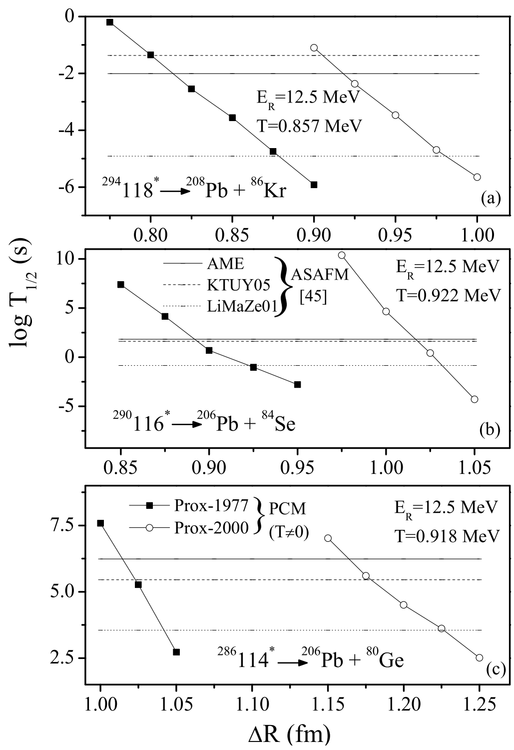

Figure 6.9: Predicted decay half-life times using PCM(T≠0) in terms of neck-length values for the most favored heavy clusters emitted from (a)$^{294}118^*$, (b) $^{290}116^*$, and (c) $^{286}114^*$ parents resulting in a doubly magic ^{208}Pb or its neighboring daughter nucleus, compared with the predictions of ASAFM for different mass tables.

ending the chain in $^{286}114^*$. Finally, it is to be noticed that the above predictions are made purely on the basis of best fitted ΔR values obtained in reference to the measured α-decay half-lives in the decay chain of $^{294}118^*$ for use of PCM(T≠0) at E_R=12.5 MeV (refer Table-6.2). Since the choice of ΔR is extremely sensitive to PCM calculations, an effort is made in Fig. 6.9 to predict decay half-lives over a range of ΔR for the most probable heavy clusters emitted from $^{294}118^*$, $^{290}116^*$ and $^{286}114^*$ parents with decay products treated as deformed and oriented nuclei. Note, this work is an extension of [17,18] carried out using PCM(T=0) for the ground-state cluster decays of $^{278}113$, $^{287-289}115$ and $^{293,294}117$ parents. However, in the present work, the half lives have been calculated using PCM(T≠0) and then compared with those predicted by ASAFM [28, 29]. Fig. 6.9 shows this comparison of our results using PCM(T≠0) with those provided by ASAFM, obtained by using mass tables of

AME11, LiMaZe01 and KTUY05. As expected, log $T_{1/2}$ values for the three clusters, respectively, from $^{294}118^*$, $^{290}116^*$ and $^{286}114^*$ parents are significantly influenced by the variation of ΔR, thereby giving different contributions for both the choices of nuclear potentials. Such a study provides a testing ground for future studies of cluster decay measurements. However note that the concept of heavy particle radioactivity is merely a theoretical concept, which comes into picture as a competing decay channel with respect to α-decay from the super-heavy parents.

6.3 Conclusions

The present work helps in extending the understanding of nuclear reaction dynamics as the compound nucleus formed in this case lies in the superheavy mass region, unlike previous chapters where the mass of compound nuclei lie in light to heavy mass region and were formed in n, p α or heavy-ion induced reactions. This work presents the dynamics of heavy-ion induced reaction (using ^{48}Ca as projectile) where the target nucleus lies in transactinide region so that the resulting super-heavy compound nucleus is formed. This work highlights the role of different proximity interactions for the decayinng $^{297,298}118^*$ superheavy systems formed in the ^{48}Ca+^{249,250}Cf reactions within the framework of DCM. By including the quadrupole (β_{2i}) deformations, together with the "optimum" orientations, the DCM calculated $2n$ and $3n$ evaporation residue (ER) cross-sections, using both Prox-1977 and Prox-2000, find a nice comparison with experimental data for ^{48}Ca+^{249}Cf reaction at two incident energies. However, the relative contribution of σ_{4n} in ^{48}Ca+^{250}Cf reaction, though of the same order as 4n channel in ^{48}Ca+^{249}Cf reaction, comes out to be much smaller in comparison to its observed $3n$ channel. Apparently, further experiments are needed for the verification of $4n$ component in the reactions under study.

Also the variation of barrier height (V_B), potential energy surfaces (PES) and barrier-lowering effects are analyzed to provide a better description of the dynamics involved. The contribution from the fusion-fission component, which is not yet experimentally verified, constituting both heavy mass and asymmetric mass fragments is indicated. In addition to this, it is explored that (i) the barrier height is strongly modified with the inclusion of different nuclear potentials. (ii) The barrier lowering parameter ΔV_B has lower magnitude for Prox-1977. (iii) A smaller value of neck-length parameter is obtained for the use of Prox-2000, as compared to Prox-1977 potential.

Finally, the results of α-decay half-lives of ^{294}118, and its subsequent ^{290}116 and ^{286}114 parents occurring in the decay chain, are presented within the formalism of preformed cluster model (PCM, T$\neq$0) which helps in establishing the role of temperature T-dependence in its in-built preformation and penetration probabilities of decay fragments. A competition between α-decay and other heavier clusters emitted from all the parents in the α-decay chain is investigated with a view to understand further about the dynamics and related structure information.

The role of excitation energy, angular momentum, deformations and orientations, moment of inertia, neutron to proton asymmetry, level density parameter etc. are extensively explored in Chapters 3-6. A brief summary and outlook of this work is presented in the next chapter.

Bibliography

[1] S. Hofmann and G. Münzenberg, Rev. Mod. Phys. **72**, 733 (2000).

[2] S. Hofmann, Radiochim. Acta **99**, 405 (2011).

[3] K. Morita, *et al.*, J. Phys. Soc. Jpn. **76**, 045001 (2007).

[4] Yu. Ts. Oganessian, *et al.*, Phys. Rev. C **87**, 014302 (2013), and earlier references therein.

[5] Yu. Ts. Oganessian, *et al.*, Phys. Rev. Lett. **109**, 162501 (2012).

[6] Yu. Ts. Oganessian, *et al.*, JINR Communication D7-2002-287 (2002); see http://www.jinr.ru/publish/Preprints/2002/287(D7-2002-287)e.pdf

[7] Yu. Ts. Oganessian, *et al.*, Phys. Rev. C **74**, 044602 (2006).

[8] Niyti, G. Sawhney, M. K. Sharma, and R. K. Gupta, Phys. Rev. C **91**, 054606 (2015).

[9] Yu. Ts. Oganessian, *et al.*, Phys. Rev. C **79**, 024603 (2009).

[10] G. Mandaglio, *et al.*, Phys. Rev. C **86**, 064607 (2012).

[11] T. Cap, *et al.*, Phys. Rev. C **88**, 037603 (2013).

[12] N. Wang, *et al.*, Phys. Rev. C **89**, 037601 (2014).

[13] V. Ninov, *et al.*, Phys. Rev. Lett. **83**, 1104 (1999).

[14] R. K. Gupta, S. Kumar, R. Kumar, M. Balasubramaniam, and W. Schied, J. Phy. G: Nucl. Part. Phys. **28**, 2875 (2002).

[15] R. Smolańczuk, Phys. Rev. C **56** (1997) 812; *ibid* **59** (1999) 2634; Phys. Rev. Lett. **83** (1999) 4705.

[16] R. Kumar, K. Sandhu, M. K. Sharma, and R. K. Gupta, Phys. Rev. C **87**, 054610 (2013).

[17] G. Sawhney, K. Sandhu, M. K. Sharma, and R. K. Gupta, Eur. Phys. J. A **50**, 175 (2014).

[18] G. Sawhney, K. Sandhu, M. K. Sharma, and R. K. Gupta, EPJ Web of Conferences **86**, 00041 (2015).

[19] R. K. Gupta, in Lecture Notes in Physics, 818, Vol. **1**, *Clusters in Nuclei*, edited by C. Beck (Springer-Verlag, Berlin, Heidelberg, 2010), pp. 223-264.

[20] R. K. Gupta, M. Balasubramaniam, R. Kumar, N. Singh, M. Manhas, and W. Greiner, J. Phy. G: Nucl. Part. Phys. **31**, 631 (2005).

[21] J. Blocki, J. Randrup, W. J. Swiatecki, and C.F. Tsang, Ann. Phys. (N.Y.) **105** 427 (1977).

[22] W. D. Myers and W. J. Swiatecki Phys. Rev. C **62**, 044610 (2000).

[23] Niyti and R. K. Gupta, Phys. Rev. C **89**, 014603 (2014).

[24] G. M. Carmel Vigila Bai and J. Umai Parvathiy, Pramana J. Phys. **84**, 113 (2015).

[25] K.P. Santhosh and B. Priyanka, Phys. Rev. C **89**, 064604 (2014).

[26] C. Samanta, P. Roy Chowdhury, and D. N. Basu, Nucl. Phys. A **789**, 142 (2007).

[27] G. Royer and H. F. Zhang, Phys. Rev. C **77**, 037602 (2008).

[28] D. N. Poenaru, R. A. Gherghescu, and W. Greiner, Phys. Rev. Lett. **107**, 062503 (2011).

[29] D. N. Poenaru, R. A. Gherghescu, and W. Greiner, Phys. Rev. C **85**, 034615 (2012).

Chapter 7

Summary and future scope

This present work is concerned with the understanding of the decay dynamics of nuclear reactions formed via variety of projectiles. The use of projectiles having masses lying in different regions is important not only because it leads to the formation of a variety of compound nuclei covering a broader region of the periodic table but also provides an opportunity to explore the dynamical behavior of compound nuclei. The compound nuclei choose to decay via light particle evaporation or via heavier fragments emission depending up on their masses and reaction conditions. Hence, the primary purpose of this thesis is to study the kinematics of n, p, α and heavy-ion induced reactions and to analyze the subsequent decays of the compound nuclei thus formed. The significance of this analysis arises from the fact that the aforementioned reactions form incoming channels having different asymmetries and the compound systems thus formed cover the whole mass region of the periodic table ranging from light mass ^{61}Ni* formed in n-induced reaction to superheavy $^{297}118^*$ formed in heavy-ion induced reactions.

In view of this, a brief description of the nuclear reactions, their types, their asymmetries and the role of this asymmetry in conversion of beam energy E_{beam} in to kinetic energy of incident channel $E_{c.m.}$ is discussed in *Chapter-1*. This chapter provides a generalized description of the overall work carried out in this thesis. The objectives of the present work are pursued within the frame-work of the Dynamical

Cluster-decay Model DCM, which is based on collective clusterization technique, following the Quantum Mechanical Fragmentation Theory (QMFT). The methodology proceeds through the transference of the beam energy E_{beam} to center of mass energy $E_{c.m.}$ (which is controlled by the asymmetry of the incoming channel) and hence to the excitation energy $E_{CN}{}^*$ of the exit channel. This methodology works in two-steps: the first step involves the estimation of probability with which the decaying fragments are pre-born within the parent nucleus and the second step involves the estimation of probability of the pre-born fragments tunnelling through the potential barrier. The adequate description of this methodology is explained in Chapter-2 covering the detailed description of the potentials used, the moment of inertia expressions, the radius terms and the level density parameter etc.

First of all, the reaction dynamics governing the decay of compound nucleus $^{240}Np^*$ formed in highly asymmetric n-induced reactions over incident beam energy of E_n=0.62-18.75 MeV is worked out. The heavy mass nucleus $^{240}Np^*$ formed here decays via fission channel and the cross-sections are fitted using the neck-length parameter ΔR of the DCM. The decay of $^{240}Np^*$ is analyzed by including the effect of quadrupole deformations on the fragmentation structure and it is concluded that with inclusion of deformations, the decay profile becomes more asymmetric, however, the fragments contributing towards the decay cross-sections remain same (A_2=100-112). The enhancement in cross-sections at the three energies is attributed to the orientations of the decaying fragments as change in structure is observed when hot (equatorial) orientations are replaced with cold (polar) configuration. The significance of moment of inertia in the decay of $^{240}Np^*$ is also investigated from the corresponding structural variations that come in to picture. It is observed that effect of choice of moment of inertia is prominent for lighter fragments as compared to heavier fragments and the non-sticking approach seems better for the description of particle evaporation and the sticking approach for fission decays. Also, the comparative analysis of decay profiles of $^{240}Np^*$ and $^{238}U^*$ show similar fragmentation structures with small variations in magnitude for both the decaying nuclei.

After this, in order to investigate the effect of the mass of the decaying compound nucleus, the decay of compound nucleus $^{61}Ni^*$ formed in n-induced reaction over an incident beam energy range of E_n=1-100MeV is carried out and it has been found that the compound system $^{61}Ni^*$ chooses to decay via particle evaporation attributed to its lighter mass unlike, the system $^{240}Np^*$, which decays via fission channel. The experimental data has been addressed using the non-sticking moment of inertia I_{NS} and the cross-sections for the α-cluster emission or $2p2n$-multinucleon emission are fitted nicely by opting appropriate values of neck-length parameter. The emission of light charged particles is favored at lower angular momentum values and the compound nucleus $^{61}Ni^*$ undergoes near symmetric fragmentation at lower center of mass energies $E_{c.m.}$ and with increase in $E_{c.m.}$, a change in the structure is observed. Also, with increase in energy, the emission of α-cluster is replaced with 2p2n-multinucleon emission. This transmutation of α-emission at lower energies and $2p2n$-emission at higher energies is explained on the basis of temperature dependence of the binding energies used in DCM, and it has been observed that the binding energy of α-cluster possesses lower magnitude at lower temperature (T in MeV) while above a particular temperature T=2.9 MeV, the trend gets reverted with $2p2n$-cluster having lower values of binding energies. Also, the effect of mass (and charge) of the compound nucleus on α and $2p2n$-multinucleon emission is analyzed and comparative analysis is done for the decay of various compound nuclei having mass ranging from light to intermediate mass region.

Furthermore, the decay analysis of compound systems- $^{77}As^*$, $^{83}Br^*$ and $^{86}Sr^*$ formed in p-induced reactions is also carried out at common beam energy E_{beam}=1-5 MeV. The chosen compound systems decay via n-evaporation and the experimentally available data is addressed adequately by using the collective clusterization technique of DCM. The calculations are done using spherical fragmentation approach and the role of deformations is also analyzed, signifying that the inclusion of deformations makes the decay profile more asymmetric as compared to spherical approach. The role of angular momentum on the decay path has also been investigated and similar results have been drawn that light particle evaporation is preferred at lower ℓ-values only and heavy fragments start appearing in the fragmentation channel at higher ℓ-values. The DCM calculated cross-sections are analyzed for their dependence on the nuclear level density parameter by varying the value of LDP from 6-10 and by including mass-dependence in it. The results conclude that the DCM calculated cross-sections for n-evaporation are insensitive to the choice of level density up to those ℓ-values up to which the n-evaporation dominates in decay channel, and as soon as the ℓ-values are increased further, due to competing heavier fragments, a variation in the cross-sections can be observed. Similar results are obtained when mass-dependent level density parameters are used.

After this, the decay analysis of the compound systems ^{117}Sb*, ^{145}Pm* and ^{191}Ir* formed in α-induced reactions is carried out over an incident beam energy range $E_\alpha \sim$ 10 to 15 MeV within the framework of DCM along with the dynamics involved in the decay of ^{98,104}Cd* systems formed in ^{40}Ca-induced reactions over a beam energy range of E_{Ca}=105-155 MeV. The compound nuclei formed in the above-mentioned reactions are investigated for light particle evaporation and the DCM calculated cross-sections find nice agreement with the experimental data. For the CN formed in α-induced reactions, the role of mass of the CN on the fragmentation structure is analyzed along with the role of deformations of the decaying fragments. The significance of these emerges from the structural variations that come in to picture. The role of angular momentum is analyzed for both α as well as heavy-ion induced reactions and it has been observed that the lower angular momentum values favor particle evaporation while high ℓ-values signify the presence of heavier fragments in the decay channel. These results lie in nice agreement with the results observed for n and p-induced reactions. Additionally, the neutron to proton asymmetry effects are investigated and for this purpose asymmetry dependence is included in bulk constant α (used in LDM term) and the radius expression and the corresponding effect on fragmentation structure is investigated. It is observed that by including asymmetry in Bulk constant α, the overall fragmentation structure remains same however the magnitude of fragmentation potential changes at individual fragment level. For the use of asymmetry dependent radius, a decrement in preformation probability P_0 and an enhancement in barrier tunnelling probability P is observed while the decay cross-sections follow the trend of P_0 leading to a net decrement in their magnitude.

Lastly, this work highlights the role of different proximity interactions for the decay of $^{297,298}118^*$ superheavy compound systems formed in the ^{48}Ca+^{249,250}Cf reactions within the framework of dynamical cluster decay model. By including the quadrupole (β_{2i}) deformations, together with the "optimum" orientations, the DCM calculated $2n$ and $3n$ evaporation residue (ER) cross-sections, using both Prox-1977 and Prox-2000, find a nice comparison with experimental data for ^{48}Ca+^{249}Cf reaction at two incident energies. The variation of decay barrier height, potential energy surfaces, and barrier-lowering effects etc. are analyzed to extract a better picture of the dynamics involved. A possible contribution for the, not yet observed, fusion-fission component constituting both heavy mass and asymmetric mass fragments is predicted.

The barrier height is observed to get strongly modified with the inclusion of different nuclear potentials and the barrier lowering parameter ΔV_B is found to be least for Prox-1977. For the use of Prox-2000 a relatively smaller value of neck is required. The α-decay half-lives of $^{294}118$, and its subsequent $^{290}116$ and $^{286}114$ parents occurring in the α-decay chain, are addressed via preformed cluster model (PCM) for ground state analysis T=0 and T$\neq$0 considerations. The competition of α-decay with other possible heavy cluster emissions from all the parents in the α-decay chain is also probed with a view to understand further about nuclear dynamics and related structure information.

The present work involves the role of T-dependence in binding energies, mass dependence in level density parameter, the use of neutron to proton asymmetry dependence in Bulk constant (α) and radius term R_i, deformations and orientations and moment of inertia etc. The decay dynamics have been worked out for n, p, α and heavy ion induced reactions. Further as an extension of this work, the effect of some of these parameters may be exploited for some exotic nuclei formed near the drip line which may provide further insight regarding the reaction dynamics governed via variety of projectile beams. In addition to this, the dynamics can also be worked out where the various projectiles are incident upon the same target, there by providing an analysis of the use of different projectiles.